LBNL-48993

ERNEST ORLANDO LAWRENCE
BERKELEY NATIONAL LABORATORY

Gas Phase ^{129}Xe NMR Imaging and Spectroscopy

Lana G. Kaiser

Materials Sciences Division

September 2001

Ph.D. Thesis

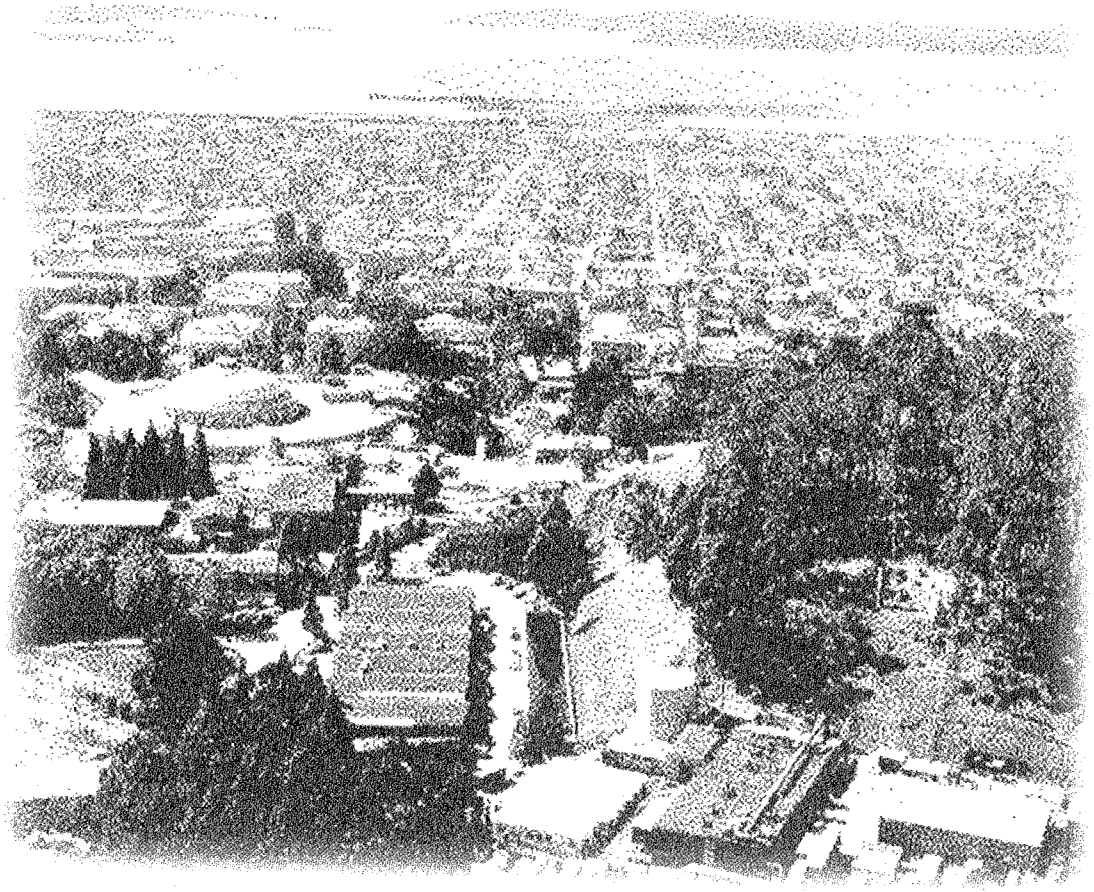

Gas Phase ^{129}Xe NMR Imaging and Spectroscopy

Lana Galina Kaiser
Ph.D. Thesis

Department of Chemistry
University of California, Berkeley

and

Materials Sciences Division
Lawrence Berkeley Laboratory
University of California
Berkeley, CA 94720

Fall 2000

This work was supported by the Director, Office of Science, Office of Basic Energy Sciences, Materials Sciences Division, of the U. S. Department of Energy under Contract No. DE-AC03-76SF00098

Gas Phase ^{129}Xe NMR Imaging and Spectroscopy

by

Lana G. Kaiser

B. S. (Illinois State University) 1996

A dissertation submitted in partial satisfaction of the requirement for the degree of

Doctor of Philosophy

in

Physical Chemistry

in the

GRADUATE DIVISION

of the

UNIVERSITY OF CALIFORNIA, BERKELEY

Committee in charge:

Professor Alexander Pines, chair

Professor A. Paul Alivisatos

Professor Jeffrey A. Reimer

Fall 2000

Abstract

Gas Phase ^{129}Xe NMR Imaging and Spectroscopy

by

Lana G. Kaiser

Doctor of Philosophy in Chemistry

University of California at Berkeley

Professor Alex Pines, Chair

Liquid and solid state Nuclear Magnetic Resonance (NMR) spectroscopy has been applied successfully in many scientific, medical and industrial applications. Gas phase NMR, however, has prohibitively low sensitivity for most of the NMR techniques. In the last decade the problem of low sensitivity of xenon in the gas phase has been overcome by the use of optical pumping of noble gases, increasing the polarization by several orders of magnitude.

This manuscript describes the technique and several applications of optical pumping under continuous flow, which significantly facilitates multidimensional gas phase NMR experiments. Magnetic resonance imaging (MRI), combined with continuous flow of laser-polarized xenon, provides visualization of the gas dynamics in porous media. The sensitivity of the xenon chemical shift to the surfaces of the host materials has been exploited in chemical shift selective 3-D MRI of xenon gas adsorbed in molecular sieves (zeolites) and aerogels.

Stochastic displacement of xenon in porous medium is investigated in two environments: diffusion through an aerogel framework with virtually non-restricted

motion (via PFG technique) and single file diffusion in organic material TPP (via build-up curves of xenon signal intensity as a function of time). Also the interplay between stochastic and deterministic phenomena is investigated in xenon gas undergoing Poiseuille flow in a pipe, where molecular displacements due to flow and diffusion are monitored via dynamic NMR microscopy. Finally the transfer of polarization from laser-polarized xenon to protons of large molecules in solution via Nuclear Overhouser Effect (NOE) is demonstrated using batch mode optical pumping method.

...Like nitrous oxide, which may also act on NMDA receptors, xenon gas can induce a state of euphoria...

N. P. Franks et al, Nature ***396,*** *324 (1998)*

Acknowledgements

First and foremost I would like to thank Alex Pines for his enthusiastic support and guidance in my research. I also would like to thank Dr. Seth Bush for his friendship and support in the laboratory through high and low. Special thanks go to Dr. Eike Brunner, who was always such a supportive and knowledgeable coworker. His ideas about applying MRI to continuous flow system made me interested in NMR imaging. Dr. Roberto Seydoux has spent a tremendous amount of time designing and implementing the optical pumping system, thus building a great foundation for the research described in this manuscript. Dr. Thomas Meersmann infused the porous materials imaging project with endless ideas and insights, as well as improving the optical pumping system. John Logan was a great co-worker who always amazed me with his level of competence in all things Matlab and science in general. I would also like to thank Dr. Marco Tomacelli, Dr. Birgit Shwickert, Dr. Sunil Saxena, Dr. Mark Kubinec, Dr. Dihn Tong, Gosia Marjanska and Annjoe Wongfoe for being such great Pinenuts and Dione Carmichael, for keeping the laboratory running.

Most important, this dissertation would not have been possible without my great family: my mom Galina, my husband Mark, and my children Anya and George.

To my family: my mother Galina,

my husband Mark,

my children Anastasia and George

Chapter 1

Introduction to gas phase ^{129}Xe NMR imaging and spectroscopy

Since its discovery in the forties by Bloch and Purcell, magnetic resonance phenomenon has been used extensively as a very powerful tool in science, technology and medicine (1, 2). Today chemists and physicists use Nuclear Magnetic Resonance (NMR) spectroscopy as a local, non-invasive probe for studying molecular dynamics, structure and chemical determination. An extension of NMR spectroscopy, Magnetic Resonance Imaging (MRI), has established itself as an invaluable diagnostic tool in the medical community. New methods that improve both sensitivity and resolution are continually being developed, encouraging applications of NMR and MRI to solving even more scientific puzzles. Many of these methods and their application can be found in illuminating books, which describe the main principles of NMR spectroscopy (3-6) and

MR imaging (7 - 9). The interested reader can find the description of the basic liquid and solid state NMR and MRI experiments in these references.

Application of multi-dimensional NMR and MRI techniques to gases has not been actively pursued until recently due to a variety of challenges. Polyatomic gases containing spin I = ½ nuclei have relaxation times that are dominated by spin-rotation interaction. Very short relaxation times, typically of the order of milliseconds, are frequently observed as a result of the interaction between the nuclear spins and fluctuating intramolecular magnetic fields produced by rapid molecular rotation. The most significant problem, however, is poor signal to noise ratio, a consequence of the low density of nuclear spins in the gas phase. NMR is also considered an insensitive technique compared with other spectroscopic methods due to very low nuclear polarization generated in even the strongest of available magnetic fields. The nuclear polarization can be defined with the following relation:

$$P = \frac{N\uparrow - N\downarrow}{N\uparrow + N\downarrow} \tag{1}$$

where $N\uparrow$ and $N\downarrow$ are respectively the fractions of spins in the $m_i = 1/2$ and $m_i = -1/2$ states. At thermal equilibrium, the values of $N\uparrow$ and $N\downarrow$ are nearly equal, as given by the Boltzmann distribution,

$$N\uparrow = \frac{\exp(-\gamma\eta B_0 / 2kT)}{\sum_i \exp(-m_i \gamma\eta B_0 / kT)} \tag{2}$$

where γ is the gyromagnetic ratio, k is Boltzmann's constant, and η is Planck's constant divided by 2π. Using the above equation we may express nuclear polarization as

$$P = \tanh(\gamma\eta B_0 / 2kT) \tag{3}$$

In general, $\gamma\eta B_0 / kT \ll 1$, so equation (1) can be reduced to

$$P \approx \gamma \hbar B_0 / 2kT \qquad (4)$$

For a collection of protons at room temperature at typical NMR magnetic field strengths, equation (3) gives $P \sim 10^{-5} - 10^{-6}$. The nuclear magnetization M is proportional to P:

$$M = \frac{1}{2} N_s \gamma \hbar P \qquad (5)$$

where N_s is the number of spins. Thus improving the equilibrium magnetization can be performed only by increasing B_0 (which grows progressively expensive and difficult), or by lowering T (which may induce transition from gas phase to liquid or solid state and also is inappropriate for various types of samples in general, especially living organisms). When matter is in a gas phase the number of nuclei in a given sample volume is reduced by almost a factor of a thousand.

Two main experimental approaches were explored in the past few years with a goal of overcoming the severe insensitivity of gas phase NMR imaging and spectroscopy. The one simple way to increase sensitivity is to signal average (adding spectra mathematically). The signal adds in linearly with the number of co-added acquisitions N, while the random noise increases only as the square root, $\sqrt{N}$; thus the signal to noise increases as $N/\sqrt{N} = \sqrt{N}$. Kuethe et al (10) and Lizac et al (11) have used this approach to image fluorine gas (high sensitivity nuclei) by applying rapid signal averaging. Rapid transverse relaxation of the gas phase species, however, requires RF excitation in the presence of the frequency-encoding gradient. This introduces a line-width restriction on resolution as well as distortion of the k-space origin data due to the spectrometer dead time. In addition, this technique is not very useful for gases with long spin-lattice

relaxation time, since one has to wait some time on the order of three relaxation times for co-addition (6), translating into days of experimental time.

In the last decade an alternative method involving spin-exchange optical pumping has received a great deal of attention in the NMR and MRI community. Using this method (in which the signal sensitivity is enhanced by spin-exchange between optically pumped electron spin states of alkali metals and nuclear spin states of noble gases), it is possible to obtain a 10,000 to 100,000-fold increase of nuclear spin polarization over the natural thermal Boltzmann distribution (12). Two inert gases regularly used in the spin-exchange process are ^{129}Xe and ^{3}He (it is also possible to optically pump the nuclear spins of ^{3}He in a single step by a process called metastability exchange (13)).

One of the most exciting isotopes for NMR spectroscopy is ^{129}Xe, which has a nuclear spin of I=1/2 with natural abundance of 26.44 %. Xenon is a noble gas, forming only a few compounds, primarily with fluorine and oxygen (14, 15). Before the use of optical pumping techniques, there has been already a substantial use of one-dimensional ^{129}Xe NMR spectroscopy as a probe for investigating zeolites (16, 17), anisotropic environments (18) and liquids (19). ^{129}Xe NMR is an attractive probe of various environments due to its inertness and very sensitive chemical shift, which varies within an enormous range (over 6000 ppm). The large electron cloud of ^{129}Xe has symmetrically spherical distribution and any distortion of this cloud is reflected in the NMR chemical shift. Figure 1.1 shows isotropic chemical shift range of xenon in different chemical environments and physical states.

The use of optical pumping greatly facilitates traditional one-dimensional experiments that are performed with thermally polarized ^{129}Xe NMR, reducing the

experimental times from hours to seconds (for example, chemical shift studies of xenon adsorbed in zeolites (17)). Perhaps the most exciting aspect of optically pumped ^{129}Xe NMR is that it opens the door to a number of gas phase NMR experiments that were heretofore inaccessible: multi-dimensional techniques such as gas phase MR imaging and dynamic NMR microscopy. The main focus of this manuscript is to demonstrate the emergence of this new approach to laser-polarized ^{129}Xe NMR as a tool for multi-dimensional gas phase NMR spectroscopy and imaging.

Chapter 2 describes optical pumping process and its incorporation into NMR and MRI experiment followed by discussion of the advantages and disadvantages of the two main methods of producing laser-polarized xenon (batch mode and continuous flow mode). Chapter 3 demonstrates the possibility of multidimensional imaging experiments for the purpose of studying behavior of xenon gas in porous media and in a lipophilic environment. Chapter 4 contains examples of monitoring stochastic displacements of xenon gas in porous media via Pulsed Field Gradient (PFG) technique. Chapter 5 describes the study of the interplay between coherent and stochastic displacements in a gas phase Poiseuille flow using dynamic NMR microscopy. Finally Chapter 6 addresses application of laser-polarized ^{129}Xe NMR as a probe for atomic scale interactions, mainly the transfer of xenon polarization via Nuclear Overhouser Effect to protons of large macromolecules in solution.

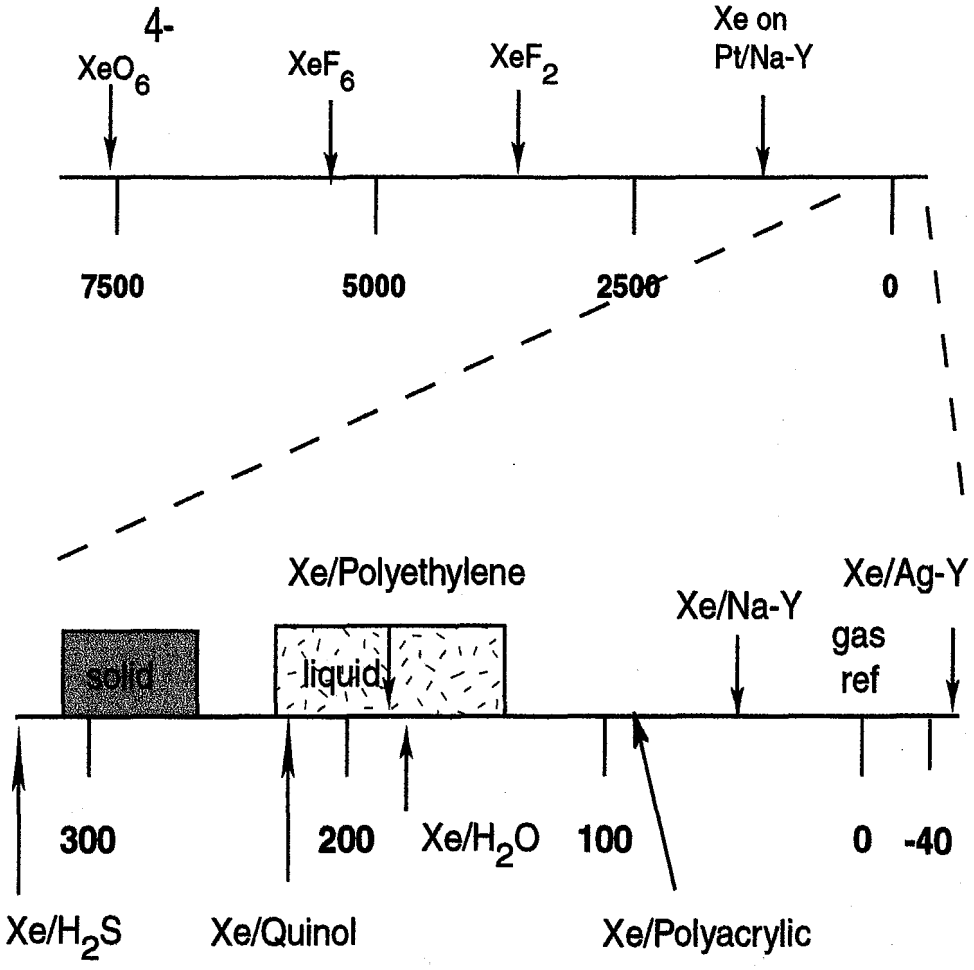

Figure 1.1 Isotropic chemical shift range of xenon in different chemical environments. The chemical shifts are referenced to dilute xenon concentration (0 ppm).

References

1. F. Bloch, W. W. Hansen, M. Packard, *Phys. Rev.* **69**, 127, (1946)
2. E. M. Purcell, H. C. Torrey, and R. V. Pound, *Phys. Rev.* **69**, 37 (1946)
3. C. P. Slichter, Principles of Magnetic Resonance, Harper and Row, New York (1963)
4. A. Abragam, Principles of Nuclear Magnetism, Clarendon Press, Oxford (1961)
5. R. R. Ernst, G. Bodenhausen, and A. Wokaun, Principles of Nuclear Magnetic Resonance in One and Two Dimensions, Clarendon Press, Oxford (1987)
6. E. Fukushima and S. B. W. Roeder, Experimental Pulse NMR: A Nuts and Bolts Approach, Addison-Wesley, Reading, (1981)
7. P. Mansfield and P. G. Morris, NMR Imaging in Biomedicine, Academic Press, New York (1982)
8. P. T. Callaghan, Principles of Nuclear Magnetic Resonance Microscopy, Clarendon Press, Oxford (1991)
9. M. T. Vlaardingerbroek and J. A. den Boer, Magnetic Resonance Imaging, Springer-Verlag, Berlin (1999)
10. D. O. Kuethe, A. Caprihan, E. Fukushima, and R. A. Waggoner, *Magn. Reson. Med.* **39**, 85 (1998)
11. M. J. Lizak, M. S. Conradi, and C. G. Fry, *J. Magn. Reson.* **95,** 548 (1991).
12. W. Happer, *Rev. Mod. Phys.* **44**, 169 (1972)
13. E. Stolz, M. Meyerhoff, N. Bigelow, M. Leduc, P. J. Nacher and G. Tastevin, *Appl. Phys. B*, **63**, 629 (1996)
14. R. J. Gillespie and G. J. Schrobilgen, *J. Inorg. Chem.* **13**, 2370 (1974)

15. D. D. DesMarteau and M. Eisenberg, *J. Inorg. Chem.* **11**, 2641, (1972).

16. P. J. Barrie and J. Klinowski, *Prog. Nucl. Magn. Reson. Spectrosc.* **24**, 91 (1992)

17. T. Ito and J. Frassard, 5th International Conference on Zeolites; Heyden: Naples, p. 150 (1980)

18. J. A. Ripmeester and D. W. Davidson, *J. Mol. Struct.* **75**, 67 (1981)

19. K. W. Miller, N. V. Reo, D. P. Stengle, T. R. Stengle, and K. L. Williamson, *Proc. Natl. Acad. Sci. USA* **78**, 4946 (1981)

Chapter 2

Production of laser-polarized ^{129}Xe

Introduction

In 1949 Alfred Kastler proposed the idea of "optique pompage" (1), which suggested that it was possible to transfer angular momentum from polarized resonance light to an alkali metal atomic system leading to non-thermal population distributions. Following the first successful observations of these population imbalances in the early fifties (2), later work (3) has shown that spin-exchange optical pumping of mixtures of alkali-metal vapors and noble gases can be used to efficiently polarize the nuclei of the noble-gas atoms. As a result, the technique of spin-exchange optical pumping became the basis for many applications in chemistry and physics that require large numbers of spin-polarized nuclei. Among the various applications are Magnetic Resonance Imaging (MRI) of the lungs with the laser-polarized ^{3}He and ^{129}Xe (4), studies of gas and surface interactions (5), visualization of gas flow and diffusion in porous materials (6).

Theory

There are two main steps involved in the spin-exchange optical pumping process: the first is the production of electronic spin-polarization and the second is the transfer of electron spin polarization of alkali metal to nuclear spin polarization of noble gases.

Step 1. Optical pumping

Optical pumping is a very complex phenomenon, especially at low gas pressures where the hyperfine structure of the absorption lines is well-resolved (7). In most applications of optical pumping, however, the following diagram (Fig. 2.1) approximates the process of optical pumping under typical experimental conditions. Circularly polarized laser light with a wavelength of 794.7 nm excites the D_1 line of alkali metal atoms, resulting in transition from the $^2S_{1/2}$ ground state to the first excited state $^2P_{1/2}$. This has the effect of depopulating one of the $^2S_{1/2}$ states (which state is depleted depends on whether the circular polarization of the laser light is right-handed or left-handed). Collisions with the noble gas atoms rapidly equalize the sublevel populations of the excited states. The quenching collisions with N_2 molecules re-populate both ground-state sublevels with nearly equal probability. The net result of the optical pumping cycle is to leave one of the ground state levels highly polarized, since the relaxation time of the ground state is relatively long (up to 1 second).

There are several subtleties regarding the above picture that warrant further attention. All non-radioactive alkali atoms have nuclear spins $I \neq 0$, and have hyperfine energy splittings in both the ground and excited states. The total density of nitrogen and noble gas exceeds 1 atm in most optical pumping applications, thus the pressure broadening of the absorption line results in unresolved alkali-metal hyperfine structure.

As a result the optical pumping process can be discussed in terms of spin states of the electron, as though the nuclear spins are zero. Radiative emission of photons by the alkali-metal atoms is nearly unpolarized and can be reabsorbed by the Rb atoms, thereby optically depumping the atoms. High Rb vapor densities are necessary for spin-exchange optical pumping experiments, in order to keep spin-exchange rates large enough to attain high polarization. Thus the thickness of the cell is large enough for photons to be scattered several times and depolarize several atoms before escaping from the cell (8). The N_2 quenching gas removes this damaging depolarization mechanism, which is also known as radiation trapping mechanism (9).

Step 2. Spin-exchange

The most important advance in the applicability of optical pumping is spin-exchange, which can polarize species that cannot be pumped directly. During collisions with rare gas atoms, spin polarization may be transferred from the alkali metal to the rare gas molecule. Grover at Litton Industries (10) and later Happer and coworkers at Princeton (11) showed that optical pumping could be used to dramatically increase the nuclear spin polarization of ^{129}Xe and ^{3}He. The key process in spin-exchange optical pumping is collisional transfer of angular momentum, which occurs either while atoms are bound in van der Waals complexes or in simple binary collisions between the atoms. For ^{3}He, binary collisions dominate the spin relaxation, and the contribution from van der Waals molecules is negligible. For heavy atom such as xenon, the contributions of van der Waals molecule to the spin-relaxation can greatly exceed the contribution of binary collisions. For example, at pressures of a few tens of Torr, the collisional lifetime of

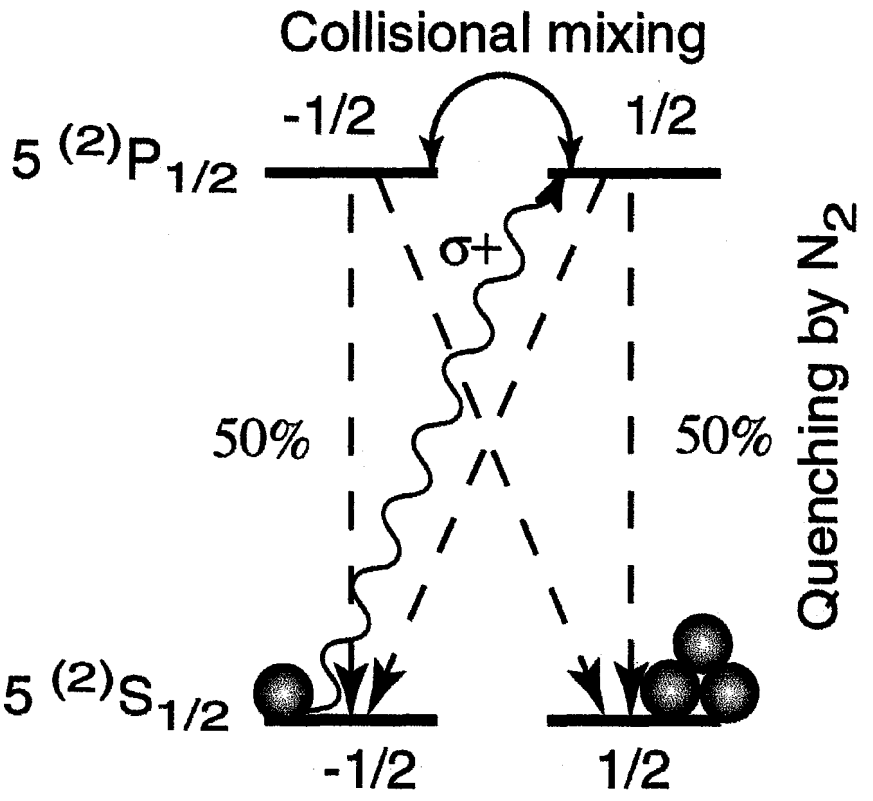

Figure 2.1 Spin sublevels and collisional processes involved in the optical pumping of alkali-metal atoms with circularly polarized D_1 light. For Rb atom right circularly polarized light at 754.7 nm causes transitions from the $m_s = -1/2$ ground state to the $m_s = +1/2$ excited state.

Xe-Rb complex is on the order of 10^{-9} seconds, whereas He-Rb has a lifetime of about 10^{-12} seconds. The spin-exchange is more efficient for large rare gas atoms like xenon because the spin exchange efficiency varies as the interaction time squared.

A schematic figure of a van der Waals molecule is shown in Figure 2.2. The following Hamiltonian during the van der Waal collision has been successfully used to account for all observed phenomena in this system (12):

$$H_a = A\mathbf{I} \cdot \mathbf{S} + \gamma \mathbf{N} \cdot \mathbf{S} + \alpha \mathbf{K} \cdot \mathbf{S} \qquad (2.1)$$

In this equation A is the isotropic hyperfine interaction between the Rb electron spin (S) and Rb nuclear spin (I), γ is the spin-rotation constant for the complex, and α is the isotropic hyperfine interaction between the rubidium electron spin and the nuclear spin of xenon (K). The first term is hyperfine interaction, which has no effect on optical pumping and is also ignored in the description of step 1 under the assumption of high-pressure conditions (close to 1 atm). The second term, $\mathbf{N} \cdot \mathbf{S}$, is the spin-rotation interaction, which transfers polarization from the electron spin to the translational degrees of freedom of the atoms, thus acting as a primary relaxation mechanism for Rb and contributing a significant loss pathway in xenon nuclear polarization. The spin-rotation interaction arises from precession of the electron spin about magnetic fields induced by motion of the nuclei (in the case of heavy atom like xenon, the spin-rotation interaction arises mostly from the xenon gas core, whereas for He the dominant source is inside the alkali-metal core). Spin relaxation via spin rotation can also occur in collisions with the nitrogen quenching gas. Other sources of relaxation during optical pumping spin-exchange processes include Rb-Rb collisions, magnetic field inhomogeneities, cell wall

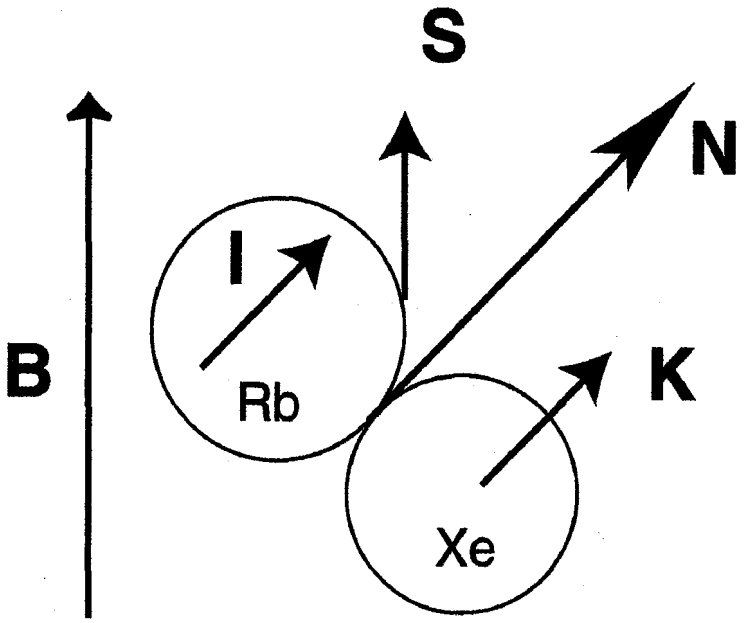

Figure 2.2 Schematic Rb-Xe van der Waals complex, with the various angular momenta labeled. N represents the rotational angular momentum of the complex.

relaxation, noble gas self-relaxation resulting from dipole-dipole interaction (dominant for ^{3}He) and molecular spin-rotation interaction (dominant for ^{129}Xe). The third term in this Hamiltonian is "Fermi contact" interaction, which contains the exchange terms, responsible for polarization transfer from rubidium to xenon. This term can be expanded in spherical basis and written as

$$\alpha \mathbf{K} \cdot \mathbf{S} = 8\,\pi/3\,\gamma_e\gamma_{xe}\,|\Psi(0)|^2\,[K_zS_z+1/2(K_+S_- + K_-S_+) \qquad (2.2)$$

where $K_+S_- + K_-S_+$ constitute the "flip-flop" terms that allow spin exchange. The exchange depends strongly on the probability for finding unpaired electron spin density at the xenon nucleus, denoted $|\Psi(0)|^2$. This term is particularly large for xenon due to polarization of the xenon core electron shells during a collision (13).

It would be convenient to polarize directly a system of interest, rather than polarize a secondary species and transfer the polarization. An ideal molecule must have an accessible transition with selection rules that will allow the establishment of non-thermal populations in order to be optically polarized directly. Secondly, the relaxation time of the polarized state must be sufficiently long to allow the accumulation of polarization. Alternatively, in order to spin-exchange a system with optically polarized Rb, it must not react with rubidium vapor (not necessarily a trivial requirement!). There must be some probability of finding the Rb electron at the nucleus of the system of interest and the relaxation time again must be sufficient for the accumulation of polarization. ^{3}He is the only noble gas that can be easily polarized directly by pumping a metastable state (14).

Experimental Approach

There are several experimental approaches for optical pumping of noble gases via alkali-metal spin exchange. They can be broadly divided into two categories: continuous flow mode and batch mode. Historically, batch method was employed before the continuous flow methods, perhaps because the former does not require high power lasers (~100W), which were not available until recently. What follows is the description of the two experimental approaches and their suitability for various experiments.

Batch mode production of laser-polarized ^{129}Xe

The batch method is much simpler to implement than the continuous flow approach and is usually used for producing small amounts of polarized noble gas. A schematic picture of the classic "batch" optical pumping apparatus is shown in Figure 2.3. A narrow bandwidth continuous wave laser (in our set-up 1. 5 W Ti:sapphire laser pumped by an 11-W argon ion laser) produces a beam tuned to the D_1 resonance of the alkali metal vapor. The beam is circularly polarized with a quarter-wave plate, allowing only right hand circularly polarized light to enter the pump cell. Inside a magnetic field (~30G) produced by a Helmholtz coil pair resides a glass optical pumping cell (volume 20-50 cc) containing ~100-300 torr of xenon, a small amount of nitrogen gas, and a small amount of Rb metal (1 drop). The pumping cell is heated to ~ 60-130 degrees Celsius to change Rb metal from solid to vapor phase. During optical pumping the line is constantly evacuated to about 10^{-5} torr to minimize oxygen contamination of the pumping mixture during transfer to the sample. Once the optical pumping process has been completed, the cell is cooled to condense the Rb vapor, and the xenon is transferred to the sample via liquid nitrogen cryopumping. The dewar containing liquid

nitrogen for cryopumping has small permanent magnets in order to have frozen polarized xenon constantly exposed to a strong magnetic field (>500 G). If the external field is too weak, the polarized xenon will rapidly relax through dipolar couplings between ^{129}Xe and ^{131}Xe nuclei (15).

Batch mode production of xenon is suitable for many experiments including polarization transfer in solution, imaging, in vivo applications, etc. Conventional NMR experiments that utilize 90° pulses, however, can not be performed using xenon polarization obtained in batch mode. The application of each 90° pulse destroys non-Boltzmann polarization created by laser, and the spins relax back to thermal equilibrium via the spin-lattice relaxation mechanism providing virtually no detectable magnetization. Thus acquisition pulses have to be set at a small tipping angle to avoid consuming all of the polarization at once; the application of each radiofrequency (rf) observation pulse of tipping angle α reduces the remaining z component only by a factor of $\cos(\alpha)$. Since the decrease in longitudinal magnetization can also cause artifacts in images and spectra, this method is not very well suited for multi-dimensional experiments or signal averaging.

Continuous flow production of laser-polarized ^{129}Xe

The continuous flow method was developed initially by Haake et al (16) in order to overcome the problem of the non-renewable nature of xenon polarization (a similar idea was also introduced by Driehuys and coworkers (17)). An excellent way to replenish longitudinal magnetization is to introduce continuously fresh polarized xenon to the

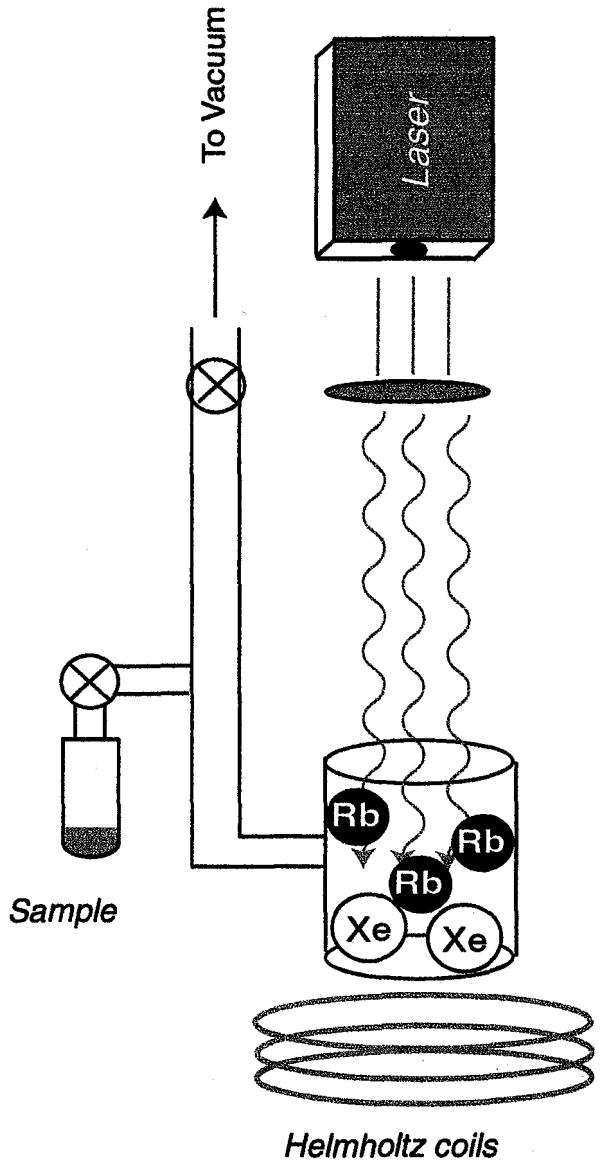

Figure 2.3 Production of laser-polarized xenon in a batch mode.

sample area; this use of laser-polarized xenon under continuous flow, however, requires fast optical pumping techniques since xenon has to be polarized 'on the fly'. This has become possible with the development of high-power laser diode arrays. The laser that is used in continuous flow set-up is rated at about 130 watts, almost a factor of a 100 more than the laser power needed in the batch method. The continuous flow system has two different modes of operation – continuous "closed loop" flow where xenon, after reaching the detection region enters the pumping cell and a continuous "open" flow mode where xenon, after reaching the detection region is purged into the atmosphere. The former mode does not waste any xenon during many hours of experiment, however the sample must be degassed in order to protect moisture-sensitive Rb in the pumping cell. Continuous "open" flow allows investigation of wet samples, however the amount of xenon that is consumed can be prohibitively expensive. Since the "closed loop" flow was used in most of the experiments described in this manuscript, the description below will refer to that particular arrangement.

The gas circulation system (Fig. 2.4) is a closed loop, with 3 main components, connected together by Teflon™ tubing. The heart of the continuous flow apparatus is the pumping cell (**1**), which contains 2 chambers: a smaller chamber for the solid Rb reservoir and a larger chamber for optical pumping where laser light interacts with Rb vapor and the spin-exchange between Rb and xenon takes place. The large chamber is positioned in the fringe field of the superconducting magnet (with magnetic field lines parallel to the laser light). For better magnetic field homogeneity it is also possible to have the pumping cell inside a Helmholtz coil (the entire apparatus has to be far enough from the magnet in order to avoid magnetic field interference). The temperature at the

Rb reservoir is maintained at about 150-200 °C by a small oven, although after several hours of optical pumping process the heat generated by the laser is enough to maintain enough Rb in the vapor phase without an external oven.

The gas mixture is circulated through the system via a pressure and vacuum resistant pump (**2**), producing a maximum flow rate of ca. 35 ml/s through 4 mm tubing. The polarized gas enters the sample region (**3**), which is located inside the NMR/MRI probe inserted into the superconducting magnet. The gas mixture is cooled in a condenser to remove Rb before entering the detection zone inside the superconducting magnet. After the detection zone, the mixture re-enters the gas circulation pump to start a new cycle. The entire loop has to be evacuated to about 10^{-4} Torr before it is filled with a desirable mixture of gases.

The maximum polarization that was obtained with the continuous flow apparatus in our experiments was about 8 %. In order to further improve the optical pumping efficiency under continuous flow several important issues need to be addressed: composition of the gas mixture, gas flow rate, and magnetic field inhomogeneity. These parameters and their effect on xenon polarization are discussed below.

Gas mixture composition

Light radiated by the alkali-metal atoms is nearly unpolarized and can be reabsorbed by the Rb atoms, thereby optically *depumping* the atoms. Since high Rb vapor pressures are necessary for spin-exchange optical pumping, the cell is usually many optical depths thick, and a single photon can be scattered several times and depolarize several atoms before escaping from the cell (8). The nitrogen, which is chemically inert,

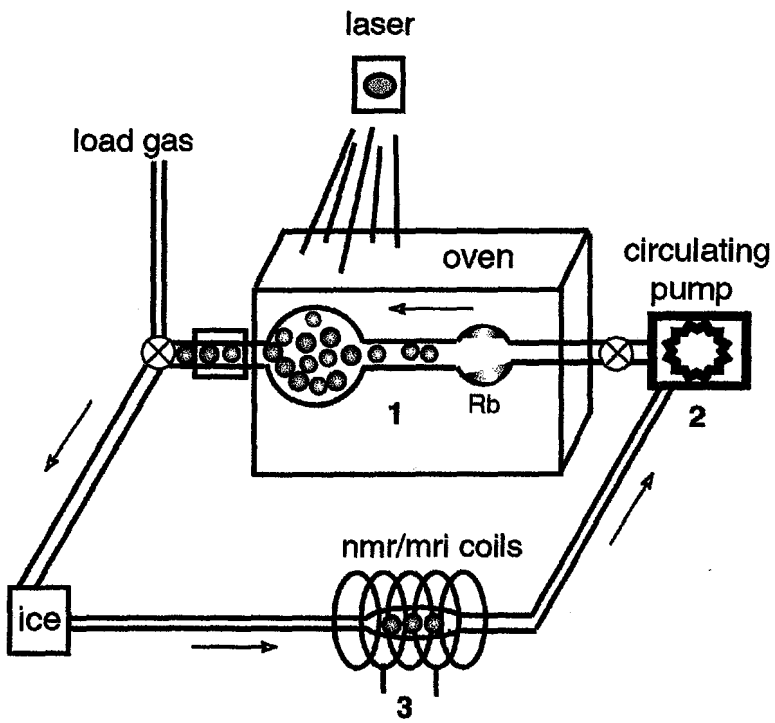

Figure 2.4 Gas circulation system delivering polarized xenon into the detection region via steady-state flow.

suppresses re-radiation of light by quenching the excited atoms. Thus addition of N_2 to xenon should increase the efficiency of the optical pumping process. In order to investigate this effect under continuous flow conditions xenon pressure is kept constant at 1 atm with N_2 gas added in small increments, and ^{129}Xe NMR signal area is measured after each addition. Figure 2.5 displays area of the NMR signal as a function of amount of N_2. The build-up of polarization in Figure 2.5 indicates that a 1:1 ratio seems to give the largest increase in polarization (a factor of 3), although it is clear that even half that amount of nitrogen gives a significant increase. After 1:2 xenon to nitrogen ratio is reached, there seems to be no benefit in additional amount of N_2.

Flow rate

In order to investigate the effect of gas flow on the efficiency of the optical pumping process, flow rate is increased in small increments and the area of the ^{129}Xe NMR signal is measured. Figure 2.6 shows the effect of the flow rate on the NMR signal area at constant temperature ~ 300 F. In order to rule out the possibility of a reduction of signal intensity due to flow (excited spins being washed out of the sample region) the flow was stopped and signal was recorded after 60 seconds for each flow increment. The rate of decay with a stopped flow measurement yielded the same rate of signal decay as in the Fig. 2.6.

In order to explain the dependence of the NMR signal on gas flow velocity we need to examine the crucial components of the optical pumping process that contribute to the spin polarization.

The average nuclear spin polarization, P_{xe}, obtained after a certain residence time,

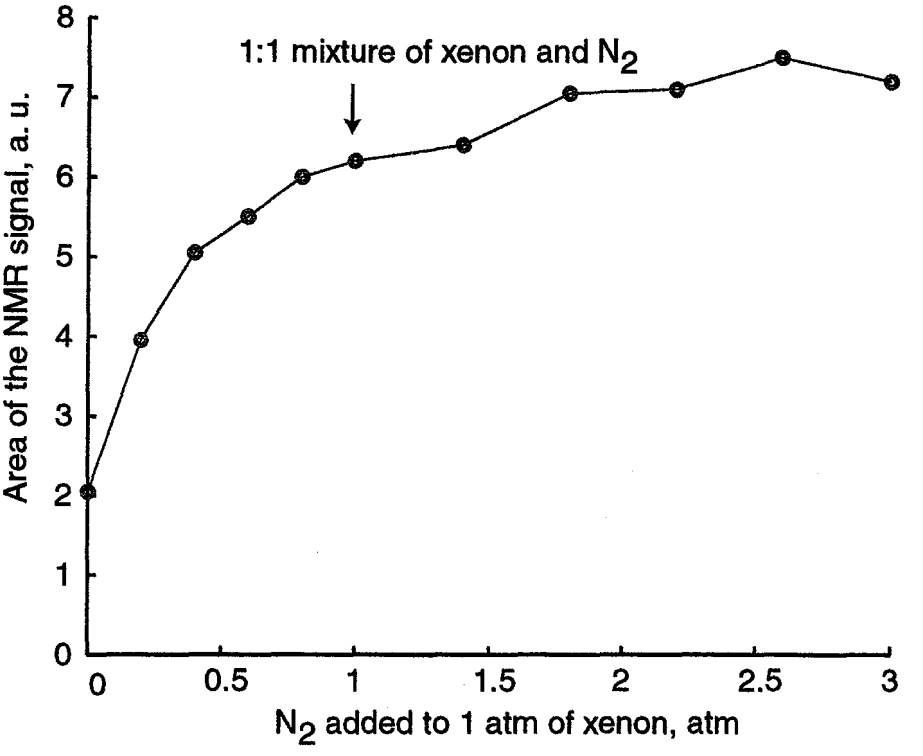

Figure 2.5 Area of the NMR signal vs of amount of N_2. The xenon pressure is kept constant at 1 atm.

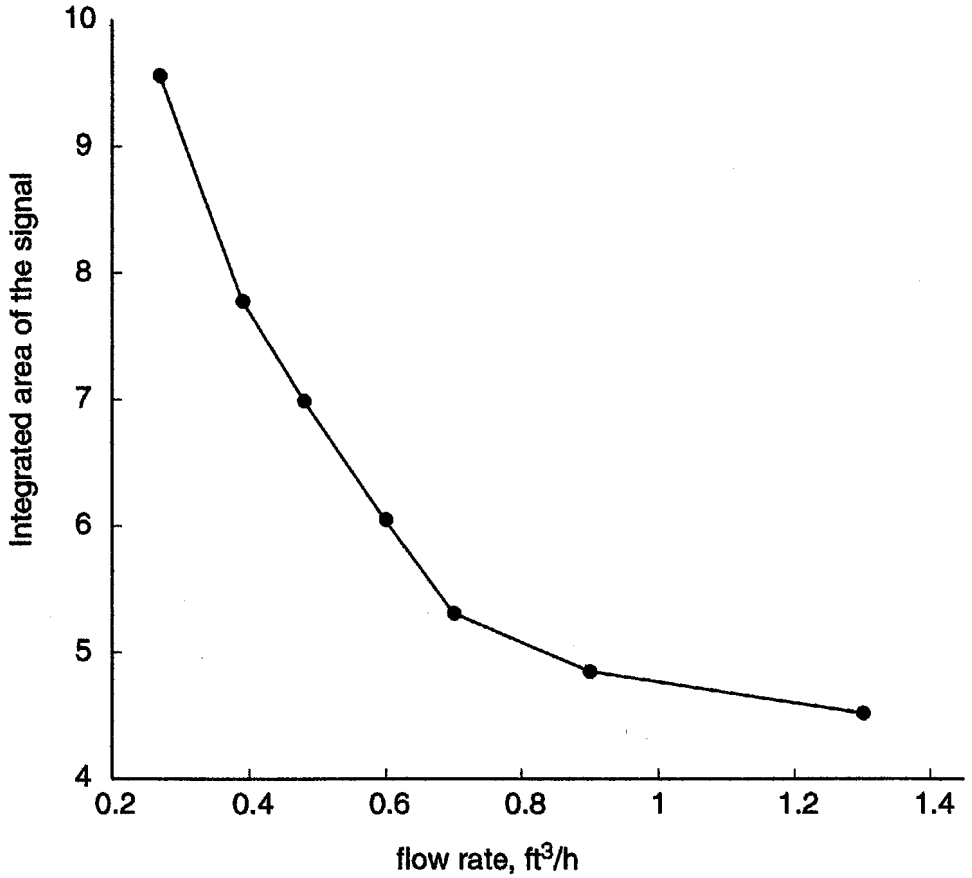

Figure 2. 6 ^{129}Xe NMR signal intensity vs flow rate (in cubic feet per hour). The exponential reduction in xenon polarization is attributed to a decrease in residence time of xenon in the pumping cell according to Eq. 2.3.

t_p, of the xenon atoms in the pumping cell is (18)

$$P_{Xe} = \frac{\rho_{se}}{\rho_{se} + \Delta\rho_1} P_{Rb}\left[1 - e^{-(\rho se + \Delta\rho)t_p}\right] \tag{2.3}$$

where P_{Rb} is the average electron spin polarization of the Rb atoms, ρ_{se} is the spin-exchange rate and $\Delta\rho_1$ includes all the other contributions to the longitudinal relaxation rate of the noble gas nuclei under optical pumping conditions excluding ρ_{se}. From Eq. (2.3) we can see that the polarization is exponentially decreasing as a function of the residence time of xenon in the pumping cell, t_p. This trend agrees with the experimental data in Figure 2.6. However, for flow rates slower than 0.2 ft^3/h we observe a decrease in the NMR signal due to relaxation effects.

Magnetic Field Inhomogeneity

The optical pumping process described above is carried out in the fringe field of the superconducting magnet. The magnetic field gradient is approximately 0.0015 T/cm^{-1} at the chosen position where B_{ext} = 0.026 T. The inhomogeneity of the external magnetic field contributes to the longitudinal relaxation rate as (19),

$$\rho_1 \approx \frac{2}{3}\tau_c < v >^2 \left(\frac{\nabla\Omega_\perp}{\omega}\right)^2 \tag{2.4}$$

where ω as the Larmor frequency of xenon, $\Omega_\perp$ is the Larmor precession frequency due to the transverse portion of the magnetic-field inhomegeneity. The pre-factor, 2/3 $<v^2>\tau_c$, has the dimension of a diffusion coefficient and corresponds to ca 2D, where D denotes xenon self-diffusion coefficient. Xenon diffusion coefficients of ca 0.08 - 0.38 cm^2/s are expected for xenon at total gas pressures of ca 0.2 - 1 MPa at 423 K. Therefore spin-lattice relaxation values of ca 300-2000 s would result from the inhomogeneity of the

magnetic field according to Eqn (2.4). This means that longitudinal relaxation caused by pure gas diffusion is negligible. However, additional relaxation may be induced by the displacement due to gas flow.

Conclusion

Although the two methods described above are based on the same phenomena of spin exchange optical pumping, the NMR applications are quite different for each of the modes. The advantage of the batch mode is that it yields higher xenon polarization (the maximum polarization of about 70%, observed in batch mode (20)); the continuous flow is also not suitable for solution applications (one should not circulate xenon through anything containing moisture or other impurities that can destroy Rb in the reservoir). As a result batch mode seems to be the method of choice for experiments such as xenon polarization transfer to macromolecules in solution, where the amount of xenon polarization is crucial to the success of the experiment. Due to the non-renewable nature of laser-polarized xenon, however, this method is not suitable for multi-dimensional experiments or traditional NMR experiments that utilize hard 90° excitation pulses.

References

1. A. Kastler, *J. Phys. Radium*, 11, 255 (1950)
2. J. Brossel, A. Kastler, and J. Winter, *J. Phys. Radium*, 13, 668 (1952)
3. M. R. Bouchiat, T. R. Carver, and C. M. Varnum, *Phys. Rev. Lett.* 5, 373 (1960)
4. B. Saam, D. A. Yablonsky, D. S. Gierada, and M. S. Conradi, *Magn. Reson. Med.* **42**, 507 (1999).
5. D. Raftery, H. Long, T. Meersmann, P. J. Graninetti, L. Reven, and A. Pines, *Phys. Rev. Lett.* **66**, 584 (1991)
6. L. G. Kaiser, T. Meersmann, J. W. Logan, and A. Pines, *Proc. Natl. Acad. Sci. USA* **97**, 2414 (2000)
7. W. Happer, *Rev. Mod. Phys.* **44**, 169 (1972)
8. D. Tupa and L. W. Anderson, *Phys. Rev.* A **36** , 2142 (1987)
9. N. D. Bhaskar, M. Hou, B. Suleman, and W. Happer, *Phys. Rev. Lett.* **44**, 930 (1979)
10. B. C. Grover, *Phys. Rev. Lett.* **40**, 391 (1978)
11. W. Happer, E. Miron, S. Schaefer, D. Schreiber, W. A. Wijngaarden, and X. Zeng, *Phys. Rev.* A, **29**, 3092 (1984)
12. N. D. Bhaskar, W. Happer, M. Larsson, and X. Xeng, *Phys. Rev. Lett.* **50**, 105 (1983).
13. R. M. Herman, *Phys. Rev.* **137**, 1062 (1965)
14. G. K. Walters, F. D. Colegrove, and L. D. Schearer, *Phys. Rev. Lett.*, **8,** 439 (1962)
15. M. Gatzke, G. D. Cates, B. Driehuys, D. Fox, W. Happer, and B. Saam, *Phys. Rev. Lett* **70,** 690 (1993)

16. M. Haake, A. Pines, J. A. Reimer, and R. Seydoux, *J. Am. Chem. Soc.* **119**, 11711 (1997)

17. B. Driehuys, G. D. Cates, E. Miron, K. Sauer, D. K. Walther, and W. Happer, *Appl. Phys. Lett.* **69**, 1668 (1996)

18. T. E. Chupp, M. E. Wagshul, K. P. Coulter, A. B. Mcdonald, and W. Happer, *Phys. Rev.* C **36**, 2244 (1987)

19. L. D. Schearer and G. K. Walters, *Phys. Rev.* A **139**, 1398 (1965)

20. U. Ruth, R. Hof, J. Schmidt, D. Fick, and H. J. Jänsch, *Applied Physics* B **68**, 93 (1999)

Chapter 3

NMR imaging and microscopy of laser-polarized xenon

Introduction

NMR imaging (referred to in the medical community as MRI) is the most significant innovation in diagnostic imaging since the discovery of X-rays. In 1973, Lauterbur (1) reported the first reconstruction of a proton spin density map using nuclear magnetic resonance. In the same year Mansfield and Grannell (2) independently demonstrated the Fourier relationship between the spin density and the NMR signal acquired in the presence of a magnetic field gradient. Besides having an enormous impact on the medical community as a diagnostic tool, NMR imaging is also employed in the biological, food technology and material sciences. Callaghan in his fundamental work (3) further defines NMR microscopy as MRI at a resolution equal to or less than 100

micrometers. Although NMR microscopy cannot compete with the resolution of optical microscopy, it offers an image contrast that can be made sensitive to a specific chemical environment, relaxation rate, flow rate and diffusivity. In addition NMR microscopy is non-destructive and inherently three dimensional, allowing, in principle, the total density of the system of interest to be determined.

Until recently gas phase multidimensional NMR microscopy was not possible due to very poor sensitivity. By using laser-polarized ^{129}Xe it is possible to perform multidimensional NMR experiments in the gas phase. What follows is a short description of the basic theory of NMR microscopy, with a discussion of contrast mechanisms available. Gas phase imaging applications in porous and lipophilic samples are demonstrated along with the discussion of the dynamic imaging contrast derived from continuous flow of laser-polarized xenon gas.

Basic theory of NMR microscopy

In conventional NMR spectroscopy it is desirable to have very high homogeneity of the magnetic field in the sample region in order to ensure that all nuclei have identical behavior. In contrast NMR imaging requires a linear magnetic field gradient superimposed on the main field, B_0. This static magnetic field gradient, **G**, is defined as the **grad** of the pulsed gradient field component parallel to B_0. Thus the local Larmor frequencies of the spins will show a linear spatial dependence, which is defined as

$$\omega(\mathbf{r}) = \gamma B_0 + \gamma \mathbf{G} \cdot \mathbf{r} \qquad (3.1)$$

In equation (3.1) the scalar product $\mathbf{G} \cdot \mathbf{r} = G_x x + G_y y + G_z z$ represents the incremental field at location **r**, resulting from the superimposed field gradient **G**. In the rotating frame of reference (ignoring the precession due to the main polarizing field B_0), the complex time-dependent NMR signal evolves as $\exp(i\gamma\omega t) = \exp(i\gamma \mathbf{G} \cdot \mathbf{r}t)$. In a volume element ("voxel") dxdydz the signal dS(t) then becomes

$$dS(t) \propto M_{xy}(r, t)\exp[i\gamma(G_x x + G_y y + G_z z)t]\, dxdydz \tag{3.2}$$

where Mxy (r,t) is the magnetization density at location **r**. The total signal is then obtained by spatial integration across the object. Unless the gradients have constant amplitude, products $G_x t$, $G_z t$ and $G_y t$ are integrals over time. We can define the wave vector (also denoted 'spatial frequency vector') as follows:

$$k(t) = (2\pi)^{-1} \gamma \int_0^t G(t')dt' \tag{3.3}$$

where G(t) is the time-dependent spatial encoding gradient. From equation 3.3 it is evident that **k**(t) has the units of m^{-1} (it thus measures 'reciprocal space'). Rather than expressing the NMR signal in terms of magnetization, which is modulated by the relaxation terms in a manner specific to the excitation scheme used, it is customary to express it as a function of the spin density, which is equivalent to ignoring relaxation. We can rewrite the equation (3.2) in spatial frequency format. For an object of spin density p(r) the spatial frequency signal S(k) is thus given by

$$S(\mathbf{k}) = \iiint_{\text{object}} \rho(\mathbf{r}) \exp[i2\pi \mathbf{k} \cdot \mathbf{r}]\, d\boldsymbol{r} \tag{3.4}$$

Pictorially, the spatial frequency may be regarded as the phase rotation per unit length of object that the magnetization experiences after being exposed to a gradient G(t)

for some period t. It is easy to see from equation 3.4 that S(k) and r(r) are Fourier transform pairs, thus

$$\rho(\mathbf{r}) = \iiint_{k-space} S(k) \exp[-i2\pi \mathbf{k} \cdot \mathbf{r}] \, d\mathbf{k} \qquad (3.5)$$

Hence, the spatial spin density at any one location can be obtained as the inverse Fourier transform of the spatial frequency signal. The path the spatial frequency vector follows during execution of the pulse sequence is, of course, determined by the time-dependent gradient waveforms.

Equations 3.4 and 3.5 are the fundamental equations of NMR imaging (3). While conceptually correct, they do not indicate how to fill the void between the theory and practice in imaging. Depending on the experimental conditions used (i.e. delays, gradient and RF pulses), the signal S(**k**) will be modified such that nuclei with some distinctive property (chemical shift, relaxation behavior, dipolar or scalar coupling, flow or diffusion, etc.) will have an unequal weighting in the signal. Including such effects, equation 3.4 can be written as

$$S(\mathbf{k}) = \iiint_{object} \rho(\mathbf{r}) E_c(\mathbf{r}) \exp[i2\pi \mathbf{k} \cdot \mathbf{r}] \, d\mathbf{r} \qquad (3.6)$$

where $E_c(\mathbf{r})$ is the normalized and combined contrast factor (4). Thus, image reconstruction after Fourier Transform returns $\rho(\mathbf{r})E_c(\mathbf{r})$. $E_c(\mathbf{r})$ is the product of several factors and is given by

$$E_c(\mathbf{r}) = E_c(T_x)E_c(\delta_i)E_c(\mathbf{q}) \qquad (3.7)$$

where $E_c(T_x)$ (x=1,2 or 1ρ) is the contrast factor representing the effects of spin-lattice, spin-spin or spin-lattice relaxation in the rotating frame. $E_c(\delta_i)$ represents chemical shift

effects and $E_c(\mathbf{q})$ is the contrast factor for molecular motion, which contains contributions from self-diffusion and flow. The factors in equation 3.7 are primary contrast factors as they can be included in the Bloch equation (4). In addition to the primary contrast factors, there are also secondary contrast factors such as temperature and susceptibility differences, which appear as perturbations of the primary contrast factors.

The imaging experiment

There are three common ways in which a gradient can be used to impart a spatial dependence into the acquired NMR signal: slice selection, frequency encoding, and phase encoding. Figure 3.1A illustrates the 2D Fourier Imaging (spin warp) pulse sequence containing all three components. Spin warp versions of 2-D and 3-D Fourier imaging continues to be the standard imaging technique of choice for MRI applications since its introduction in 1980 (5).

A slice is selected by applying a selective ("soft") RF pulse in the presence of the slice gradient (i.e., G_z). The slice thickness (Δz) will depend on the strength of the applied gradient and the frequency selectivity of the RF pulse, $\Delta\omega_{rf}$

$$\Delta z = \frac{\Delta\omega_{rf}}{\gamma G_z} \tag{3.8}$$

The magnetization components within the frequency range are completely dephased immediately after the RF pulse, thus it is necessary to apply a negative gradient for a short period of time to refocus the magnetization. This (two-dimensional) slice is then sampled using two other orthogonal gradients. If a gradient (i.e., Gy) is applied for a fixed time, t,

and then is switched off prior to signal acquisition, then the phase of the signal, ϕ, is spatially dependent,

$$\phi(\mathrm{r}) = \int_0^t (\gamma B_0 + \gamma \mathbf{G} \cdot \mathbf{r})\, dt \tag{3.9}$$

with the assumption that B_0 is effectively homogeneous throughout the sample, thus not contributing to the spatial dependence. During the detection period, the FID is frequency-encoded owing to the presence of the third orthogonal gradient (i.e. the read gradient, G_x). A series of FIDs are collected while stepping through Gy by a set amount (ΔG_y) in successive experiments. The choice of x, y and z gradients for read, phase and slice selection is purely arbitrary and any permutation is possible. Thus, this method samples **k**-space in a Cartesian coordinate system in the *xy* plane as depicted in Fig. 3.1B. When $k_x = 0$ and $k_y \neq 0$, the spins evolve in k-space along the y-axis as the time advances during the phase period. Subsequently, when $k_x \neq 0$ and $k_y = 0$, the signal is mapped along the x-axis during the read period (notice that the use of the precursor read gradient and application of the hard 180° pulse allows full echo sampling, with $k_x = 0$ being in the center of the echo). It is obvious that any imaging scheme will work as long as k-space is appropriately sampled, even without k-space confined to a Cartesian grid (3, 6, 7).

The discrete sampling of k-space, of course, requires compliance with the Nyquist criterion which demands that two or more samples be taken per phase cycle, i.e. the highest spatial frequency $k_{i,max}$ ($i = x,y$) sampled has to obey the relationship

$$k_{i,max} \cdot R_i = N_i \tag{3.10}$$

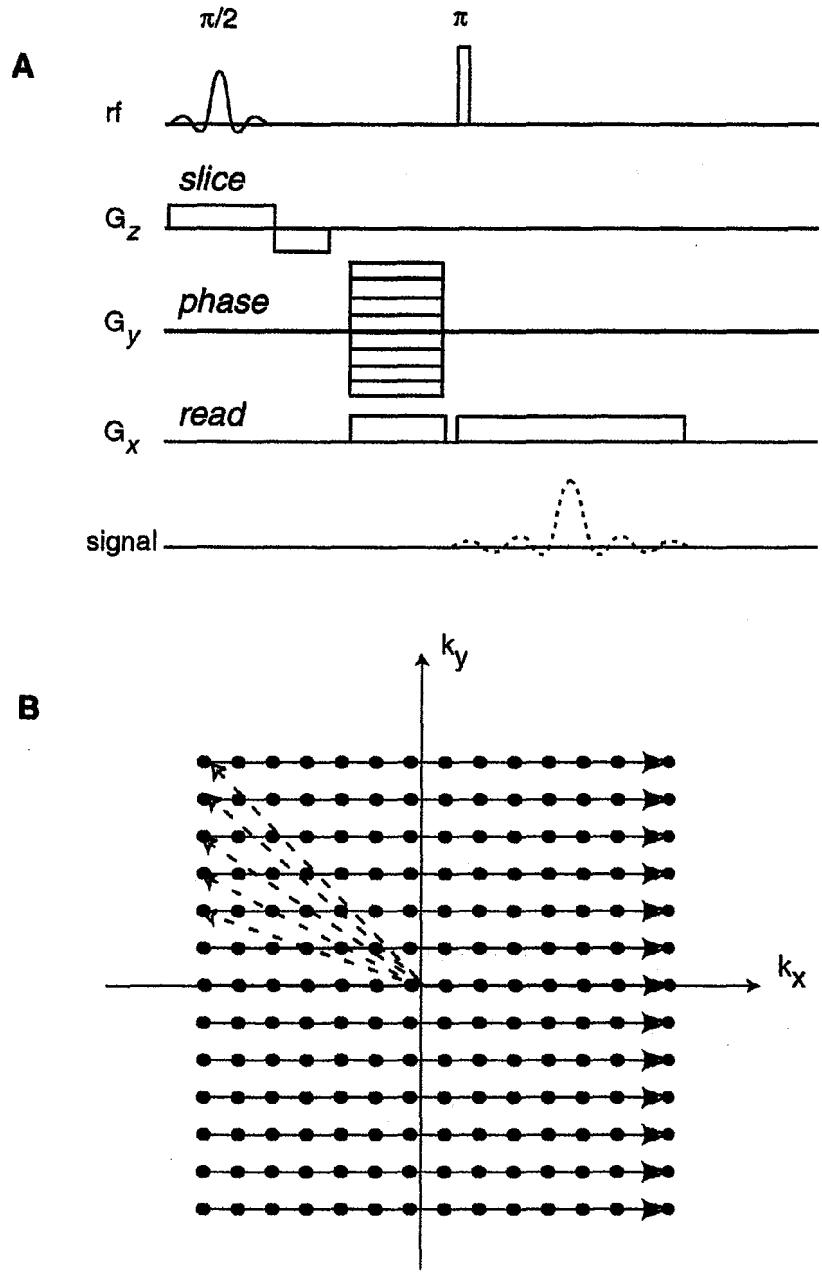

Figure 3.1 A. Generic 2D Fourier Imaging (spin warp) pulse sequence with full echo sampling. **B.** Sampling of the k-space (phase encoding period is represented by the dashed lines, and frequency encoding period is represented by solid lines). Data points are acquired at each point.

where R_i and N_i represent the maximum spatial distance (often referred to as field of view – FOV) and number of data samples, respectively. The FOV in each direction are independent of each other and can be defined as $R_i=\Delta R_i \cdot N_i$, where ΔR_i is the digital resolution. The digital resolutions, ΔR_i, in frequency encoded x direction and phase encoded y direction are given by

$$\Delta R_x = \frac{2\pi}{\gamma G_x(\Delta t_x)N} \tag{3.11}$$

and

$$\Delta R_y = \frac{2\pi}{\gamma(\Delta G_y)t_y N} \tag{3.12}$$

where Δt_x is the dwell time between data points in the FID, t_y is the time during which phase encoding gradient is on and ΔG_y is the step size of the gradient. For the case of phase encoding, N is the number of phase-encoded FIDs acquired. The implications of equations 3.11 and 3.12 are very important: if we choose too small value for FOV (by using large gradients and long times) the image will be distorted due to aliasing. On the other hand, if we choose too large value for FOV, the image resolution becomes inadequate.

Motivation for xenon gas phase NMR imaging

NMR spectroscopy and imaging are commonly used for non-invasive study of various properties in materials and biological samples (3). Their application to gases, however, has been hampered by poor signal to noise ratio, a consequence of the low-

density medium. One important application of gas imaging is the study of solid materials that are chemically sensitive to water and other liquids, or which in some other way may be altered upon exposure to moisture. Examples of such materials include food products, polymers, catalysts, and aerogels. For example, many proposed applications of aerogels require a detailed understanding of gas dynamics within the aerogel matrix. NMR imaging may provide valuable information concerning gas diffusivity and dynamics in aerogels as well as images of the uniformity and defects of the material itself.

One way to achieve a reasonable signal to noise ratio is to use fluorine-rich gases (C_2F_6) at elevated pressure with extensive signal averaging (8, 9). Alternatively, the optical pumping spin exchange techniques described in Chapter 2 provide a 10,000 to 100,000-fold increase in spin polarization over the natural thermal Boltzmann distribution. This enhancement in magnetization in gas phase xenon makes it possible to achieve a signal to noise ratio comparable to liquids (10-13). Laser-polarized noble gas imaging has been gaining widespread interest in the context of medical research and clinical applications primarily for images of the respiratory system (14-16). Elegant work from the Duke University Medical Center, for example, has shown striking images of laser-polarized ^{3}He and ^{129}Xe inside lungs with a variety of features, ranging from fully filled lungs to gas dynamics in pulmonary airways (17, 18).

The visualization technique for porous media demonstrated below is based on the unique imaging contrast that laser-polarized gases provide under conditions of steady-state continuous flow. The circulation system, initially designed to supply continuously freshly polarized gases, proved to be a source of imaging contrast that is derived from the *transport of laser-polarized gases via flow and diffusion* (19). As a consequence, not

only are traditional 3-D MRI gas phase images accessible, but direct "snapshots" of gas flow and diffusion in the porous samples can be obtained as well. Interaction of non-reactive xenon gas with the surface of a host material leads to a distortion of its large electron cloud as reflected by the wide chemical shift range of around 300 ppm (20). Lipophilic samples and materials with high surface area give rise to ^{129}Xe NMR signals that reflect local xenon surroundings. It is, therefore, possible to image xenon gas selectively in different environments based on its chemical shift position. This highly useful feature is not available with other gases.

In order to investigate the suitability of imaging xenon gas under continuous flow conditions, phantom lipophilic samples and porous materials are chosen. Macroporous matter, such as sea sponge, microporous and mesoporous materials, including zeolites (pore diameter < 10 Å) and aerogels (pore diameter < 500 Å), are used to illustrate the potential of the technique.

Experimental

The experimental continuous-flow optical pumping apparatus is described in detail in Chapter 2. All experiments are performed at a magnetic field of 4.3 T; images are obtained using 3-D Fourier imaging pulse sequence similar to the one depicted in Figure 3.1. The only difference is that "hard" 90° pulse is employed with substitution of the slice selection gradient G_z with second phase encoding gradient. Maximum magnetic field gradients of 50 G/cm is employed with phase encoding gradient time of 600 μs. 13X zeolite sample containing 8 spherical pellets is degassed for 10 hours under vacuum at 550

K. The flow rate is kept constant during the experiment, resulting in an average gas velocity of about 3 cm/sec within the cylindrical sample container of 4-mm internal diameter.

Laser-polarized ^{129}Xe Phantom Images

One of the main concerns with imaging laser-polarized gases under continuous flow is that gas spin-lattice relaxation can impose artificial contrast as gas travels through the sample area. In order to determine the optimal experimental conditions required to image materials, an image of an empty tube and a structured phantom sample was acquired. Figure 3.2 (A, B) shows the 1D and 2D image of xenon, respectively, flowing at V_{ave}= 2 cm/s through the empty cylinder (id = 4mm). The pulse sequence in Figure 3.1A is used to record both images with "hard" 90° pulse, without a slice selection gradient. There is no spin-lattice relaxation effects observed in the detection region (~ 13 mm solenoid coil). Otherwise one would observe higher signal intensity as xenon enters the cell, and decreased intensity as xenon leaves the tube. At average velocity of gas of ca 2 cm/s and higher, flow apparently replenishes fresh spins at a faster rate than spin-lattice relaxation.

Figure 3.3A shows a schematic phantom sample constructed from a glass tube (id = 7 mm) containing one sealed and eight open-ended capillaries (od = 1.3 mm), parallel to the gas flowing direction, each having a wall thickness of ca. 200 microns. These capillaries are seen as dark circles in the spin density image (Figure 3.3B). The 256×128 image in Figure 3.3 B is obtained using spin-warp pulse sequence (Figure 3.1A) with

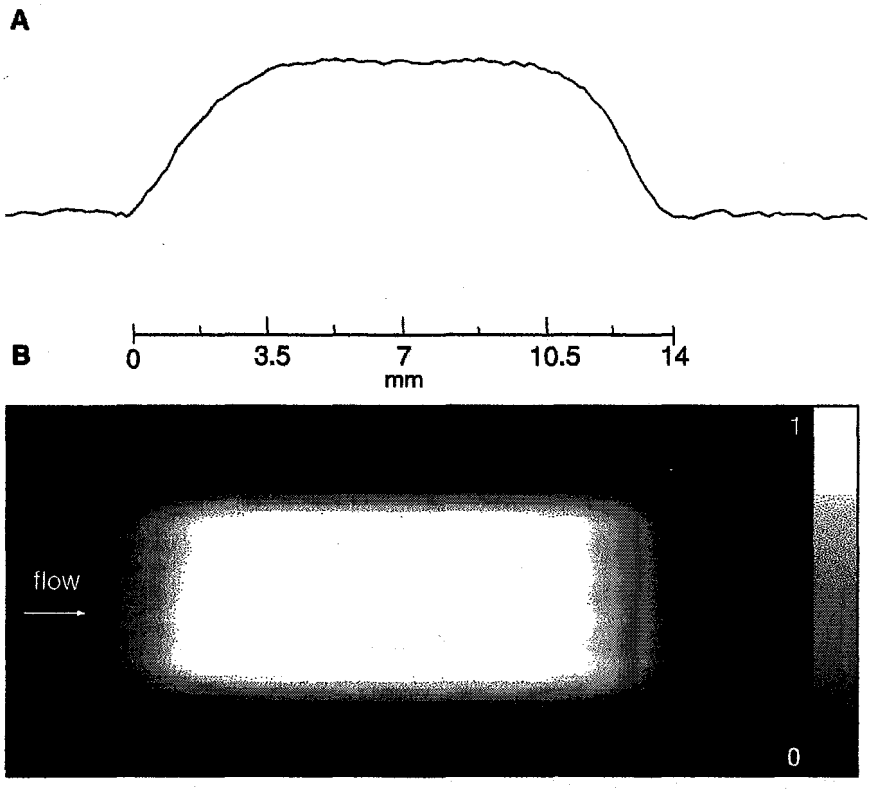

Figure 3.2 A 1D NMR image of xenon flowing through an empty cylinder. **B.** 2D NMR image of xenon in an empty cylinder. Both images exhibit no effects of spin-lattice relaxation in the direction of flow.

subsequent zero-filling the data to 512×512 data points. The capillary that was flamed-sealed on both ends (white dotted circle) remains dark as it contains no xenon.

Imaging resolution is affected and limited by molecular diffusion. Our set-up uses pressures up to 1 MPa, and the image shown in Fig. 3.3 is taken at 0.4 MPa. For gas mixtures, the diffusion coefficient, D, can be calculated using the formulae given in Ref. 24, which we calculated to be 0.1 – 0.2 cm^2/s. The maximum imaging resolution is limited to about $2\times l_g$ where l_g is given by $l_g = (D/G))^{1/3}$. This gives a maximum resolution of 120-150 micrometers for our experiment. If necessary, the parameter $2\times l_g$ can be further reduced by increasing the pressure, since D is inversely proportional to pressure. The maximum pressure, that can be used in our apparatus safely, is ca. 1 MPa (corresponding to 90-110 microns for $2\times l_g$). In addition, resolution of the images taken in flow direction will be affected by the displacement of the gas mixture during data acquisition time (~1 ms); for the present data this results in gas convection of 50 to 70 micrometers (average velocity of 5 cm/s).

The phantom images presented above demonstrate the feasibility of Fourier imaging under continuous flow of laser-polarized ^{129}Xe. This new technique is useful for imaging studies of materials and is described further in the next section.

Xenon Imaging of Natural and Synthetic Porous Systems

Xenon gas imaging of materials can be broadly divided into two categories: void space imaging and chemical shift selective imaging. Void space imaging is based on a bulk gas phase ^{129}Xe NMR signal when xenon is diffusing through a macroporous matrix, without

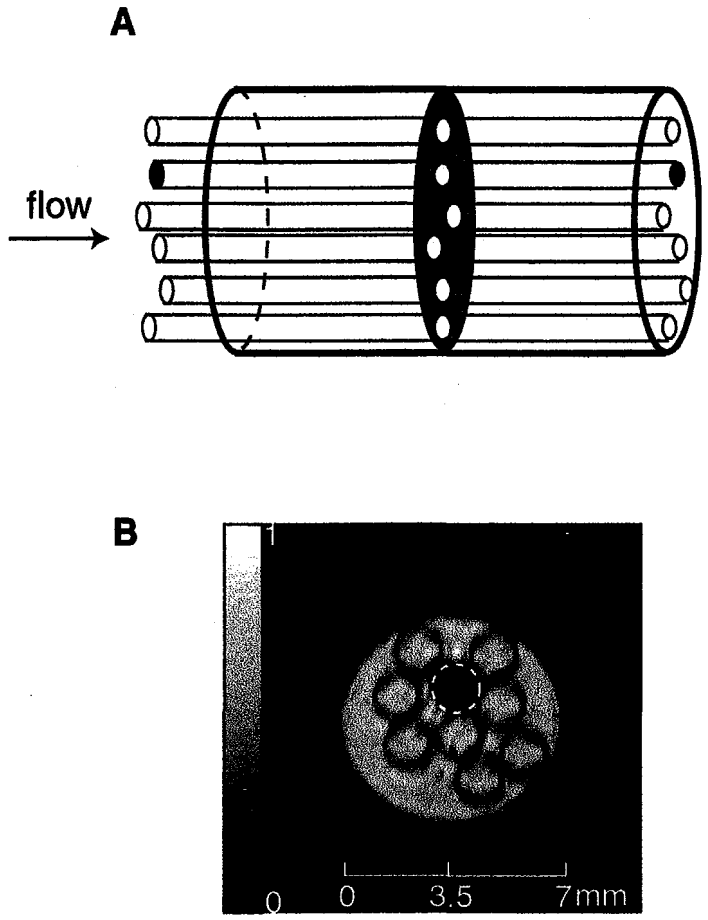

Figure 3.3 A Xenon flowing through a phantom sample tube containing several glass capillaries (slice thickness = 4 mm). **B.** 2-D Fourier image of laser-polarized ^{129}Xe (digital resolution = 110×340 μm). One capillary has sealed ends and remains dark (white dotted circle).

significant interaction of the xenon atom with the surface of the material. This type of imaging is very popular in medical imaging of respiratory systems (17, 18).

Chemical shift selective ^{129}Xe imaging (19) requires surface-xenon interaction that results in several chemical shift signals. This type of imaging has not been employed thus far; in the following section one can find the examples of chemical shift selective images that may result in useful applications. The following results show examples of ^{129}Xe void space and chemical shift imaging (CSI) of natural and synthetic porous systems (xenon dissolved in phantom lipophilic sample is presented as well). In addition, lipophilic phantom demonstrates potential benefits in studying selectively lipophilic sites in biomedical samples, since there is a second ^{129}Xe NMR signal due to dissolution in a fatty environment.

Void space ^{129}Xe imaging under continuous flow

Lacunar materials and systems such as pumice, sponge, sand and glass beads form interconnected pore spaces which permit transport of fluids through the samples. An elephant sea sponge and fragment of sea coral are used as examples of macroporous systems with random pore distribution. Since the pixel resolution is less then the average pore size, it is possible to examine the pore space framework directly from the spin density image. Figure 3.4 shows 2-D slices from 3-D ^{129}Xe imaging data set of xenon gas flowing through the elephant sea sponge. Sea sponge has a non-rigid porous framework, therefore it is necessary to pack the sample without affecting the original structure (the sharp edges of the cylindrical container were used to cut into the sponge, so that the sponge piece in

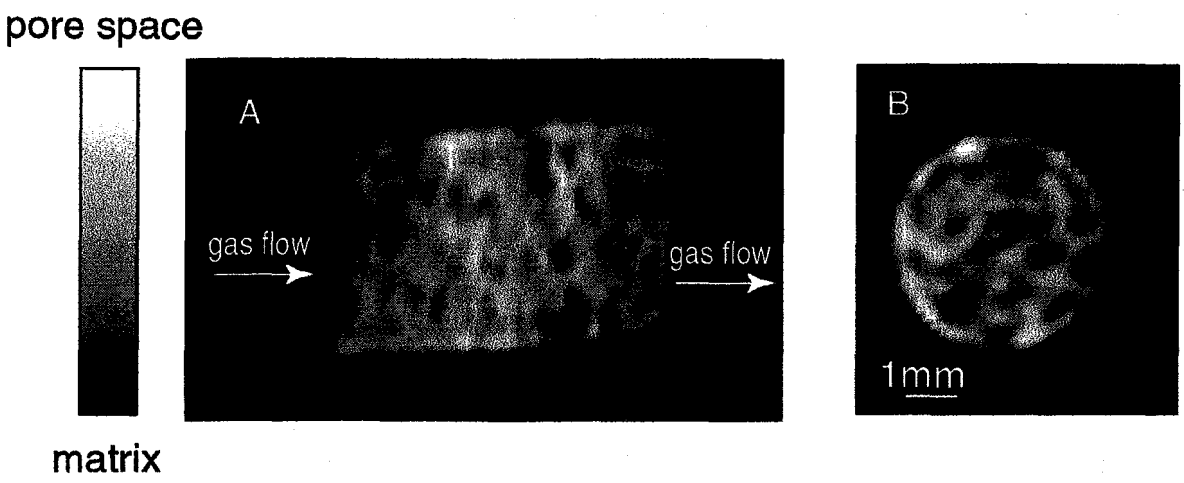

Figure 3.4. Void space image of xenon flowing through elephant sea sponge. Bright contrast corresponds to void space, whereas dark space corresponds to matrix of the sponge. The 3-D ^{129}Xe MRI data set (with resolution of 250*250*250 micrometers) was collected in the course of 3.5 hours using pulse sequence similar to the one depicted in Figure 1A (with one more phase-encoded gradient employed and no slice selection).

A. Longitudinal 2-D slice from the 3-D data set (along the flow direction).

B. 2-D slice transverse to the gas flow from the same 3-D data set.

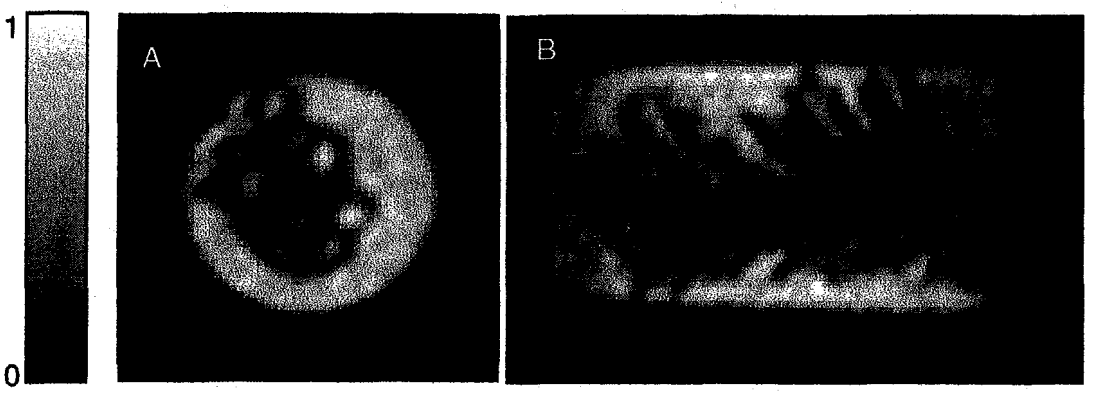

Figure 3.5 Void space image of xenon inside a small branch of sea coral. Bright contrast corresponds to void space, whereas dark space corresponds to structural matrix of coral. The 3-D ^{129}Xe MRI data set (with resolution of 350 micrometers in every direction) was collected in the course of 6 hours using pulse sequence similar to the one depicted in Figure 1A (with one more phase-encoded gradient employed and no slice selection). **A**. Longitudinal 2-D slice from the 3-D data set (along the flow direction). **B**. 2-D slice transverse to the gas flow from the same 3-D data set.

the sample did not collapse). The sponge matrix is clearly visible in both slices; it is also obvious that the ratio of pore space/sponge matrix is greater than unity.

Another example of void space imaging is shown in Figure 3.5, with xenon gasflowing through a small branch broken from sea coral. As in the case with the previous image, this is also an example of "negative" imaging in that the high intensity of the signal corresponds to the void space in the system. But unlike elephant sea sponge, this sample has a rigid matrix framework with the pore space/coral matrix ratio less than unity. Most of the signal intensity comes from xenon gas above and below the coral fragment, because the material occupies the middle of the container, with some empty space at the walls. Perhaps the magnetic susceptibility due to porous medium in the sample is diminishing the gas signal intensity to some degree as well.

To date void space imaging is being used extensively in medical imaging of respiratory airways (17, 18). In materials imaging both structural properties and transport phenomena can be examined using ^{129}Xe NMR imaging, since it has the ability to use spin-density images to mirror the full percolation cluster. Also the percolation backbone can be identified with the aid of the velocity data in the same manner as described in reference 21; this may be especially valuable in studies of water sensitive solid materials (e.g. food products, polymers, catalysts, and aerogels).

Chemical shift selective imaging

Aerogels are ultra-light porous materials, typically based on silica, with densities ranging from 0.003 to 0.25 g/cm^3 (22). The aerogel chemical composition, microstructure, and physical properties can be controlled at the nanometer scale, giving rise to unique

optical, thermal, acoustic, mechanical and electrical properties. NMR spectra of laser-polarized xenon gas flowing through fragments of silica aerogel at two different partial pressures are depicted in Fig. 3.6. Xenon occluded within the aerogel gives rise to a signal with a chemical shift separated by about 25 ppm from that of pure (bulk) gas phase. The solid line corresponds to a gas pressure of 1 atm (0.5 atm of Xe and 0.5 atm of N_2) and the dashed line corresponds to a gas pressure of 4 atm (3 atm of Xe and 1 atm of N_2). The addition of nitrogen gas facilitates optical pumping (5), although pure xenon gas can also be used with somewhat reduced signal intensity. The decrease in chemical shift with the higher pressure of gas occluded into the aerogel fragments is in agreement with previous NMR data for xenon at thermal equilibrium (23). In order to produce "chemical shift selective" images, low power gaussian-shaped rf pulses are used. Thus, images of xenon diffusing through aerogel fragments (Fig. 3.6B) can be separated from those of the bulk phase xenon gas (Fig. 3.6C). The gas diffusion around and into the material can be visualized by spin density images encoded with varying time delays between excitation pulses. NMR experiments normally involve a time delay between scans during which the longitudinal magnetization is restored to thermal equilibrium by spin-lattice relaxation. In the present methodology, which uses "externally prepared" magnetization, the rf excitation pulse essentially destroys the magnetization created by optical pumping and the system thus relaxes back to thermal equilibrium, yielding negligible imaging contrast for the gas phase. In this mode of imaging, therefore, the spin-lattice relaxation is effectively replaced by the transport of fresh laser-polarized ^{129}Xe via flow and diffusion.

Figure 3.7 demonstrates the penetration of xenon into aerogel fragments as a function of the "transport time" (the time delay between excitation pulses) and the total

gas pressure. NMR images of high-pressure gas mixture (total pressure = 4 atm), penetrating aerogel fragments via diffusion are shown in Fig. 3.7 A-C, and a lower pressure gas mixture (total pressure = 1 atm) are shown in Fig. 3.7 D-F. For short time delays between the pulses the images exhibit a xenon signal at the outer regions of the aerogel fragments (Fig. 3.7 A and D). The extent of xenon penetration into the material depends on the diffusion coefficient, and can be estimated by the mean displacement $\overline{R} = \sqrt{2Dt}$, where D is the diffusion constant and t is the time delay between excitation pulses. The diffusion coefficient of xenon inside the aerogel fragments depends on the overall gas pressure; thus it is possible to visualize different degrees of gas penetration into the material in a given time period by comparing experiments at different gas pressures. Since mean displacement, R, can be obtained directly from the spin-density images it is possible to calculate diffusion coefficient. This method, however, is not very accurate, because it is difficult to ensure uniform distribution of radio-frequency pulses throughout the entire sample. Pulsed Field Gradient (PFG) technique described in Chapter 4 yields more accurate diffusion measurements. Using PFG technique, for a lower pressure mixture (0.5 atm of Xe, 0.5 atm of N_2) we find D_{aero} = 0.65 mm^2/s, whereas the high pressure mixture (3 atm of Xe, 1 atm of N_2) yields D_{aero} = 0.35 mm^2/s. Bulk phase xenon diffusion coefficients, D_{bulk}, for low and high pressure mixtures are determined to be 5.5 mm^2/s and 2.6 mm^2/s respectively. The different degree of gas penetration (e. g. compare Fig. 3.7B and 3.7E) can be observed only for short time delays. For longer times, the material becomes saturated with polarized gas as seen in the images of Fig. 3.7C and Fig. 3.7F.

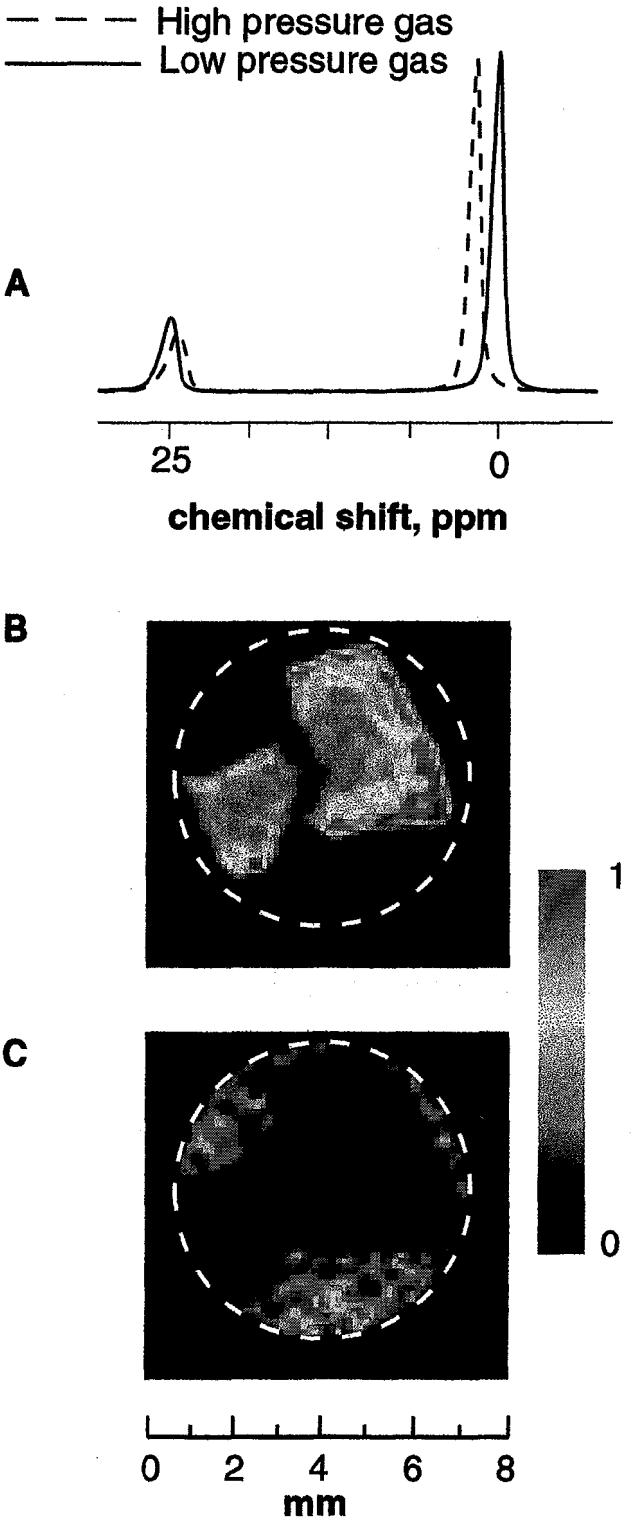

Figure 3.6 (see below)

Figure 3.6

A. NMR spectra of laser-polarized ^{129}Xe flowing through aerogel fragments at two different pressures (T = 290 K). Xenon occluded in aerogel gives rise to a signal around 25 ppm, where the pure gas phase (bulk phase) at 1 atm has been used as a reference at 0 ppm. The solid line shows the spectrum recorded at 1 atm total pressure (0.5 atm of xenon and 0.5 atm of N_2) and the dashed line shows the result at 4 atm (3 atm of xenon and 1 atm of N_2).

B. "Polarization-weighted" images of laser-polarized xenon diffusing into aerogel fragments, based on chemical shift selection of the transition at 25 ppm (spectrum Fig. 3.6A, solid line). 2D magnetic resonance image slices (perpendicular to the flow) from the full 3D data set, with a resolution of 250 × 250 ×100 micrometers, are recorded at T = 290 K using a lower pressure gas mixture with a pulse time delay of 0.4 sec. The white circle designates the wall of the sample container.

C. "Polarization-weighted" images of bulk laser-polarized xenon gas outside the aerogel fragments, based on chemical shift selection of the transition at 0 ppm (see Fig. 3.6A, solid line). The image is a 2-D slice from the full 3-D data set with a resolution of 250 × 250 ×100 micrometers, taken perpendicular to the flow with a pulse time delay of 0.4 sec.

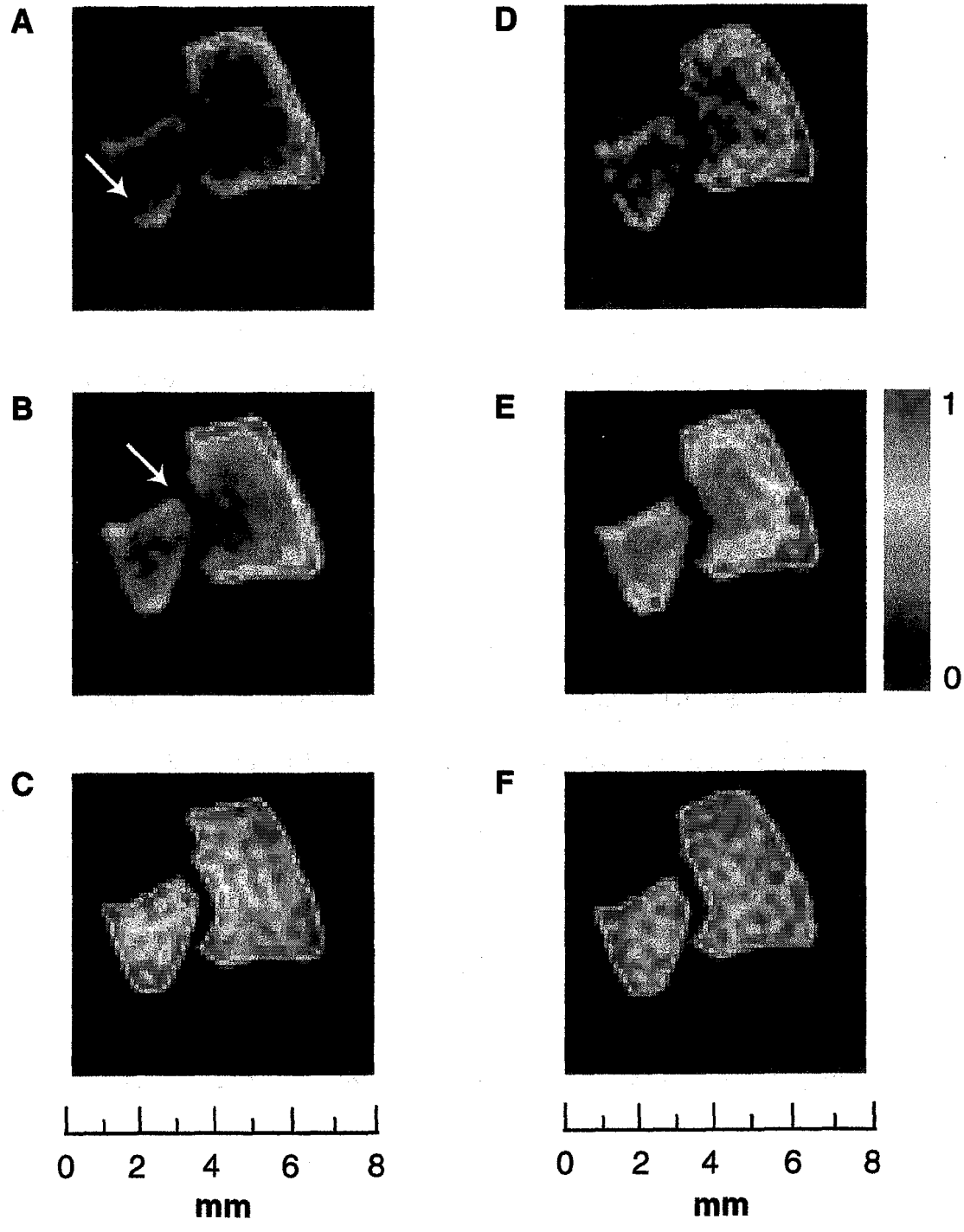

Figure 3.7 (see below)

Figure 3.7

Penetration of laser-polarized xenon into silica aerogel fragments at two different pressures as a function of time delay between excitation pulses. 2-D magnetic resonance image slices perpendicular to the flow from a 3-D data set are shown, with a slice thickness of 100 micrometers and an in-plane resolution of 250×250 micrometers.

A-C: Magnetic resonance images of xenon adsorbed in aerogel fragments at high pressure (3 atm of xenon and 1 atm of N_2; spectrum in Fig. 3.6A, dashed line around 25 ppm). The diffusion coefficient of xenon at T = 290 K under these conditions is $D_{aero} = 0.35$ mm^2/s. The pulse delay times are A) 0.2 s, B) 0.4 s, C) 2 s.

D-F: Magnetic resonance images of xenon adsorbed in aerogel fragments at lower pressure (0.5 atm of xenon and 0.5 atm of N_2; spectrum Fig. 3.6 A, solid line at 25 ppm). The diffusion coefficient of xenon at T = 290 K under these conditions is $D_{aero} = 0.65$ mm^2/s. The pulse delay times are: D) 0.2 s, E) 0.4 s, F) 2 s. The asymmetrical distribution of xenon spin density inside the aerogel fragments, for the shorter time delays, reflects the close proximity of fragments to each other and to the walls of the container, which attenuates the efficient accessibility of polarized gas to the fragments (white arrow).

An interesting feature of xenon images is the asymmetrical distribution of xenon spin density in the aerogel fragments at short time delays (indicated by the white arrows in Fig. 3.7A and 3.7B). This is, perhaps, a consequence of the differential flow and restricted accessibility of gas to the fragments. Figure 3.6 C demonstrates that for some regions the gas flow is obstructed and therefore at short time delays the delivery of freshly polarized xenon is limited (the lack of xenon spins between the fragments is obvious). Such circumstances arise, for example, for fragments close to the glass walls of the sample container and for areas of close contact between fragments.

Figure 3.8 depicts how particle contact and restricted gas flow affect images of gas penetration into zeolite particles. The technique thus presents a useful means of mapping out the dynamics of gases flowing over a bed with porous fragments, a common situation in industrial processes that utilize heterogeneous catalysts. The xenon atom has a diameter of about 4.4 Å, making it an appropriate probe of 13X zeolites with estimated pore size of about 7-8 Å (24). The NMR spectrum of laser-polarized xenon flowing through 13X zeolite particles of diameter $\cong$ 2 mm, shows two signals, one from bulk phase ^{129}Xe (reference peak), and a second one at 130 ppm arising from xenon occluded within the zeolite. A two-dimensional magnetic resonance image slice of the occluded xenon, taken from the full 3-D data set, in a plane parallel to the flow is shown in Fig. 3.8B, whereas Fig. 3. 8 C depicts a slice through one particle, perpendicular to the flow.

The most apparent feature of Fig. 3.8 B and C is the high intensity in the outer area of the particles with signal rapidly decaying towards the center. The penetration of xenon into the material is indeed dominated by diffusion, but spin-lattice relaxation

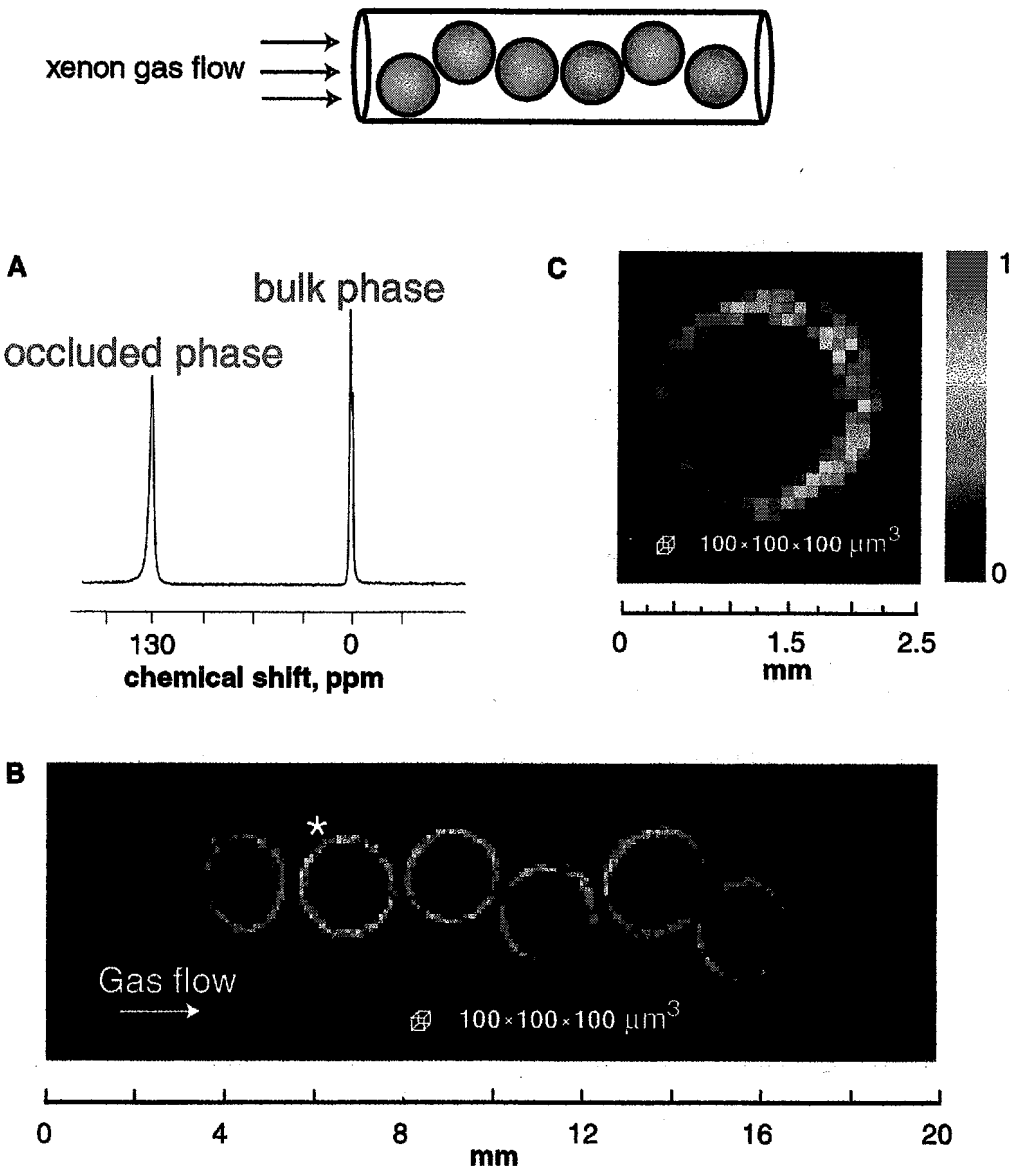

Figure 3.8 (see below)

Figure 3.8

A. NMR spectrum of laser-polarized xenon flowing through spherical particles of 13X zeolites (T = 290 K). Xenon occluded within the zeolite gives rise to a signal at 130 ppm, referenced to bulk phase xenon gas at 0 ppm (1 atm of xenon, 1 atm of N_2).

B. Magnetic resonance 2D image, longitudinal slice (along the direction of flow) from a full 3-D data set for xenon occluded in zeolite particles. The 3D data with a resolution of 100 micrometers in all 3 dimensions (64×64×256 points) are Fourier-transformed with no zero-filling or smoothing filters. Spin-lattice relaxation reduces the polarization of xenon before the pellet is saturated completely with laser-polarized ^{129}Xe. The asymmetric intensity of spin density in the pellets reflects close contact of neighboring particles, which interferes with the efficient flow and accessibility of polarized gas to the particles.

C. Magnetic resonance 2D image, transverse slice (perpendicular to the direction of flow) from a full 3-D data set as described in Fig. 3.8B. The asterisk (*) indicates which particle of Fig.3 B is depicted in the slice. The low signal intensity on the left-hand side of the particle is due to its close proximity to the glass walls of the container, which interferes with the flow accessibility of polarized gas.

reduces the signal before the particles can become saturated with polarized gas, in contrast to the situation for the aerogel fragments. Polarization-weighted xenon NMR imaging with variable time delays can be used to map out gas phase dynamics between particles with a resolution of $100 \times 100 \times 100 (\mu m)^3$, a compelling advance in gas phase imaging.

Chemical Shift Imaging of ^{129}Xe in a Lipophilic Environment

Figure 3.9A shows an NMR spectrum of ^{129}Xe flowing through a sample with vacuum grease spread on the walls of the glass cylinder. Xenon dissolved in a lipophilic environment gives rise to a signal at 200 ppm (referenced to a signal from free xenon gas in the center of the tube at 0 ppm). It is possible to use a "soft" Gaussian-shaped pulse in order to select either signal by centering the rf frequency carrier on the desired transition. Figure 3.9B shows a 2D transverse image of xenon absorbed in vacuum grease; note that it is possible to see two lines cut through the grease on the sample walls. Curiously, if the rf frequency carrier is centered between the two signals, both xenon phases – adsorbed and free, are visible (Figure 3.9C). This effect has been observed before in ^{1}H imaging (it is known as a chemical shift artifact), and it is often encountered in systems where NMR signals are very close in frequency (2-3 ppm). This artifact is not desirable in ^{1}H imaging, since very small frequency separation between the NMR transitions manifests itself as an additional "ghost" that appears as part of the image. For xenon gas this effect can be used to observe xenon simultaneously in two different environments, since the large frequency separation (from 25 to 300 ppm) allows unambiguous assignment of the images.

In summary, laser-polarized ^{129}Xe gas produced under continuous flow enhances imaging studies of porous medium. The technique described above permits 3D imaging of

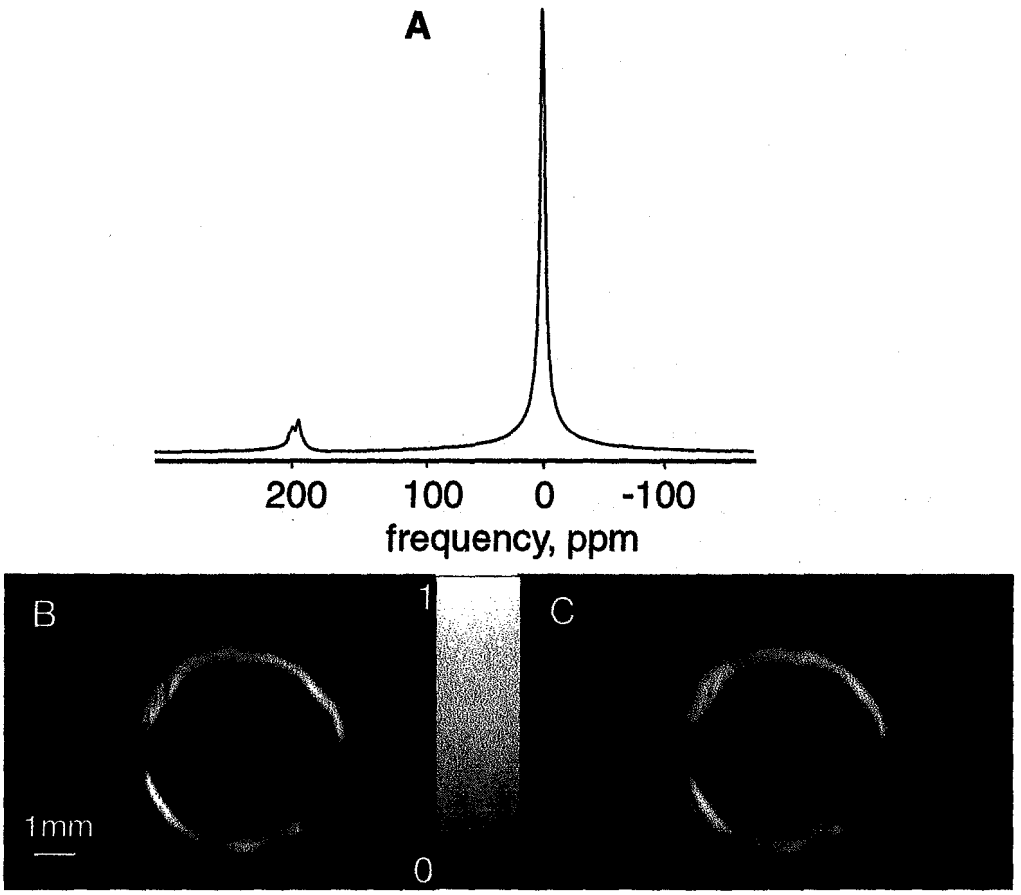

Figure 3.9 A. NMR spectrum of xenon flowing through cylindrical tube (walls covered with vacuum grease). **B.** 2-D transverse image of xenon adsorbed in lipophilic environment (rf frequency carrier is centered around 200 ppm transition). **C**. 2-D transverse image of xenon in the same sample as in B, but with rf frequency carrier centered between the two transitions (around 100 ppm).

gas spin density inside porous networks with the same sensitivity as liquid state imaging. Since the delivery of xenon into the porous material is based on the transport of laser-polarized gas via flow and diffusion, this method also has the capability of providing "snapshots" of the gas dynamics, thereby allowing the visualization and investigation of transport phenomena in porous materials. Chemical shift selective images of xenon gas in various environments can be a very powerful tool in analyzing catalytic processes where gas transport plays a key role. Using the continuous-flow apparatus, "polarization-weighted" images can also be utilized as complementary data to the quantitative NMR measurements of velocity and diffusion, a topic discussed in the next chapter.

References

1. P. C. Lauterbur, *Nature* **242**, 190 (1973)
2. P. Mansfield and P. K. Grannell, *J. Phys. C* **6**, L422 (1973)
3. P. T Callaghan, *Principles of Nuclear Magnetic Resonance Microscopy*, Oxford University Press Inc, New-York (1991)
4. Y. Xia, *Concepts of Magn. Reson.*, **8**, 205 (1996)
5. W. A. Edelstein, J. M. S. Hutchison, G. Johnson, and T. Redpath, *Phys. Med. Biol.*, **25** 751, (1980)
6. P. C. Lauterbur and C. M. Lai, *IEEE Trans. Nucl. Sci.* **27**, 1227 (1980)
7. G. H. Glover and J. M. Pauly, Encyclopedia of Nuclear Magnetic Resonance (ed. D. M. Grant and R. K. Harris), p. 3772, Wiley, New York (1996)
8. P. J. Prado, B. J. Balcom, I. V. Mastikhin, A. R.Cross, R. L. Armstrong, and A. Logan, *J. Magn. Reson.* **137**, 324 (1999).
9. M. J. Lizak, M. S. Conradi, and C. G. Fry, *J. Magn. Reson.* **95,** 548 (1991).
10. W. Happer, E. Miron, S. Schaefer, D. Schreiber, W. A. van Wijngaarden, and X. Zeng, *Phys. Review A* **29**, 3092 (1984)
11. G. Navon, Y. –Q. Song, T. Rõõm, S. Appelt, R. E. Taylor and A. Pines, *Science* **271**, 1848 (1996)
12. D. Raftery, H. Long, T. Meersmann, P. J. Grandinetti, L. Reven, and A.Pines, *Phys. Rev. Lett.* **66**, 584 (1991)

13. B. Driehuys, G. D. Cates, E. Miron, K. Sauer, D. K. Walter, and W. Happer, *Appl. Phys. Lett.* **69**, 1668 (1996)

14. M. S. Albert, G. D. Cates, B. Driehuys, W. Happer, B. Saam, C. S. jr. Springer, and A. Wishnia, *Nature* **370**, 199 (1994)

15. M. E. Wagshul, T. M. Button, H. F. Li, Z. Liang, C. S. jr. Springer, K. Zhong, and A. Wishnia, *Magn. Reson. Med.* **36**, 183 (1996)

16. B. Saam, D. A. Yablonsky, D. S. Gierada, and M. S. Conradi, *Magn. Reson. Med.* **42**, 507 (1999).

17. X. J. Chen, M. S. Chawla, L. W. Heldund, H. E. Möller, J. R. MacFall, and G. A. Johnson, *Magn. Reson. Med.* **39**, 79 (1998)

18. H. E. Möller, X. J. Chen, M. S. Chawla, G. P. Cofer, B. Driehuys, L. W. Hedlund, L. E. Suddarth, and Johnson G. A. *Magn. Reson. Med.* **41**, 800 (1999)

19. L. G. Kaiser, T. Meersmann, J. W. Logan, and A. Pines, *Proceed. of Natl. Acad. of Science* **97**, 2414 (2000)

20. P. J. Barrie and J. Klinowski, *Prog. Nucl. Magn. Reson. Spectrosc.* **24**, 91 (1992)

21. A. Klemm, H. -P. Muller, and R. Kimmich, *Physical Review* E, **55**, 4413 (1997)

22. S. Q. Zeng, A. Hunt, and R. Greif, *J. Non-Cryst. Sol.* **186**, 264 (1995)

23. D. M. Gregory, R. E. II Gerald, and R. E. Botto, *J. Magn. Reson.* **131**, 327 (1998)

24. J. Kärger and D. Ruthven, Diffusion in Zeolites and Other Microporous Solids, John Wiley & Sons, Inc., (1992)

25. R. B. Bird, W. E. Stewart, and E. N. Lightfood, Transport Phenomena, Wiley, New York (1960).

Chapter 4

Stochastic transport of xenon gas in porous media

Introduction

Effects of motion on a Nuclear Magnetic Resonance (NMR) signal have been known for a long time. In 1950 Hahn, in arguably the most famous article in NMR (1), derived the effect of molecular self-diffusion on spin echoes and in 1951 Suryan (2) reported first measurement of flow by NMR. The use of NMR study of flow and diffusion motion has several advantages such as its inherent non-invasiveness, the absence of preferred directions (in contrast to scattering experiments), the ability to distinguish between stationary and flowing spins, and to penetrate opaque media. The limitations of NMR are well-known (low sensitivity for most of the nuclei, except protons), incompatibility with ferromagnetic objects, and the fact that most NMR experiments measure average displacement over time, in contrast to some methods such as laser Doppler velocimetry, which measures instantaneous values (3).

This chapter examines gas diffusion phenomena using laser-polarized xenon in porous media for two extreme cases. In part I, the Pulsed-Field Gradient (PFG) NMR technique is applied to the study of xenon gas diffusion in aerogel. The aerogel matrix is a good representation of a random network, with pore sizes larger than the xenon atom by several orders of magnitude. In Part II, "single-file" diffusion is examined for xenon in TPP crystallites. The nanochannels of TPP are highly symmetrical cylinders with approximately the same diameter as the xenon atom.

Theory

The quantatative study of diffusion dates from the early work of two pioneers, Thomas Graham and Adolf Fick, during the period 1850-1855. On the basis of their work what is generally known as Fick's Second Law of Diffusion is formulated:

$$\frac{\partial C}{\partial t} = D\frac{\partial^2 C}{\partial z^2} \qquad 4.3$$

where C is the concentration and D is the diffusion coefficient. Later Einstein elaborated on the close relationship between Brownian motion and diffusion in his famous paper in 1905 (4). The general solution of equation 4.3 by differentiating (for a constant diffusivity system) is

$$C = \frac{A}{\sqrt{t}} e^{-z^2/4Dt} \qquad (4.4)$$

where A is an arbitrary constant. Since the total quantity of diffusing substance is related to C by

$$\mathrm{M} = \int_{-\infty}^{+\infty} \mathrm{C}dz \qquad (4.5)$$

one can substitute equation 4.4 to show that when the quantity of solute is initially confined to the plane at z=0, the distribution of solute at all later times will be given by

$$\frac{C}{M} = \frac{e^{-z^2/4Dt}}{\sqrt{4\pi Dt}} \tag{4.6}$$

Equation 4.6 thus give the probability of finding, at position z, a particle which was located at the origin at time zero. This quantity is termed the "Propagator" and, as it is a Gaussian function, it is completely defined by the mean square half-width, which can be found directly from equation 4.6 by integration

$$< z^2(t) >= \int_{-\infty}^{+\infty} z^2 \frac{e^{-z^2/4Dt}}{\sqrt{4\pi Dt}} dz = 2Dt \tag{4.7 a}$$

$$< r^2(t) >= \int_{-\infty}^{+\infty} \mathbf{r}^2 \frac{e^{-\mathbf{r}^2/4Dt}}{(4\pi Dt)^{3/2}} d\mathbf{r} = 6Dt \tag{4.7 b}$$

with the corresponding solution for isotropic diffusion in three-dimensional space (4.7 b).

Brownian motion is inherently a three-dimensional process; the situation changes, however, when the particles are confined in the channels that have similar size as the particles themselves. In such systems, the particles can no longer bypass each other and the microscopic motion can not be considered as three-dimensional. The resulting diffusion is termed "single-file" diffusion and the time dependence of the mean displacement changes to

$$\langle x^2(t) \rangle = 2F\sqrt{t} \tag{4.8}$$

where F ($[F] = m^2/\sqrt{s}$) is the mobility factor (5-8).

Diffusion in a strict sense can be studied only over distances substantially greater than the dimensions of the diffusing molecules. The PFG experiment discussed below in Part I has been shown to provide perhaps the most reliable means of measuring self-diffusivities in adsorbent-adsorbate systems since it allows measurements to be made over the micrometer distances. This method has a great advantage in that it provides direct determination of the mean square displacement in a given time interval which, in accordance with equation 4.7, can be regarded as a direct measure of self-diffusivity.

Part I.

Xenon gas diffusion through silica aerogel fragments

Pulsed-Field Gradient (PFG) NMR as a Tool for Studying Translational motion

Although there are several NMR techniques to study transport phenomena by NMR, the most widely used experiment is a PFG experiment, which was introduced by Stejskal and Tanner (9). This simple experiment involving spin echo and two gradients has the ability to simultaneously measure diffusion and average velocity. The experiment can be incorporated into more complicated pulse sequences, for example one can combine PFG with spin density imaging (see discussion on gas phase Poiseuille flow in Chapter 5). The basic PFG experiment is shown schematically in Fig. 4.1A. Displacements of the spins during the period, □between the gradient pulses result in a modification of the observed echo signal. The echo observed at time 2□ is given by

$$E(q)=\exp[\, i2\pi\Delta V_{ave}\,\mathbf{q} - 4\pi^2 D\,(\Delta - \delta/3\,)\mathbf{q}^2] \qquad (4.9)$$

where $\mathbf{q} = (2p)^{-1}\gamma\mathbf{g}\delta$ (10). The gradients, **g**, of duration δ are incremented in this experiment; V_{ave} is average velocity of the particles and D their diffusion coefficient. The full width at half maximum:

$$a = 4\,[\ln 2\,(\,\Delta - \delta/3\,)\,D\,]^{1/2} \qquad (4.10)$$

of the Fourier transformed signal is determined by the diffusion coefficient, D. Thus PFG experiment yields average velocity, V_{ave}, and effective diffusion coefficient, D. An alternative way to describe the effect of motion on PFG NMR signal is to state that echo intensity is attenuated by diffusion - the larger the diffusion is, the larger is the attenuation of the signal, and that the net phase shift of the echo is caused by net flow (coherent motion).

The measurement of self-diffusion by PFG is limited by the loss of the phase coherence due to transverse relaxation. Figure 4.1 B shows a stimulated version of the PFG experiment, which avoids this problem by storing magnetization along the longitudinal axis by means of a second 90° pulse. The observed echo attenuation in this experiment is equivalent to expression 4.9, the only penalty being the loss by a factor of 2 of signal intensity due to the projection of only half the transverse magnetization along the z-axis during the storage period. The time-scale of the PFG experiment is limited by spin-lattice relaxation time of the species, and is normally between 1 ms and 1 s. Under continuous steady state flow conditions the limitation comes from the motion of the spins, since the spins encoded by the first gradient pulse should not be washed-out by flow or diffusion from the detection area during $t = \Delta$.

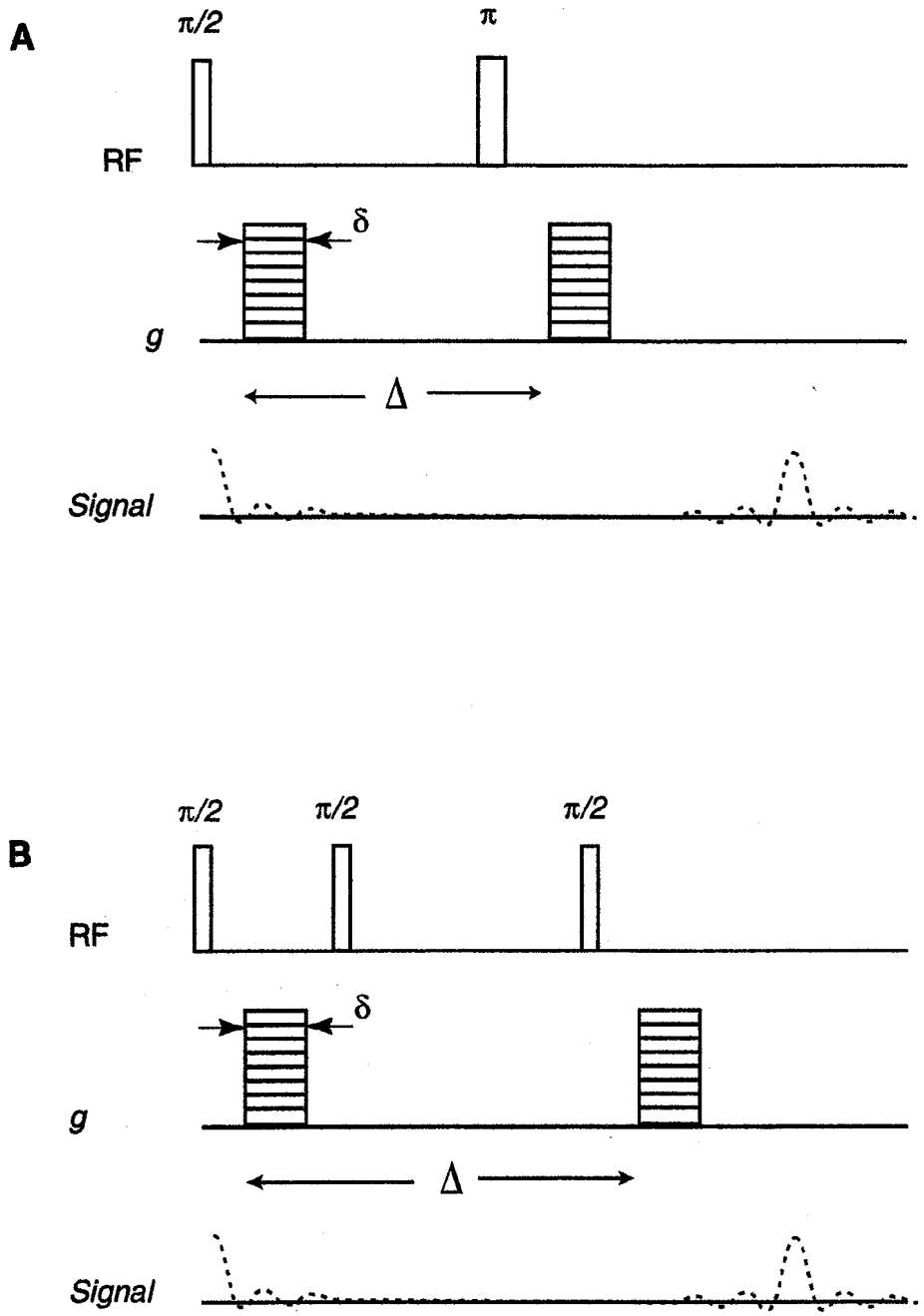

Figure 4.1 A. Pulsed gradient spin echo (PGSE) sequence with gradient amplitude, g, gradient pulse duration, δ, and gradient pulse spacing, Δ. **B** Stimulated echo version of PGSE sequence

Experimental

The experimental continuous-flow optical pumping apparatus is described in detail in Chapter 2. The experiments are performed using a 180 MHz Chemagnetics Infinity spectrometer, operating at 49 MHz for ^{129}Xe. A home-built probe, containing commercial (Nalorac) imaging gradient set (maximum gradient 0.7 T/m), is used for all the experiments. Pure xenon gas at room temperature for various pressures is used in all the measurements.

Results and Discussion

Aerogels are ultra-light porous materials, typically based on silica, with densities ranging from 0.003 to 0.25 g/cm^3 (11). ^{129}Xe PFG NMR is very well suited for investigation of water sensitive porous materials such as aerogel, since xenon is an inert gas and has a very large chemical shift range, which allows monitoring free and adsorbed phases simultaneously. Base-catalyzed tetraethoxysilane (TEOS) aerogel used in this study has a mean pore size of about 200 Å. Such a small pore size greatly restricts the motion of gas molecules in the aerogel. The mean free path of xenon gas molecules in free space is described by the equation

$$L_m = \frac{k_B T}{\sqrt{2} p d_{Xe}^2 P} \qquad (4.11)$$

where d_{Xe} is the diameter of a xenon atom (~ 4. 2 Å) and P is the pressure of the gas (11). The mean free path of xenon at 1 atm and at T = 290 is ca 500 Å. If the mean pore size of the aerogel is defined as S_m, than in the regime of $L_m/S_m<1$, the displacement of the

xenon in aerogel matrix should obey the same dependence on pressure as bulk xenon in Equation 4.11. For $L_m/S_m > 1$, the solid aerogel matrix restricts the motion of the gas, leading to a decrease in effective diffusion coefficient.

2-D PFG NMR ^{129}Xe spectra of xenon gas absorbed in several silica aerogel fragments at T=290 K are shown in Figure 4.2A. Xenon occluded in aerogel gives rise to a signal around 25 ppm, the pure gas phase at 1 atm has been used as a reference at 0 ppm. The second dimension shows evolution of the NMR signal under increasing field gradient amplitude. The data are analyzed using a Levenberg-Marquardt (L-M) algorithm (12). Figure 4.2B shows the resulting exponential signal decay for two phases of xenon. It is important that the experimental data are fit directly to the equation 4.9, rather than fitting the logarithm of the data to a straight line, since the sample points are not distributed equally in the logarithmic sampling.

Figure 4.3 shows the bulk phase and adsorbed phase xenon diffusion coefficient as a function of pressure (0.5 – 8 atm). At lower pressures, the mean free path, L_m is large, resulting in a significant difference between adsorbed and free gas stochastic displacement. For higher pressures, the displacement in aerogel approaches the free gas diffusion. However it does not completely match the value for the free gas diffusion even at 8 atm. This is consistent with the work of Zeng et al (11) in the same type of aerogel, where they determined that both free and adsorbed xenon stochastic displacement is the same for P > 10 atm (using hot wire technique).

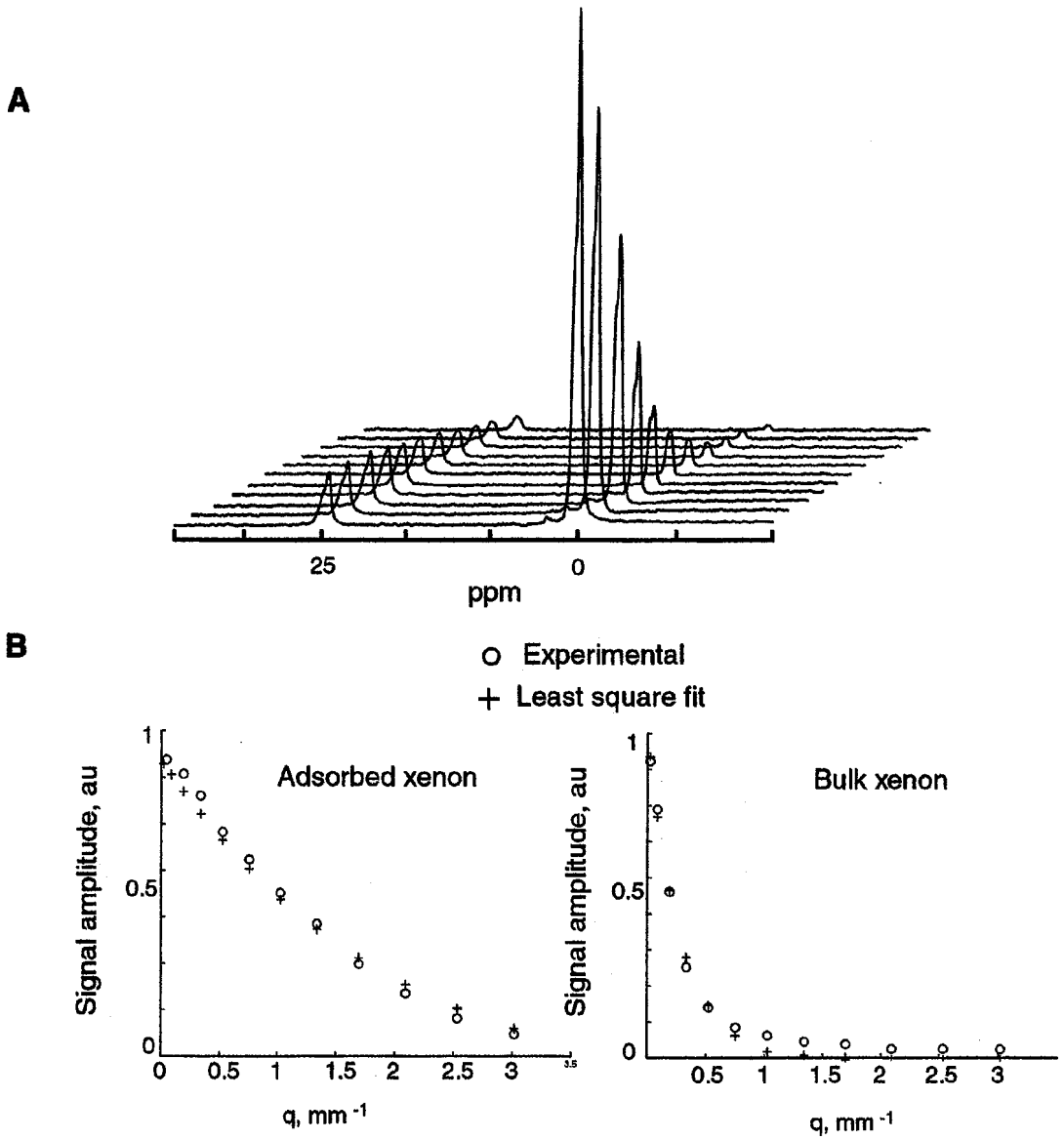

Figure 4.2 A. ^{129}Xe PGSE NMR spectra of xenon gas in aerogel fragments. Adsorbed xenon gives rise to a signal at 25 ppm relative to bulk phase xenon at 0 ppm. The spectra are acquired at T = 290 K with 1.5 atm of xenon (Δ = 50 ms, δ=1.5 ms, g ranges from 0 to 16×0.01×7 kHz/mm). **B.** Least squares fit of the signal decay due to diffusion, which yields D_{bulk}=3.5 mm^2/s, D_{aero}= 0.5 mm^2/s for free and adsorbed gas.

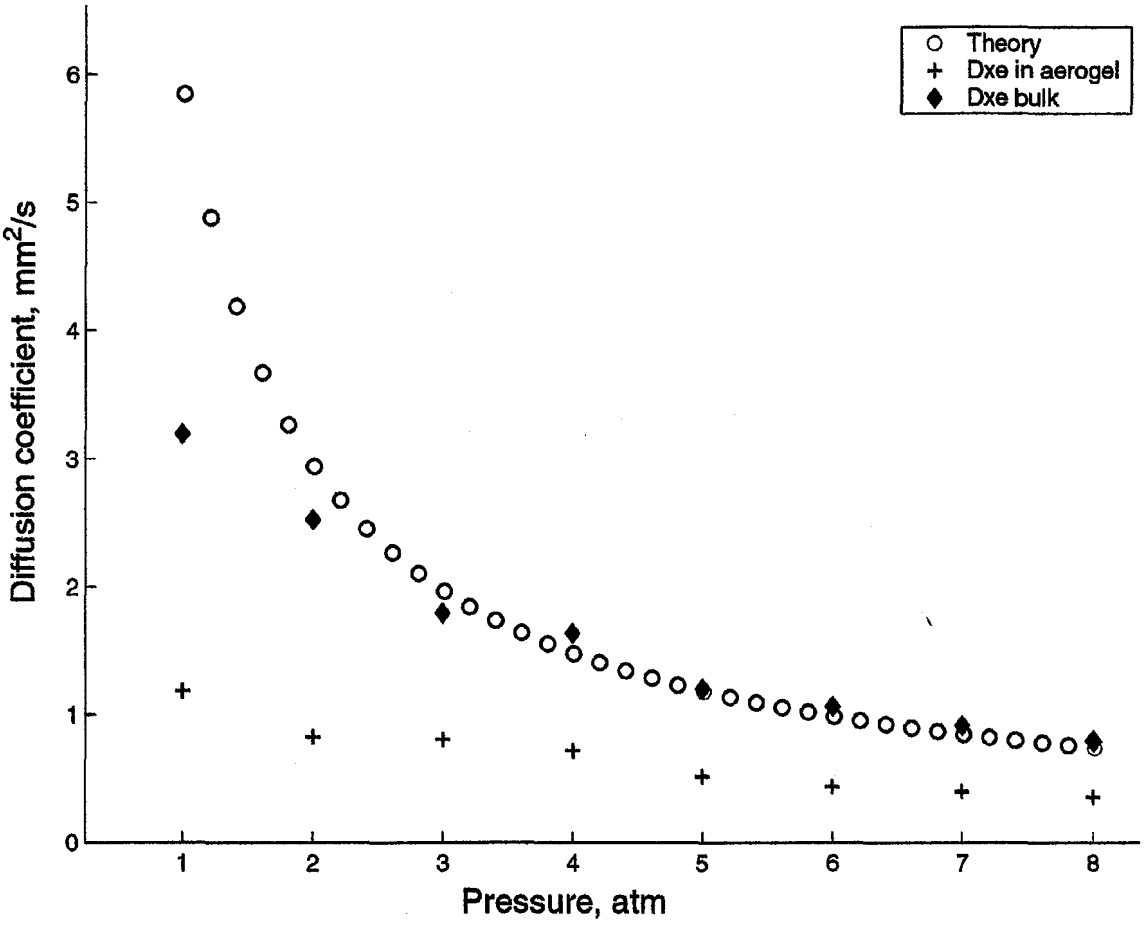

Figure 4.3 Diffusion coefficient of xenon gas as a function of pressure. At higher pressure, xenon gas adsorbed in aerogel approaches stochastic displacement of free gas. At lower pressure, free gas diffusion is significantly smaller than kinetic theory prediction due to restricted displacement between the fragments.

An interesting aspect of Fig.4.3 is the behavior of the experimental free gas diffusion coefficient (marked as triangles) with respect to the data derived from kinetic theory (marked as circles). At lower pressures the observed diffusion coefficient has a smaller value compared to kinetic theory calculation, indicating restricted diffusion due to spacing between aerogel fragments. A quick estimation of the free gas displacement during motion encoding time, $\Delta = 20$ ms, yields mean displacement of ca 250 micrometers for xenon at 4 atm (Eq. 4.7). Since the aerogel fragments are not uniform in size, it is difficult to estimate the distance resulting from random packing of such fragile porous medium as aerogels. From the data in Fig. 4.3, it is possible to estimate the average fragment separation of ca. 250 micrometers or more.

The situation described above is similar to industrial heterogeneous catalytic process, where the material might not be uniform in size and distribution. ^{129}Xe PFG NMR is capable of providing a quick estimate of the average pore size on the microscopic scale and the macroscopic dimension simultaneously.

Part II.

Single-File Diffusion in One-Dimensional Nanochannels

When the porous medium has channels with dimensions of the same size as the atoms or molecules inside the channel, the diffusion phenomena differs from Fickian behavior described by Eq. (4.7). The stochastic displacement in this type of system is

termed single file diffusion and is described by Eq. (4.8). Single-file diffusion is a rather common phenomenon in one-dimensional channel systems and has been subject to theoretical studies in the past (13-15). A few experimental verifications of single-file diffusion have been provided to date using pulse field gradient (PFG) NMR spectroscopy (16-18) at time scales of milliseconds to hundreds of milliseconds, and by quasi-elastic neutron scattering (19) with time scales in the microsecond regime. The long time behavior of gas diffusion over periods relevant, for instance, in catalytic processes has been experimentally inaccessible thus far. In the second part a persistence of single-file diffusion behavior over tens of seconds for the one-dimensional gas phase in ca. 500 pm diameter nanochannels of tris(*o*-phenylenedioxi)cyclophosphazene (TPP) is described. The technique applied for the study of this system utilizes continuous flow laser-polarized ^{129}Xe NMR spectroscopy and differs drastically from conventional diffusion measurements.

Experimental

The ^{129}Xe spectra are obtained using a 500 MHz Chemagnetics infinity spectrometer, operating at 138.33 MHz for ^{129}Xe. A flow of nitrogen gas to the dewared sample region is used to cool or heat the sample. The temperatures is kept between 473 K and 163 K, at each temperature the system is allowed to equilibrate for at least 10 minutes.

The basic TPP building block is depicted in Figure 4.4A and the channel structure becomes apparent from Figure 4.4B. The synthesis of TPP/benzene inclusion compound was performed as previously reported by Allcock (20) and the pseudohexagonal

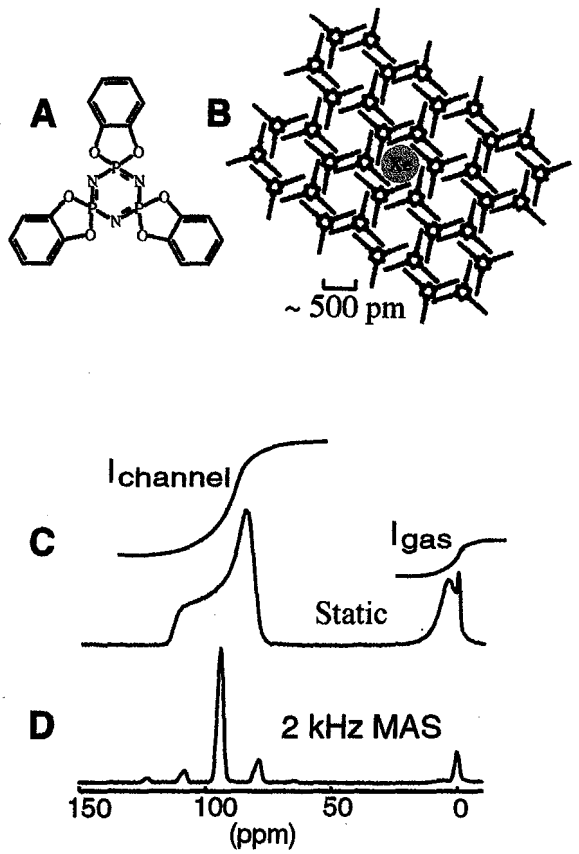

Figure 4.4 A. Basic building block of TPP crystallites. **B**. The nanochannels are composed of stacked prisms with a triangular base, where the benzene rings of TPP are the vertical faces. Neighboring prisms are rotated by 60° along the vertical axis resulting in hexagonal channels that can be considered with good approximation as cylinders of 500 pm diameter. **C**. ^{129}Xe NMR spectrum for xenon in contact with TPP at 273 K and a buildup time of 10 s. The signal from xenon inside the nanochannel is shifted at around 90 ppm with reference to the gas phase peak at 0 ppm. The broad peak overlapping with the gas phase transition is most likely from xenon in the vicinity and in between the crystallites where it is in close contact with the outer surface of the TPP. **D.** 2 kHz MAS spectrum taken under conditions otherwise identical to C.

modification of TPP with the empty channel structure was obtained by evacuation (10^{-2} torr) at 343 K (21). The fitting of the CSA patterns is performed using the following variables δ_{iso}, $\Delta\delta$, η, and the line width, using $|\delta_{33}-\delta_{iso}|>|\delta_{11}-\delta_{iso}|>|\delta_{22}-\delta_{iso}|$, $\delta_{iso} = (\delta_{11}+\delta_{22}+\delta_{33})/3$, $\Delta\delta= \delta_{33}-\delta_{iso}$ and $\eta = (\delta_{22}-\delta_{11})/(\delta_{33}-\delta_{iso})$.

Sample spinning at 5 kHz for about 30 min has been used to prepare a thin layer (a few hundred microns) of TPP crystallites on the spinner wall, thus reducing the influence of gas diffusion through the crystallite powder. All experiments for the study of single-file diffusion were performed under static (i.e. non-spinning) conditions. Figure 4.4C shows an actual static spectrum of xenon with a gas phase signal at 0 ppm and a signal with strong chemical shift anisotropy at about 100 ppm arising from xenon inside the nanochannels. Figure 4.4 D displays the 2 kHz MAS spectrum recorded under otherwise identical conditions. This spectrum confirms that the lineshape is indeed due the anisotropy of the chemical shift and not due to multiple transitions caused by different sites.

Discussion

The methodology described in Chapter 3 for the imaging of flow and diffusion into porous materials can be applied in order to distinguish between ordinary diffusion and single-file diffusion. The method is analogous to previous measurements of the diffusion of light water into a gel made with heavy water (22) and is based on the time dependence of the ^{129}Xe signal inside the channels which reflects the total gas transport into the porous material. The technique follows quite naturally from the experimental

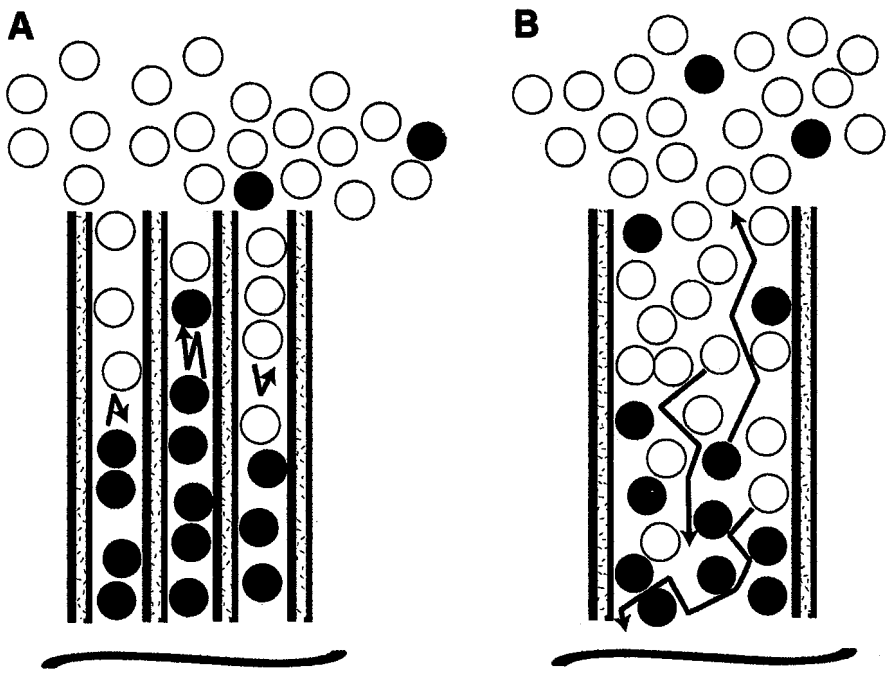

Figure 4.5 Sketches of gas particles diffusing in channels. **A.** The channel is only slightly larger than the gas particles leading to single-file diffusion and causing a time dependence in the signal intensities described by Eq 4.13. **B**. The channel with a diameter larger than the diameter of the gas particles will most likely lead to unidirectional (i.e. ordinary) diffusion with the time dependence described by eq 4.12.

setup of continuous flow laser polarized ^{129}Xe NMR and can therefore easily be implemented. Figure 4.5 provides a sketch of the basic idea. In Figure 4.5A, polarized xenon diffuses into nanochannels with a diameter only slightly larger than the xenon diameter of 440 pm. In contrast, Figure 4.5B depicts a hypothetical channel with transverse dimension much larger than the xenon diameter. The saturation train will destroy the laser enhanced xenon polarization, and the detected signal is solely due to laser-polarized xenon subsequently entering the detection cell and diffusing into the channels. The signal intensity is a direct function of the mean free pathway of the xenon into the channels with a temporal dependence described by either Eq. 4.7 or Eq. 4.8, depending on the channel diameter.

The actual measurement of xenon gas transport into the nanochannels starts with a train of 90° saturation pulses that destroys all xenon polarization within the detection cell. Since the experiments are performed under continuous flow conditions, the non-polarized xenon is immediately replaced by laser-polarized xenon. The gas phase is completely exchanged with laser-polarized xenon after approximately 50–200 ms (depending on the flow rate). This step can be verified experimentally by monitoring the signal intensity from the gas phase xenon. The saturation train is followed by a buildup time delay τ and signal acquisition after the final excitation pulse. The amount of laser-polarized xenon inside the channels will increase with increasing time τ until all channels are filled or a steady state due to longitudinal relaxation inside the material has been reached.

The measurement of the xenon uptake inside the nanochannels is meaningful only after the gas phase in the entire sample region has been replaced by polarized xenon via

flow and diffusion through the thin layer of TPP powder. During the initial 'dead-time' of ca. 50–200 ms, the polarized xenon is not in contact with all of the crystallites and some error will arise from the uncertainties during the initial 50–200 ms. Selective irradiation of the xenon-nanochannel transition during the initial 200 ms after the saturation train could prevent this error but has not produced substantially different results from pulse sequences without selective saturation.

Results

Although continuous flow optical pumping ^{129}Xe NMR provides the means to distinguish between unidirectional and single-file diffusion, longitudinal relaxation will dampen the signal intensity for long buildup times and has to be taken into account. Using equation 4.7 (a) and 4.8 we can derive for unidirectional (i.e. ordinary) diffusion the following relation:

$$I_{channel}(\tau)/I_{gas} = C^{D}(T,P)\int_{0}^{\tau}\frac{1}{\sqrt{t}}\times\exp(-t/T_1)dt \qquad (4.12)$$

or for single –file diffusion:

$$I_{channel}(\tau)/I_{gas} = C^{F}(T,P)\int_{0}^{\tau}\frac{1}{\sqrt[4]{t}}\times\exp(-t/T_1)dt \qquad (4.13)$$

where the temperature and gas pressure dependent prefactors C^{D} and C^{F} contain the information about xenon loading of the channels, the total number of channels, the xenon gas density and overall gas volume inside the detection cell. In Figures 4.6A and 4.6B, $I_{channel}/I_{gas}$ is the intensity of the xenon signal from the nanochannels normalized by the intensity of the gas phase signal. The normalization takes long-term fluctuations of the

optical pumping process into account. The dashed lines in Figures 4.6A and 4.6B show the behavior that is expected for unidirectional diffusion. Neither for long relaxation times (i.e. T_1 = 70 s, line i.) nor for short relaxation times (i.e. T_1 = 4 s, line ii) does Eq. 4.12 reflect the experimental buildup curves. The experiments were recorded using a 2.5% xenon in helium mixture at 243 K, 263 K and 308 K. The solid lines are the result of Eq. 4.13 and can provide a close fit of the experimental data points. The relaxation time used for the fits at all temperatures is T_1 = 70 s. Note that the T_1 values cannot be measured directly by inversion recovery in continuous flow optical pumping experiments. The ratio of the prefactor constants for the different temperatures can be obtained by fitting the experimental data with Eq. 4.13 yielding $C^F(243\text{ K}):C^F(263\text{ K}):C^F(308\text{ K}) = 1.9:2.7:1$. The temperature dependence of this constant may reflect changes in the mobility factor F $\left([F]= m^2/\sqrt{s}\right)$ as well as changes in the xenon loading of the channels.

These data provide the first experimental observation that gas transport in nanochannels exhibits single-file diffusion behavior over pronounced periods of time. The measurement of single-file diffusion over very long time periods is possible only because the nanochannels can be assumed to be of infinite length compared to the mean displacement of the xenon atoms during the time scales observed. The uptake curve reach maximum intensity plateaus after approximately 180 s which is most likely caused by relaxation rather than by complete filling of the channels with polarized xenon.

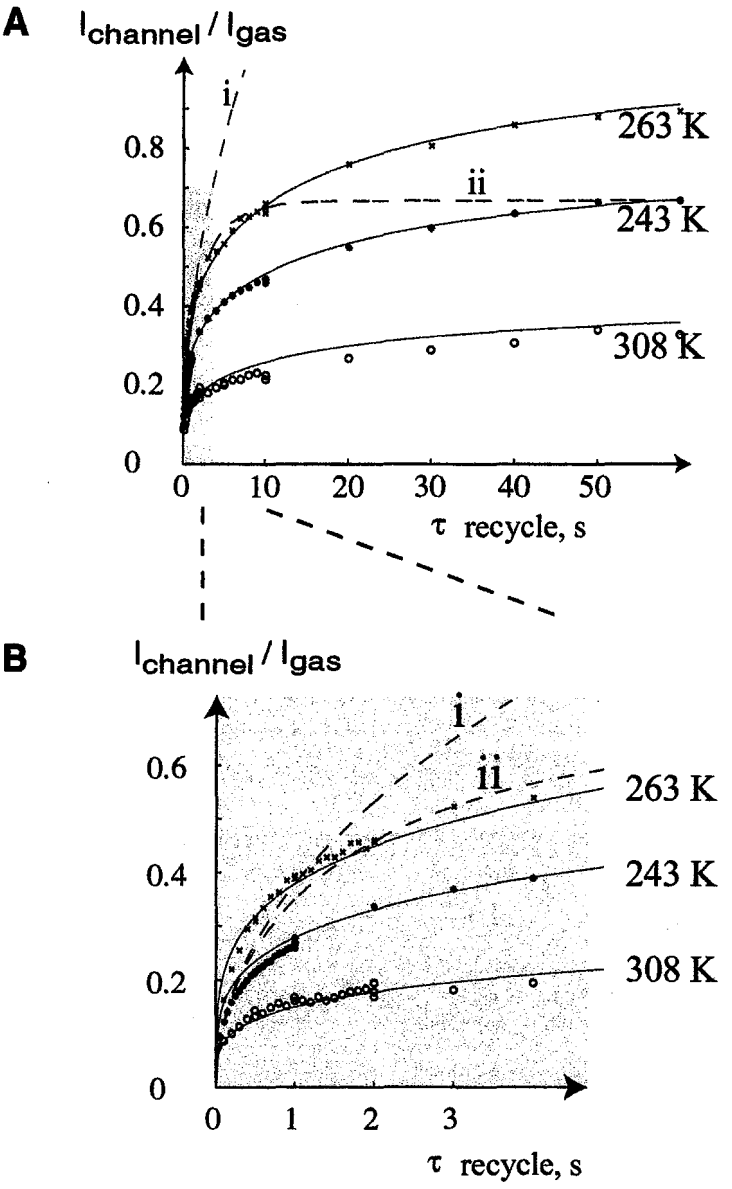

Figure 4.6 A. Integral of the xenon signal vs time for three different temperatures (308 K, circles; 243 K, stars; 263 K, crosses). The dashed lines, i and ii, envision the behavior expected from unidirectional diffusion described by eq 4.12, with $T_1 = 70$ s for line i and $T_1 = 4$ s for line ii. The solid lines represent Eq 4.13. **B** Expanded view of (A).

Correlation of the xenon transport into the nanochannels with the xenon line shape

The buildup curves at three different temperatures reveal an interesting behavior of the constant $C^F(T)$, which exhibits its largest value at the intermediate temperature of 243 K. Instead of mapping $C^F(T)$, which would require very long experimental times and high xenon usage for the open flow system, the signal intensity can be compared for various temperatures at one particular time of the xenon uptake. Figure 4.7A displays the intensities of the xenon signal inside the nanochannels after a $\tau = 10$ s buildup as a function of temperature for three different xenon concentrations. The signal intensity increases as the temperature is lowered and goes through a maximum at a temperature value that depends on the xenon concentration. Further reduction in temperature leads to decreasing signal intensity. Note that a temperature dependent change in the channel

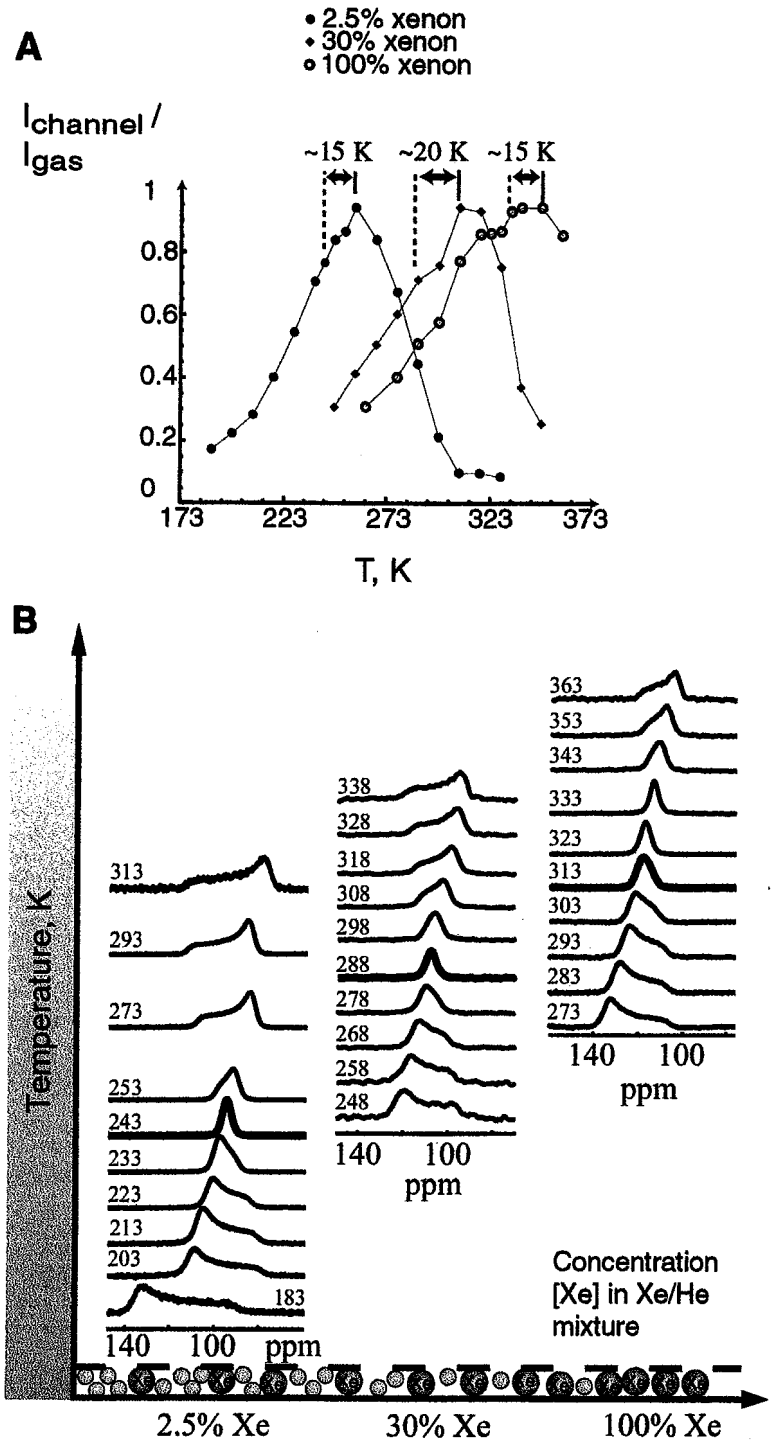

Figure 4.7 (See below)

Figure 4.7 A Experimental signal intensities (integrated) in continuous flow optical pumping ^{129}Xe NMR for xenon inside the TPP channels as a function of temperature for three different concentrations (i.e. 2.5% filled circles, 30% filled diamonds and 100% open circles). The buildup time was 10 s. Lines mark maximum intensity (solid line) and isotropic transition (dashed line, heavy line in (B)). **B**. Continuous flow optical pumping ^{129}Xe NMR line shapes for xenon inside TPP channels at various temperatures and three different concentrations: 2.5% xenon in helium, 30% xenon in helium and 100% xenon, all at atmospheric pressure (100 kPa). The xenon helium mixture is kept at a constant pressure of 100 kPa for all experiments. The fitting of the line shape resulted in the following CSA tensor values ($\eta = 0$).

Xe conc. / Temperature [K]	δ_{iso} [ppm]	$\Delta\delta$ [ppm]
2.5% / 293	92.3	16.6
2.5% / 243	95.3	2.3
2.5% / 203	102.3	–21.0
30% / 288	106.4	2.5
100% / 333	114.0	3.2

Instead of an alteration in the xenon concentration (i.e. the partial pressure of the xenon), variations in the overall pressure of pure xenon gas lead again to similar changes in the line shape (not depicted).

geometry does not provide an explanation for this behavior since it can not account for the observed temperature shift of the curves for different xenon concentrations.

A temperature and gas concentration dependence can also be seen in the xenon chemical shift anisotropy (CSA) (see Figure 4.4C, Figure 4.4D, and Figure 4.7B). An anisotropic line shape cannot be usually observed for xenon in systems with three-dimensional porous networks. All observations of xenon CSA in porous materials so far were restricted to systems containing one-dimensional channels with transverse dimensions similar to the xenon radius (23-25). However, the one-dimensional channels used in their experiments (e.g. aluminum phosphate molecular sieves) do not posses cylindrical symmetry like the TPP nanochannels, for which the xenon CSA pattern shows a nearly perfect axial symmetry (26). Figure 4.7B shows that the axially symmetric ^{129}Xe CSA at 293 K collapses to an isotropic peak as the concentration of the gas is increased from 2.5% to 30% xenon and the anisotropy reoccurs with inverted sign for pure xenon at the same temperature (the overall pressure was kept at about 100 kPa for all experiments shown in Figure 5). In addition, Figure 4.7B also demonstrates the temperature dependence of the xenon CSA. The positive anisotropy at 293 K and 2.5% xenon is reduced with decreasing temperature and at about 243 K the transition becomes isotropic. Further decrease in temperature leads to a line shape with negative anisotropy. The line shapes show comparable temperature dependence for all gas mixtures except for a shift to higher overall temperature values with increasing concentration.

Xenon atoms that are mainly affected by van der Waals interactions with the π–electrons of the channel walls can explain the observed xenon line shape at low xenon concentrations and high temperatures. This will lead to a CSA with positive and axially

symmetric anisotropy. As concentration or pressure is increased, or alternatively, the temperature is lowered, the xenon loading inside the channels rises and the xenon–xenon distance r_{Xe-Xe} decreases. This may cause a dramatic increase in the xenon–xenon interactions due to the $1/r_{Xe-Xe}^{6}$ dependence of the van der Waals forces. At the onset of the xenon–xenon interactions at low loadings, the positive anisotropy will first be reduced and subsequently be collapsed to an isotropic line shape before the xenon–xenon interactions will become dominant over xenon–wall interactions at very high loadings resulting in an axially symmetric CSA with negative anisotropy.

Comparison of Figure 4.7A with Figure 4.7B reveals that there is an intriguing correlation between the temperature dependence of the signal intensity and the temperature dependence of the line shape. An isotropic ^{129}Xe line shape (Figure 4.7B, heavy lines and Figure 4.7A, dashed lines) in the nanochannels is observable at about 15–20 K below the temperature that leads to the maximum observable xenon/TPP-channel signal (Figure 4.7A, solid lines). This correlation can be seen consistently at all xenon concentrations despite the overall temperature shift of 90 K for the various xenon–helium mixtures.

In order to explain this correlation, one has to consider that the heterogeneous xenon-nanochannel system in the NMR detection cell is in a thermodynamic equilibrium state (except for the spin polarization) and channel loading will increase with decreasing temperature or with increasing xenon gas concentration. The transport of the laser-polarized xenon into the channels depends on the diffusion within the nanochannels and

is therefore kinetically controlled. However, single-file diffusion depends strongly on the channel loading:

$$F = \sqrt{\frac{D_0}{\pi}}\sigma\frac{(1-\theta)}{\theta}, \tag{5}$$

where D_0 is the (theoretical and temperature dependent) diffusion constant of a single xenon atom in the channel, σ is the radius of the xenon atom, and θ is the loading of the channel in this 'hard sphere' approximation. The mobility factor F should therefore decrease with decreasing temperature partially due to the increased loading of the TPP nanochannels and partially due to the smaller diffusion constant D_0. Despite the reduced diffusion, the signal may still gain in intensity by lowering the temperature because of the increased xenon loading and therefore higher number of spins inside the channels. As the temperature is further reduced, the loading will approach a high filling factor with limited possibilities for additional loading increase. The reduced diffusion lowers the signal intensity as the temperature continues to decrease. The turning point in the temperature dependence of the xenon signal intensity will be accompanied by substantial xenon–xenon interactions inside the channel and will therefore be reflected in the observed xenon line shape. For TPP, the maximum intensity is reached at about 15 K before the isotropic line shape is observed independent of the used xenon concentration. Higher xenon gas phase concentration will lead to larger xenon loading for a given temperature and the temperature-intensity curves are therefore shifted to higher temperatures. In addition to the thermodynamics and kinetics inside the nanochannels, the xenon signal intensities may also be influenced by the rate of exchange from the pure gas phase into the channels (i.e. at the channel openings). However, the correlation between the temperature dependencies of the ^{129}Xe signal intensity with its line shape seems to

exclude this possibility since the line shape is generated only inside a channel. This evidence provides a strong indication that exchange processes do not determine the rate of the signal uptake, at least for the time scales used in our experiments (many hundreds of milliseconds and beyond).

Continuous flow optical pumping ^{129}Xe NMR spectroscopy provides a unique tool to distinguish between one-dimensional and single-file diffusion, in particular concerning the behavior on long time scales on the order of seconds or many tens of seconds. It can also be used when the diffusion process is too slow to be investigated by conventional PFG NMR. Although the diffusion constant itself cannot be measured directly without very strong gradients, other aspects of gas transport into nanochannels can be investigated with this technique. Complementary isotherm measurements of the xenon-channel loading at all temperatures and xenon gas concentrations would provide access to the temperature and loading dependence of the mobility factor F. Combined with the correlation between line shape and signal buildup, the technique provides new insights into the nature of gas transport into porous materials. This method will be of interest for heterogeneous catalysis in particular with respect to shape selective catalysis in restricted geometry, analytical separation methods and purification processes. It can contribute to a more basic understanding of the mechanisms that rule gas transport into porous catalysts, molecular sieves, porous rocks or pore-forming trans-membrane proteins in biological systems.

References

1. E. L. Hahn, *Phys. Rev.* **80** 580-594 (1950)
2. J. R. Suryan, *Proc. Indian Acad. Sci.* Sect. *A* **33,** 107 (1951)
3. Y. Nakayama, Visualized Flow, Fluid Motion in Basic and Engineering Situations Revealed by Flow Visualization (Pergamon, Oxford), pp. 1-6 (1988)
4. A. Einstein, *Ann. Phys.* **17**, 349 (1905)
5. D. G. Levitt, *Phys. Rev. A*, **8**, 3050 (1973)
6. P. A. Fedders, *Phys. Rev. B*, **17**, 40 (1973)
7. J. Kärger, M. Petzold, H. Pfeifer, S. Ernst, and J. Weitkamp, *J. Catal.*, **136**, 283 (1992)
8. K. Hahn and J. Kärger, *Phys. Rev. A* **28**, 3061 (1995)
9. E. O. Stejskal and J. E. Tanner, J. Chem. Phys. **42**, 288 (1965)
10. P. T. Callaghan, Principles of Nuclear Magnetic Resonance Microscopy, Oxford University Press Inc, New-York (1991)
11. S. Q. Zeng, A. Hunt, and R. Greif, *J. Non-Cryst. Sol.* **186**, 264 (1995)
12. P. R. Bevington, Data Reduction and Error Analysis for the Physical Sciences, McGraw-Hill, New York, (1969)
13. D. S. Sholl and K. A. Fichthorn, *Phys. Rev. Lett.***79**, 3569 (1997)

14. C. Rödenbeck, J. Kärger, and K. Hahn, *Phys. Rev. E* **55**, 5697 (1997)

15. D. S. Sholl, *Chem. Eng. J.* **74**, 25 (1999)

16. V. Gupta, S. S. Nivarthi, A. V. McCormick, and H. T. Davis, *Chem. Phys. Lett.* **247**, 596 (1995)

17. K. Hahn, J. Kärger, and V. Kukla, *Phys. Rev. Lett.* **76**, 2762 (1996)

18. V. Kukla, J. Kornatowski, D. Demuth, I. Girnus, H. Pfeifer, L. V. C. Rees, S. Schunk, K. K. Unger, and J. Kärger, *Science* **272**, 702 (1996)

19. H. Jobic, K. Hahn, J. Kärger, M. Bée, A. Tuel, M. Noack, I. Girnus, and G. J. Kearley, *J. Phys. Chem.* **101**, 5834 (1997)

20. H. R. Allcock and L. A. Siegel, *J. Am. Chem. Soc.* **86**, 5140 (1964)

21. A. Comotti, R. Simonutti, S. Stramare, and P. Sozzani, *Nanotechnology* **10**, 70 (1999)

22. A. Klemm, H. –P. Müller, and R. Kimmich, *Physica A* **266**, 242 (1999)

23. M. A. Springuel-Huet and J. Fraissard, *Chem. Phys. Lett.* **154**, 299 (1989)

24. J. A. Ripmeester and C. I. Ratcliffe, *J. Phys. Chem.* **99**, 619 (1995)

25. C. J. Jameson, A. K. Jameson, R. E. II Gerald, H. –M. Lim, *J. Phys. Chem. B*, **101**, 8418 (1997)

26. P. Sozzani, A. Comotti, R. Simonutti, T. Meersmann, J. W. Logan, and A. Pines, *Angew. Chem. Int. Ed.* **39**, 2695 (2000)

Chapter 5

Dynamic NMR microscopy of gas phase Poiseuille flow

Introduction

Fluid transport is an important phenomenon studied in a wide number of disciplines ranging from statistical mechanics to chemical engineering. One of the most intriguing aspects of those studies is the interplay between deterministic and stochastic molecular displacements arising, respectively, from coherent flow and Brownian motion. This problem was studied in detail by Taylor (1) and Aris (2) for the case of a fluid flowing through a pipe, where viscosity shear imposes a parabolic distribution of molecular displacements in a pipe flow, separating the entire ensemble into velocity streamlines with the smallest displacement at the walls of the pipe and largest displacements in the center. The increase in effective diffusion that arises from molecules randomly sampling streamlines with different velocities is referred to as

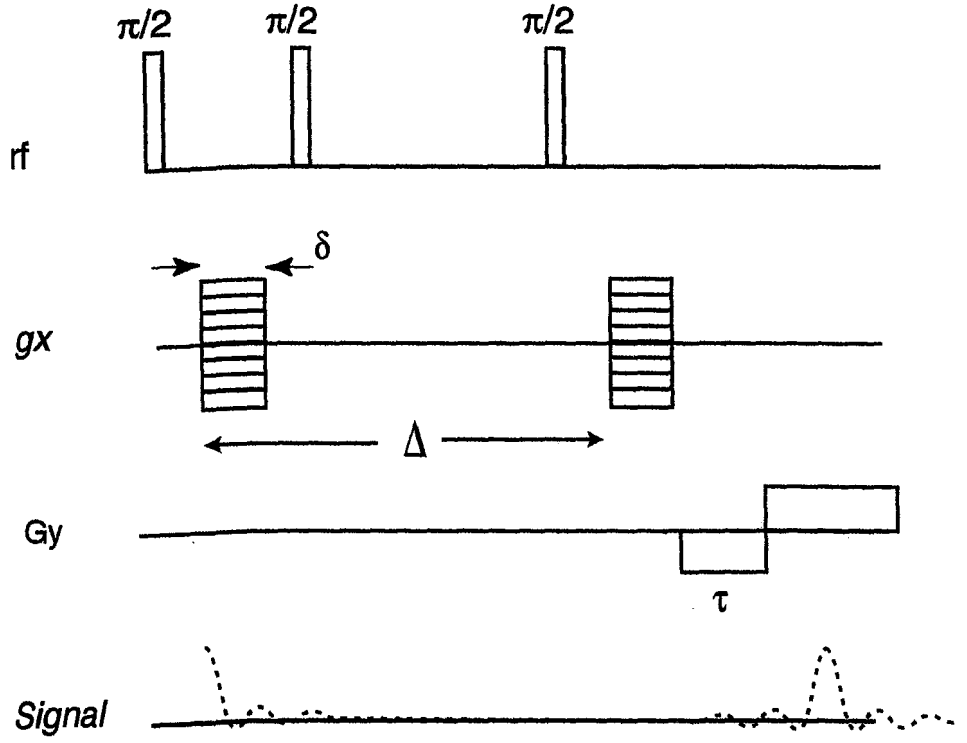

Figure 5.1. The stimulated echo dynamic NMR microscopy pulse sequence. The first gradient pulse (g_x) of duration (δ) serves to encode spatial position of each spin and the second gradient pulse has the effect of refocusing the magnetization. Molecular displacements (during time Δ) due to stochastic motion attenuate the amplitude, while coherent motion due to flow imposes a net phase shift on the observed signal. A second imaging gradient (G_y) is added in order to obtain spatial map of displacements. In the stimulated echo version during the displacement period, Δ, the magnetization is stored along the z-axis and is subject only to longitudinal relaxation.

in the flow direction (g_x) and spatial encoding gradient (G_y) in the direction perpendicular to the flow. Displacement of the spins during the period, Δ, between the gradient pulses, g, of duration, δ, results in a modification of the observed echo signal. The observed signal is given by

$$E(q) = \exp[\, i2\pi\Delta V_{ave}\, \mathbf{q} - 4\pi^2 D\, (\Delta - \delta/3\,)\mathbf{q}^2] \qquad (5.3)$$

where $q = (2\pi)^{-1}\gamma g\delta$ (9). Spatially resolved information is acquired by applying a frequency-encoding gradient (G_y) in a direction perpendicular to the flow. Following Fourier transformation, displacement profiles can be obtained by subsequent reconstruction of the velocity profiles. The simulations are performed using equation (5.3) for an ensemble of $N_{spins} = 10^4$, with corrections for spins that flow out of the tube during the observation time. The data processing for the simulations and the experiments is identical.

Results and Discussion

Temporal regimes of gas phase Poiseuille flow in a pipe

It is instructive to compare the displacement profile images for liquid pipe flow, (where diffusion is only a small perturbation) and gas pipe flow. Figure 5.2 shows a numerical simulation (A) and experimental data (B, C) of the 2D dynamic NMR microscopy experiment for water flowing in a pipe. The classical Poiseuille velocity profile is described by

$$V = V_{max}(1 - r^2/a^2) \qquad (5.4)$$

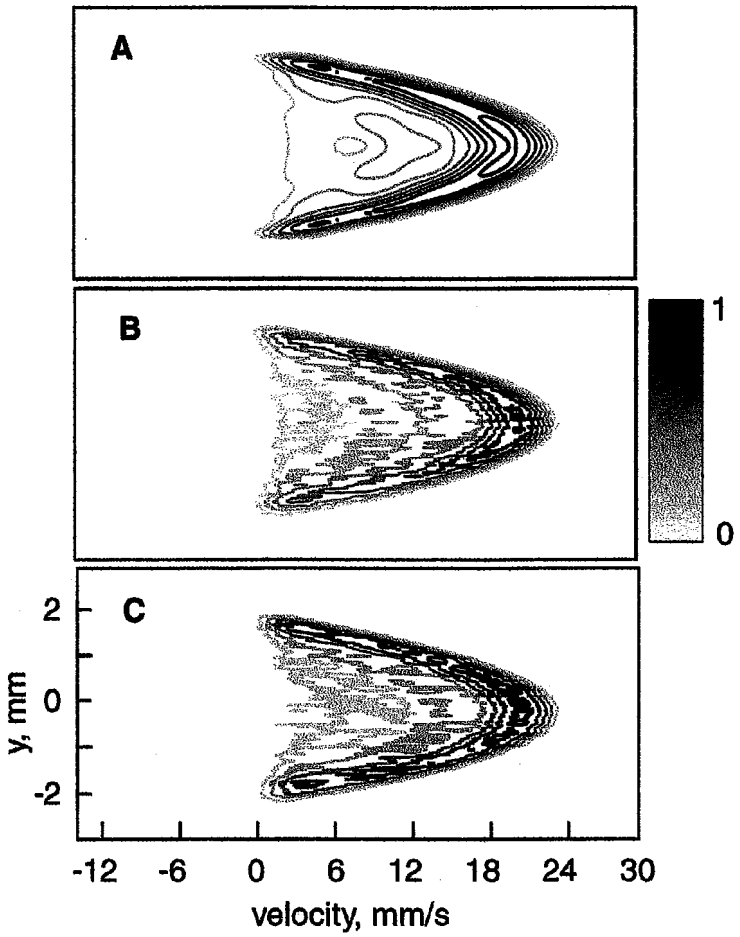

Figure 5.2

A Computer simulation of the joint spatial-velocity profile for water undergoing Poiseuille flow in a pipe (i.d. = 4 mm, $D_{water} = 2.2\times10^{-3}$ mm^2/s, $V_{ave} = 11.5$ mm/s, $\Delta = 20$ ms). The stimulated echo pulse sequence in Fig.5.1 is used to record 256×32 data sets with subsequent zero-filling to 512×256 points followed by 2D FFT.

B. Experimental data (same parameters as in A). **C.** Experimental data (same as A, $\Delta = 200$ ms)

where

$$V_{max} = \Delta P a^2 / 4\eta l \qquad (5.5)$$

and ΔP is the pressure decrease after the length l of the tube, η is the dynamic viscosity and a is the radius of the tube. The average velocity of water as determined by volumetric analysis is 11.5 mm/s. The extracted experimental average velocity, $V_{max}/2$ = 11.8 mm/s data is in good agreement with volumetric measurements. The non-zero signal intensity inside the parabola in the image is a result of spatial averaging of the spin density along the z-axis (i.e. a consequence of recording only one spatial dimension). As the observation time is increased the velocity profile of water retains its parabolic character very well (Fig. 5.2 C).

Figure 5.3 shows a numerical simulation (A) and experimental flow profiles (B - D) of xenon gas at 1.3 atm ($D = 4.5\ mm^2/2$, $V_{ave} = 25$ mm/s). The maximum velocity of liquid flow can be quickly estimated from the location of the parabola top in the displacement image. However for the gas phase profiles, the parabolic shape reflects large displacement due to longitudinal diffusion (compare Fig. 5.2B and Fig. 5.3B). In order to avoid a gross overestimation of the velocity, it is therefore necessary to extract the velocity values from the maximum of the Gaussian curves according to the procedure described in (9). Another difference between profiles in Fig. 5.2B and Fig. 5.3B is the large negative displacement of xenon gas for short observation time (also a consequence of longitudinal diffusion).

A prominent feature of Fig. 5.3 is the temporal progression of the molecular displacements. Naively we can identify two competing processes affecting the apparent velocity profiles, namely the longitudinal and transverse diffusion. In the short time limit,

the displacements due to longitudinal diffusion are dominant. Here, one would expect to see a very broad distribution of apparent velocities. In the long time limit, transverse diffusion "blurs" the radial dependence of the velocity, because the particles are able to sample the entire ensemble of the velocity streamlines.

An estimate of the displacement due to flow and diffusion as a function of time is shown in Fig. 5.4A. There are two distinct temporal regimes, first, for short times, the behavior is determined by longitudinal diffusion ($t < 15$ ms); this situation is represented by Fig. 5.3B. Second, for longer times, coherent displacements due to flow dominate as illustrated in Fig. 5.3C. The situation described in Figure 5.4A does not include transverse stochastic displacements, which leads to the asymptotic limit of Eq.2. This limit arises because particles are allowed to sample the entire ensemble of velocity streamlines during long observation times. Figure 5.3D ($\Delta = 130$ ms) shows displacement profile image approaching the asymptotic regime (the spin wash out of the detection region did not permit us to reach this limit completely).

The effective dispersion coefficient, D*, has been extracted from the images and is shown in Fig. 5.4B as a function of Δ. Different dispersion values for spins at the edges of the pipe and the spins in the center may provide useful information for an analysis of the boundaries relevant to the dispersion phenomena. Here the data are averaged over the pipe diameter, making the results equivalent to those from PFG experiments. In the short time limit, the points are fit to equation (1) the dashed line; however the effective dispersion is divergent for longer time in this method.

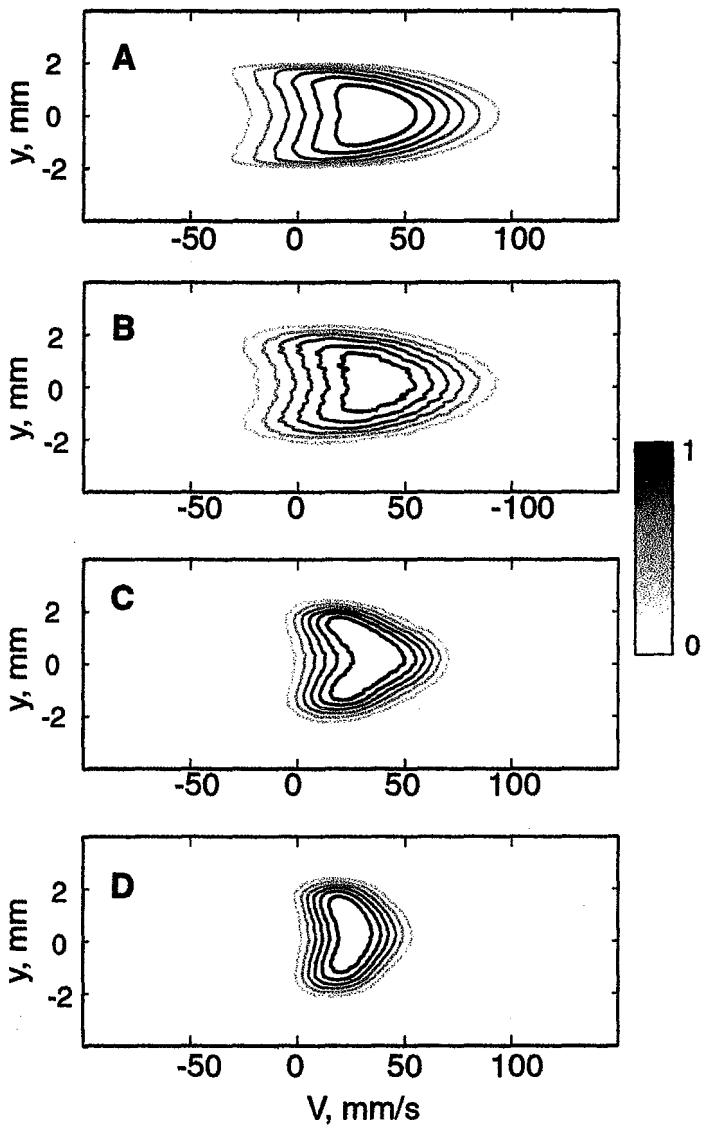

Figure 5.3

Joint spatial-velocity images of xenon undergoing Poiseuille flow in a pipe (i.d. = 4 mm, $D_{xe} = 4.5$ mm^2/s, $V_{ave} = 25$ mm/s). The 256×32 data points were collected using stimulated echo pulse sequence in Fig. 5.1 with subsequent zero-filling to 512×256 points followed by 2D FFT. Digital resolution in spatial direction (y) is 100 micrometers. **A.** Computer simulation ($\Delta = 10$ ms) **B.** Experiment ($\Delta = 10$ ms) **C.** Experiment ($\Delta = 60$ ms) **D.** Experiment ($\Delta = 130$ ms)

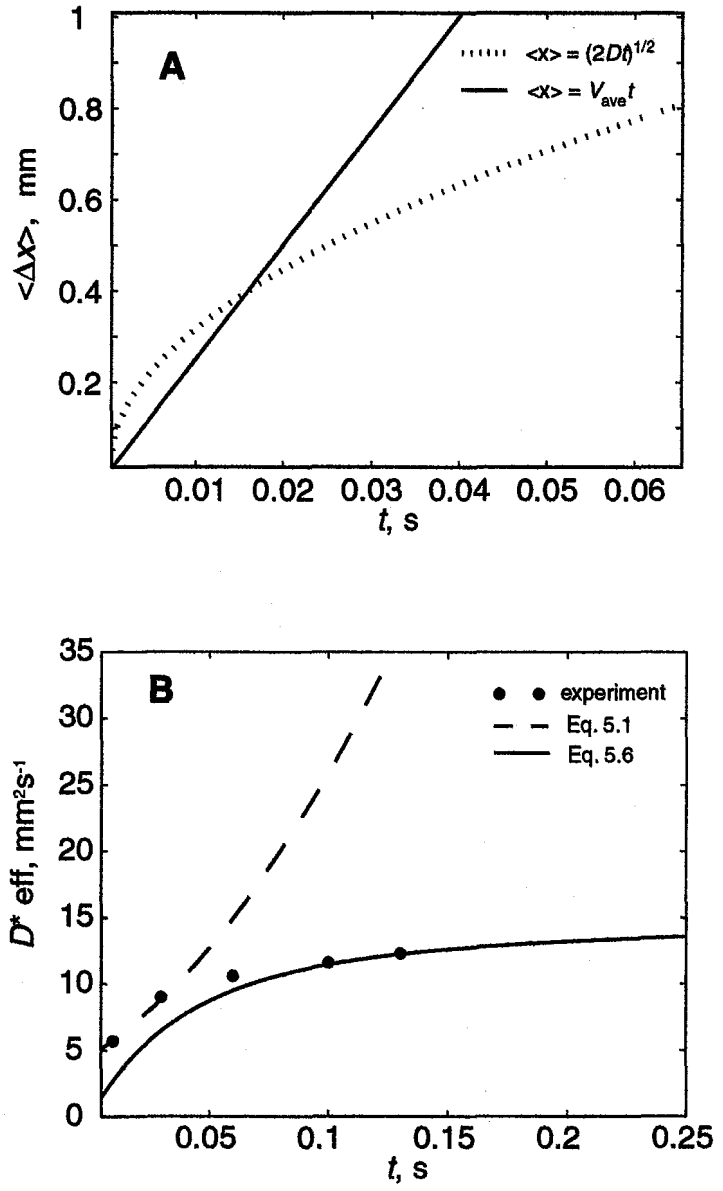

Figure 5. 4

A. The theoretical displacement due to velocity, $V_{ave}t$, and diffusion $\sqrt{2Dt}$ (dotted line) for the system described in Fig.5.3. **B**. The effective dispersion coefficient as a function of observation time, Δ.

An analytic expression for D*(Δ) has been presented in ref. 7:

$$D^*(\Delta)=V_{ave}^2\tau_c\left(1+\frac{\tau_c}{\Delta}[\exp(-\Delta/\tau_c)-1]\right) \tag{5.6}$$

where τ_c is the correlation time of the velocity fluctuations. The dispersion coefficient in the asymptotic limit is given as

$$D^*=V_{ave}^2\,\tau_c \tag{5.7}$$

For longer times, the experimental data points are correlated with the equation (6), the solid line in Fig. 3B. The velocity correlation time used for this fit (τ_c= 25 ms) matches the correlation time calculated from the asymptotic dispersion value in Eq. 5.2, (D* = 16 mm^2/s).

Edge enhancement effect in gas phase Poiseuille flow

The spin-echo version of the dynamic NMR experiment yields strongly distorted images for longer mixing times. Fig. 5.5A–C shows displacement profile images of xenon at 0.8 atm (recorded with the spin-echo version of the PFG NMR microscopy experiment). For short observation time, the displacement profile of xenon in Fig. 5.5A is equivalent to the data in Fig. 4.3B (note the slightly flatter parabolic shape due to lower pressure xenon gas). At longer measuring times such as in Fig. 5.5C (Δ = 100 ms), the intensity in the middle is significantly lower, resulting in a pronounced image "hole" in the center of the pipe. The small "natural" gradient, always present in the magnetic field, can often be neglected in liquid and solid state time-dependent NMR studies; however

such a gradient can play a significant role in the image contrast in the gas phase. This effect is referred to as "edge enhancement", an increase of the rate of magnetization decay for higher diffusion in the presence of the magnetic field gradient (8, 9). Consequently, a higher signal intensity persists at the edges where the diffusion is partially restricted. This effect can be exploited by imposing an imaging gradient in order to separate molecular displacements at the boundaries from those in the remainder of the system.

Indeed, it has been shown (10) that when an imaging gradient is applied for longer times (several milliseconds) in a xenon gas sample, only signal at the boundary remains. Figure 5.6 shows the application of the edge enhancement "filter" for gas phase Poiseuille flow. A stimulated echo pulse sequence (Fig. 5.1) with longer imaging gradient encoding time, (τ = 5 ms), is used to select atoms at boundaries, with the displacement spectral window, **q**, maintained constant. Figure 5.6A (Δ = 3 ms) demonstrates an almost symmetrical displacement distribution about $\Delta x = 0$ for the particles at the walls, corresponding to a very small flow contribution. On the other hand for Δ = 30 ms (Fig. 5.6B), the presence of unidirectional flow and mixing of the fast components from the middle of the pipe is significant.

Such an edge enhancement "filter" may be inserted at any time of the pulse sequence (the only requirement is that the spins have to be in the x-y plane during the application of the gradient). When the "filter" occurs at the beginning of the pulse sequence, it might be possible to monitor the exchange between the slow and fast components (e.g. the appearance of the spins at the center of the pipe for longer Δ).

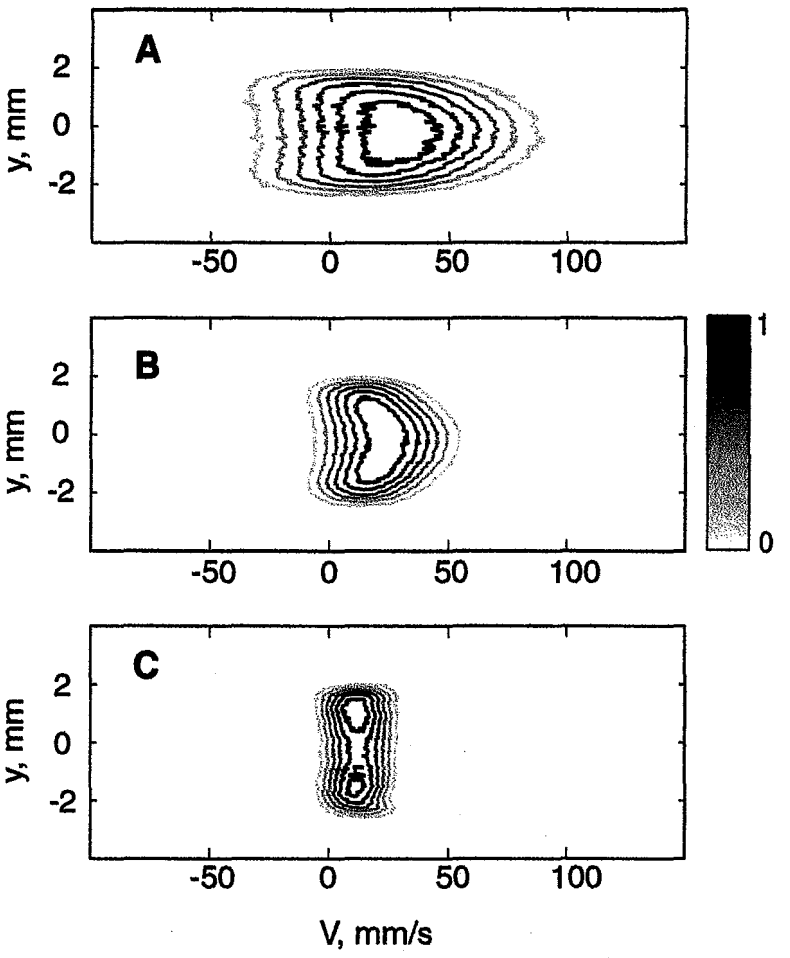

Figure 5.5

Poiseuille pipe flow displacement profiles (V_{ave} = 20 mm/s) for xenon at 0.8 atm recorded using spin-echo version of the dynamic NMR microscopy pulse sequence. **A.** Experimental data for Δ = 10 ms. **B.** Experimental data for Δ = 50 ms. **C.** Experimental data for Δ=100 ms. The reduced signal intensity in the middle of the pipe is a consequence of the edge enhancement effect induced by large random displacements under the natural inhomogeneity gradient of the magnet.

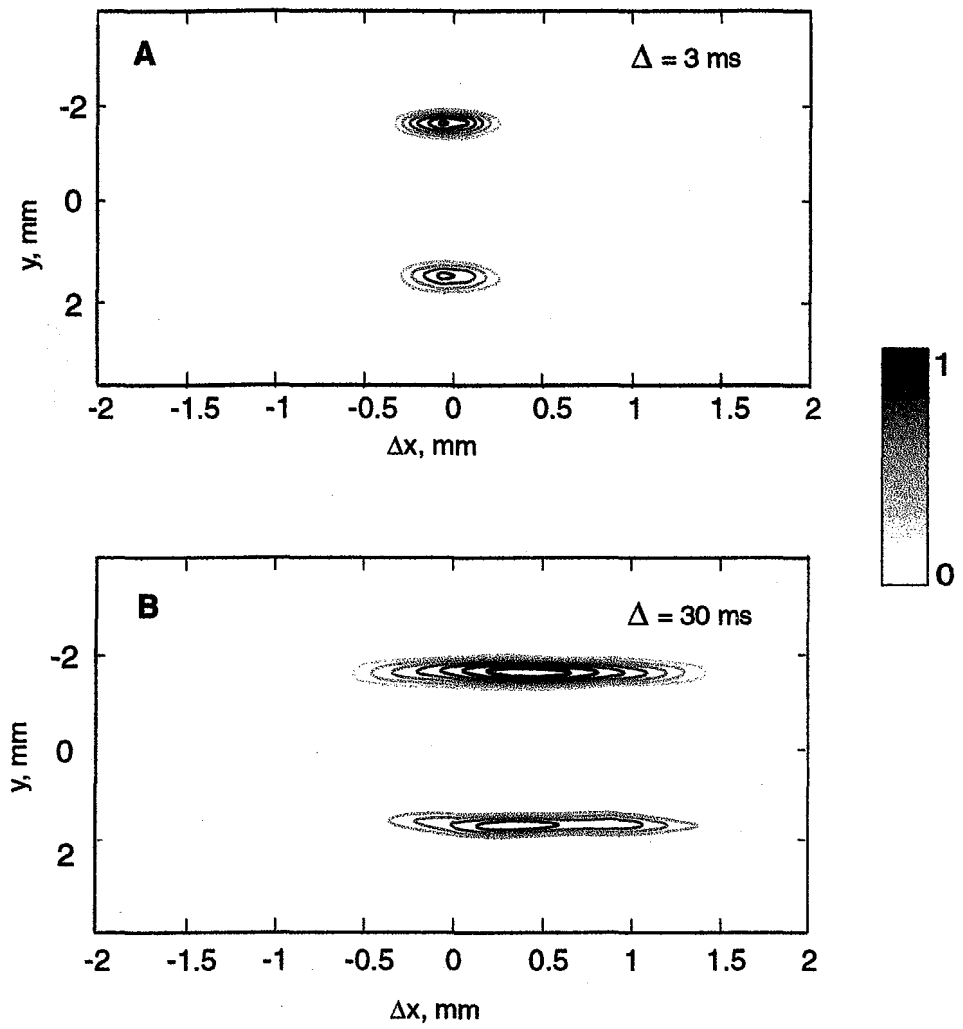

Figure 5.6

Poiseuille flow displacement profiles (V_{ave} = 27 mm/s, D = 8 mm^2/s) for xenon at 0.7 atm recorded with stimulated echo pulse sequence in Fig.1A. Only particles at the walls (slowly flowing components) are selected by the edge enhancement "filter". Modified imaging gradient time duration (τ = 5 ms) is used when 512×16 data points were collected (with subsequent zero-filling to 1024×32 points followed by 2D FFT). Digital resolution in spatial direction (y) is 100 micrometers.

A. Displacement time, Δ = 3 ms. **B.** Displacement time, Δ = 30 ms.

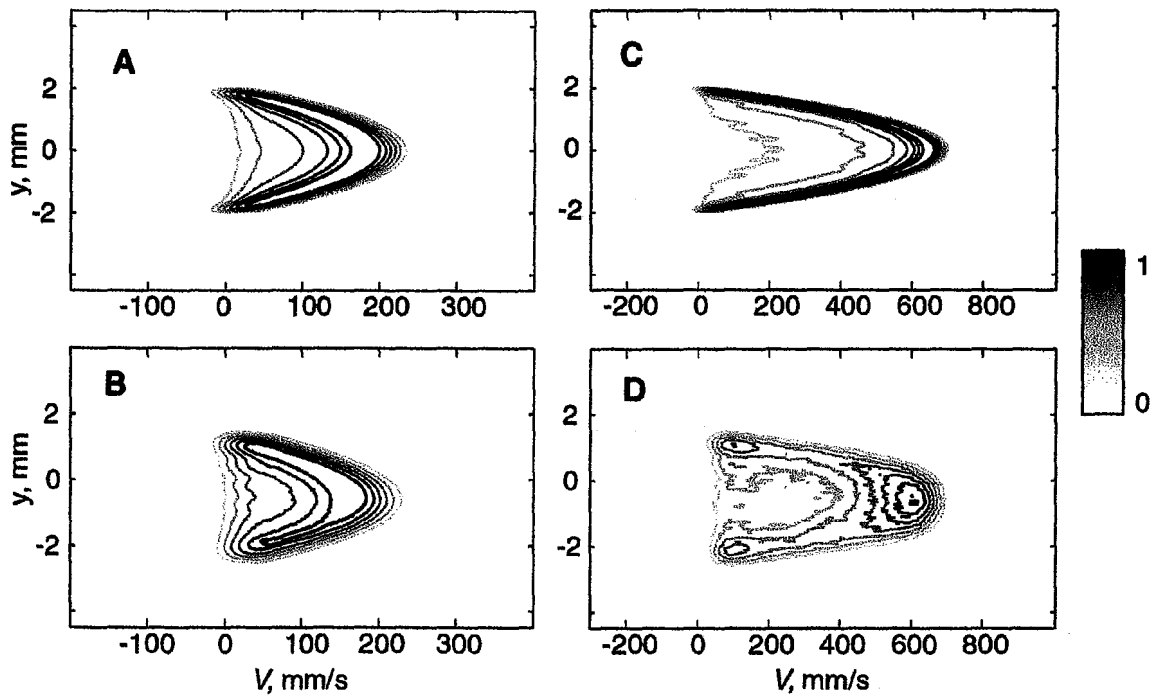

Figure 5.7

Joint spatial-velocity images for xenon flowing at two different velocities (P_{xe} = 3 atm). A. Computer simulation for xenon flow at V_{max}= 200 mm/s. B. Experimental data. C. Computer simulation for xenon flow at V_{max} = 700 mm/s (does not include the effects of turbulence). D. Experimental data. The onset of turbulence for this high velocity image is manifested via the blunting of the streamwise velocity profile.

Conclusion

A dynamic NMR microscopy study of gas phase Poiseuille flow with large stochastic displacements in different temporal regimes has been presented. The results indicate that longitudinal diffusion dominates the displacement profile for short observation time. The parabolic distribution of displacements due to unidirectional flow becomes more pronounced at longer observation times. Both diffusion and flow define the velocity profile as the system approaches the asymptotic limit. Rapid diffusion of the gas necessitates a stimulated echo PFG version for long evolution times ($\Delta > 100$ ms).

Continuous flow laser-polarized ^{129}Xe technique provides great versatility in preparing custom systems for studying transport phenomena (both diffusion and velocity can be varied by almost two orders of magnitude in our system). By adjusting flow rates and gas pressure it is possible to monitor displacements via dynamic NMR microscopy for Peclet numbers ranging from 1 to ca. 1000. Figure 5.7 shows xenon gas pipe flow in a regime where fast flow rates make velocity profiles of xenon gas approach those of liquids. For very fast flow rates, a transition to turbulence can be observed (Fig. 5.7D), manifested via the blunting of the velocity streamlines. Therefore this system shows a great potential for flow dynamics applications in both laminar and turbulent regimes.

References

1. G. I. Taylor, *Proc. Roy. Soc. London,* Ser. A **219**, 186 (1953)
2. R. Aris, *Proc. Roy. Soc. London,* Ser. A **235**, 67 (1956)
3. H. Brenner, *Phys. Chem. Hydrodyn.* **1**, 91 (1980)
4. C. Van den Broeck, *Physica* A **112A**, 343 (1982)
5. S. L. Codd, B. Manz, J. D. Symour, and P. T. Callaghan, *Phys. Rev. E,* **60**, 3491 (1999)
6. P. T. Callaghan, Principles of Nuclear Magnetic Resonance Microscopy, Oxford, University Press Inc, New-York, (1991)
7. J. D. Seymour and P. T. Callaghan, *AIChE. J.* **43**, 2096 (1997)
8. B. Putz, D. Barsky, and K. Schulten, *J. Magn. Reson.*, **97**, 27 (1992)
9. P. Callaghan, A. Coy, L. C. Forde, and C. J. Rofe, *J. Magn. Reson.*, Ser. A **101**, 347 (1993)
10. Y. -Q. Song, B. M. Goodson, B. Sheridan, T. M. de Swiet, and A. Pines, *J. Chem. Phys.* **108**, 6233 (1998)

Chapter 6

Laser-polarized ^{129}Xe NMR study of xenon binding in Cryptophane-A

Introduction

Considerable work has capitalized on the utility of ^{129}Xe (I = 1/2) as a magnetic resonance probe of molecules, materials and biological systems (1 - 5). Much of this work has utilized the highly sensitive chemical shift of ^{129}Xe in order to reveal properties of the xenon environment. Selective polarization transfer from ^{1}H to ^{129}Xe has also been used to investigate the sites of xenon binding (6) and xenon preferential solvation (7). The xenon polarization created by the optical pumping process can be transferred via cross-relaxation to molecules in solution (8, 9) and to surfaces (10, 11), a process called the "spin polarization-induced nuclear Overhauser effect" (SPINOE). Temporary binding of xenon to the molecular cavities (e.g. α-cyclodextrin) was shown to yield distance-selective cross relaxation rates, thereby enhancing the NMR signal of protons to a degree dictated by their proximity to the xenon binding site (12). These results suggest that SPINOE polarization transfer could be utilized to study structure and dynamics in molecules that interact with xenon.

Xenon is known to interact with a variety of systems, including proteins in solution (13, 14) and in crystals (15, 16). Recent work in proteins has been motivated by the desire to map hydrophobic sites and also to use xenon/protein complexes as heavy-atom derivatives for X-ray structure determination (17). Studies using xenon dissolved in lipid vesicles as a model for anesthetic action showed that xenon is preferentially attracted to amphiphilic regions in lipid membranes (7). Finally xenon has been shown to form a variety of inclusion compounds with a-cyclodextrin (6, 18), hemicarcerands (19), self-assembling dimers (20) and most recently, cryptophane-A (21).

Cryptophane-A (MW = 895.02 g/mol) is a nearly spherical cage molecule composed of two cyclotriveratrylene bowls connected by three -OCH_2CH_2O- spacer bridges (Figure 1). In a recent study, it was shown that the complex of xenon and cryptophane-A exhibits particularly strong binding, with a reported association constant (K) greater than $3000M^{-1}$ at 278 K (21), whereas K for the xenon/a-cyclodextrin complex in H_2O has been reported to be on the order of 20 M^{-1}(22). The cryptophane-A molecule can adopt various conformations that affect the size of the cavity and the stability of the host-guest complex; the dynamics of the host are expected to influence the manner in which the guest is bound and released (23).

What follows is a general theoretical framework describing the SPINOE in solution, with stress placed on the interpretation of SPINOE results in terms of the interactions between xenon and its environment. Also ^{129}Xe NMR and SPINOE experiments for laser-polarized xenon interaction with cryptophane-A in solution are described.

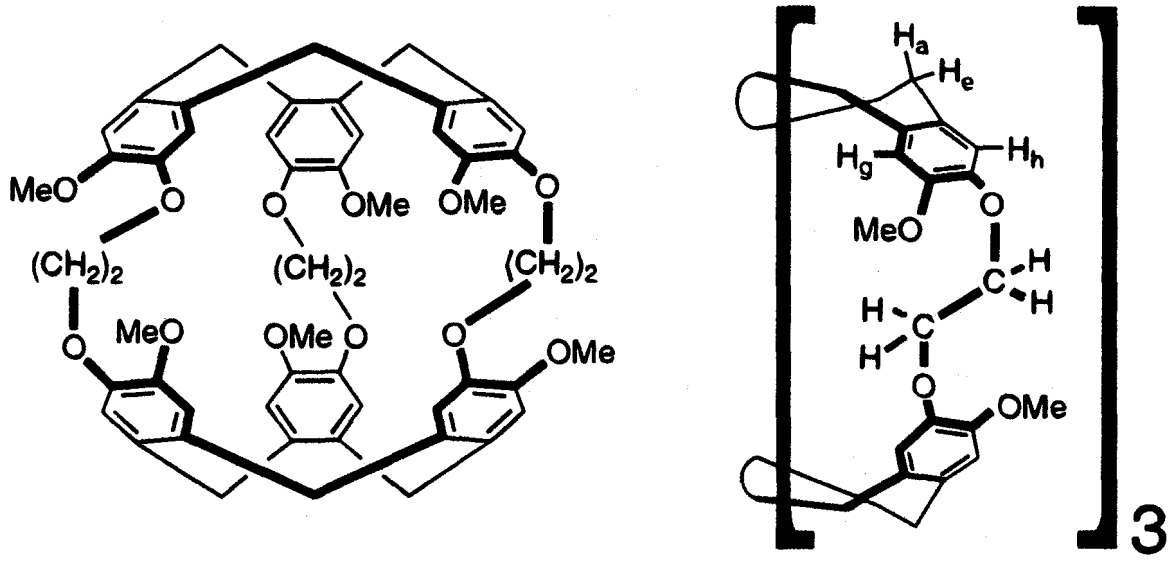

Figure 6.1. Structure of cryptophane-A and atom labeling used in the ^{1}H spectrum.

Theory

Solomon Equations for a Two-Spin System

Cross-relaxation between any two spins, I and S, is described by the Solomon equations (24, 25)

$$dI_z/dt = -\rho_I(I_z-I_0)-\sigma_{IS}(S_z-S_0) \quad (6.1)$$

$$dS_z/dt = -\rho_S(S_z-S_0)-\sigma_{IS}(I_z-I_0) \quad (6.2)$$

where I_z and S_z are the average values of the z component of the I and S nuclear spin operators, and I_0 and S_0 are the equilibrium values ($I_0 = I(I+1)\eta\gamma_I B_0/3k_B T$ and similarly for spin S). The values ρ_S, ρ_I and σ_{IS} are respectively the auto-relaxation and cross-relaxation rate constants. A full solution to the Solomon equations can be found in the literature elsewhere (26). If the nuclear spin-lattice relaxation of spin S is much slower than that of spin I (normally the case for S = ^{129}Xe when dissolved in solution (27)), the change in spin polarization of spin I is well-approximated by

$$f_I(t)=f_I(0)e^{-\rho_I t} - S_0/I_0\, f_S(0)\sigma_{IS}/\rho_I(1-e^{-\rho_I t}) \quad (6.3)$$

where $f_I(t) = (I_z(t)-I_0)/I_0$ is the fractional polarization enhancement of spin I (and similarly for spin S). Equation 6.3 is the solution to equation 6.1 given a constant polarization of spin S, and is valid in the short time limit (i. e. for times short relative to the spin-lattice relaxation time of spin S, $T_1^S = 1/\rho_S$) (see Figure 6.2).

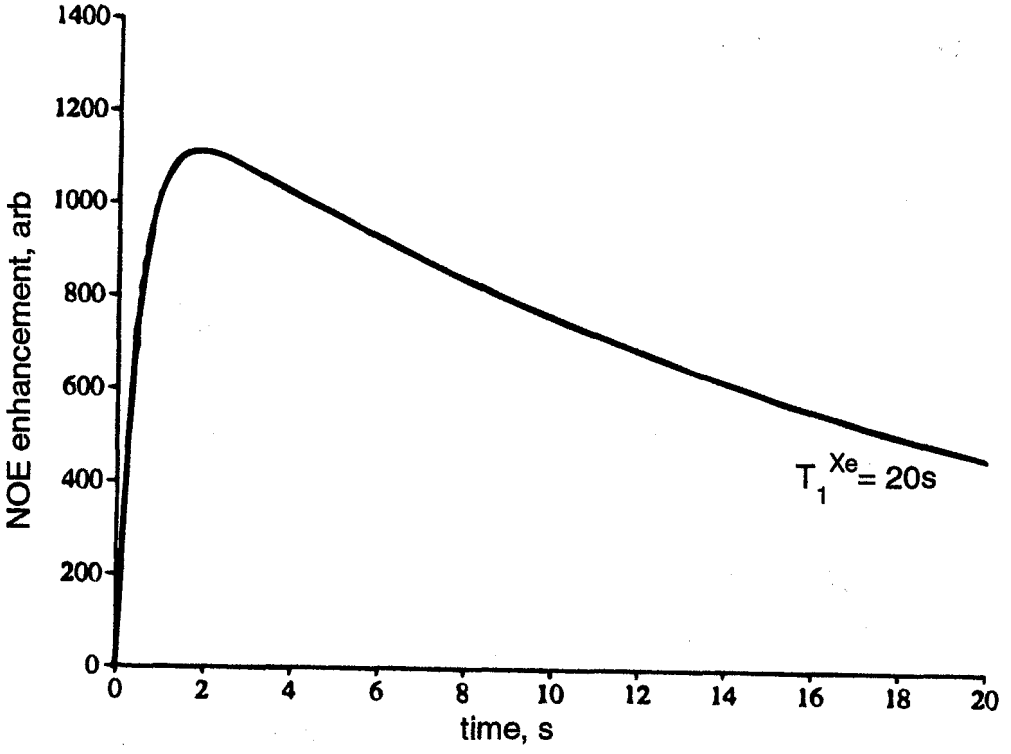

Figure 6.2. Calculated time-dependence of the SPINOE signal, including the exponential decay caused by the eventual 129Xe spin-lattice relaxation. Curves were calculated using ρ_I=2 s^{-1}, σ_{IS} = 0.001 s^{-1}, and ρ_S = 0.05 s^{-1}.

The second term on the right hand side of Eq. 6.3 describes the time evolution of the polarization of spin I originating from S polarizing I type of transfer. For intermolecular polarization transfer, the magnitude of this term is often small with respect to the equilibrium polarization of spin I, requiring an NMR pulse sequence dedicated to the direct measurement of the SPINOE difference. Such a heteronuclear difference NOE pulse sequence is described in the Experimental section, in addition to a full version expression analogous to Eq. 6.3 that accounts for experimental considerations and the relaxation of spin S.

General considerations for ^{129}Xe □ ^{1}H polarization transfer and cross-relaxation rates

In the framework of the dipolar-coupled two-spin model, the auto-relaxation of spin I (^{1}H) is solely a consequence of dipole-dipole interaction with spin S (^{129}Xe). However, molecules in solution contain many spin systems; therefore, intermolecular H-Xe dipole-dipole interactions are not likely to contribute significantly to the H auto-relaxation rate. For solutes at low concentration in deuterated solvents, when no paramagnetic species are present, intramolecular H-H dipole-dipole interactions are expected to dominate the auto-relaxation of protons in molecules large enough to bind xenon (although other mechanisms, such as spin-rotation coupling, may contribute to relaxation of small molecules such as benzene or parts of molecules, like methyl groups). Therefore, the simplest realistic model for Xe-H polarization transfer requires at least three-spin system: two interaction H's and one xenon in dipolar interaction with one of

the H sites. However for the purpose of interpreting experimental NMR spectrum, the two-spin system is sufficient.

The quantity σ_{HXe} largely controls the $^{129}Xe \rightarrow {}^{1}H$ polarization transfer. Assuming an exponential decay for the H-Xe dipole-dipole interaction correlation function, the cross-relaxation rate is given by (25)

$$\sigma_{XeH} = \left(\frac{\mu_0}{4\pi}\right)^2 \frac{\eta^2 \gamma_H^2 \gamma_{Xe}^2}{10} \left\langle \frac{1}{r_{HXe}^6} \right\rangle [6J(\omega_H + \omega_{Xe}) - J(\omega_H - \omega_{Xe})] \qquad (6.4)$$

with $J(\omega) = \frac{\tau_c}{1 + \omega^2 \tau_c^2}$

where τ_c is the correlation time associated with the fluctuations of the H-Xe dipole-dipole interactions, r_{HXe} is the H-Xe internuclear distance. Both $\left\langle r_{HXe}^{-6} \right\rangle$ and τ_c control the amplitude and selectivity of the $^{129}Xe \rightarrow {}^{1}H$ polarization transfer.

Experimental

Deuterated 1, 1, 2, 2-tetrachloroethane, $(CDCl_2)_2$, is purchased from Aldrich. Approximately 2 mL of a ~0.05 M solution of cryptophane-A in $(CDCl_2)_2$ is placed in a 10-mm NMR tube equipped with a sidearm, and Teflon stopcocks are used to isolate the sample and the sidearm from each other and from the atmosphere. Helium gas is gently bubbled through the solution for 5-10 min to displace any other gases complexed by cryptophane-A. The sample is then degassed by several freeze-pump-thaw cycles on a vacuum line.

The batch mode optical pumping apparatus used in the experiment is described in detail in Chapter 2. Following optical pumping, laser-polarized ^{129}Xe is frozen into the sidearm of the NMR tube, transported to the spectrometer, and sublimated in the fringe field of the NMR magnet. After the xenon reservoir was opened, the sample tube shaken, and the tube inserted into the magnet, the NMR experiment was immediately performed.

^{1}H and ^{129}Xe NMR spectra are recorded at room temperature (~22 °C) on a Varian/Chemagnetics CMX-400 Infinity NMR spectrometer operating at a ^{1}H frequency of 400.15 MHz. Laser-polarized ^{129}Xe were obtained using rf pulses of small tipping angle (typically 1-5°) to preserve ^{129}Xe magnetization. Measurements of ^{1}H spin-lattice relaxation time, T_1 are made using the inversion recovery technique and determined using a least squares fitting procedure.

The SPINOE spectra are obtained using the NMR pulse sequence shown in Figure 6.3. This sequence is a variant of a difference NOE sequence developed by Shaka and co-workers, capable of efficiently suppressing the equilibrium signal, thus permitting the direct observation of NOE signals as low as $\sim 10^{-4}$ of the equilibrium signal. Prior to the detection of ^{1}H SPINOE signals, the polarization of ^{129}Xe is measured using a pulse of small tipping angle. The equilibrium ^{1}H is first saturated by 90° and gradient pulses, and the saturation is maintained by a 180° pulse followed immediately by a gradient pulse. A ^{129}Xe 180° pulse allows SPINOE signals to accumulate during the mixing periods τ_1 and τ_2. The total mixing period, $t = \tau_1 + \tau_2$, was in the range of the ^{1}H T_1's but was short compared to the ^{129}Xe T_1. The ratio τ_1/τ_2 is chosen to minimize the overall equilibrium ^{1}H signal observed in the absence of ^{1}H - ^{129}Xe cross-relaxation.

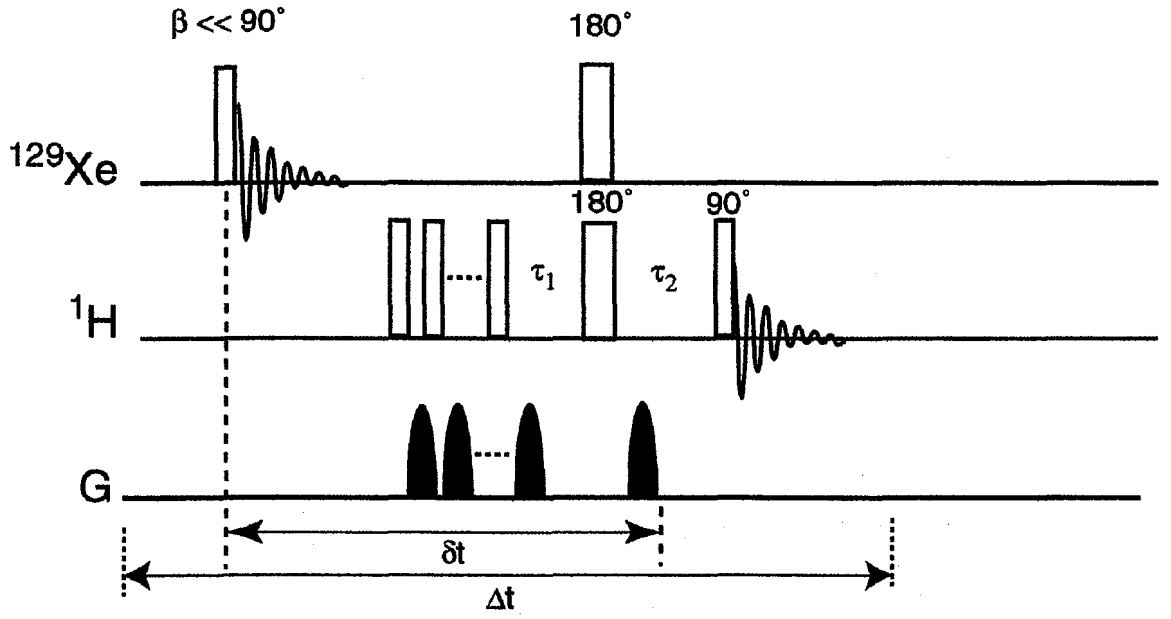

Figure 6.3 Heteronuclear difference NOE pulse sequence for ^{129}Xe-^{1}H SPINOE NMR experiments.

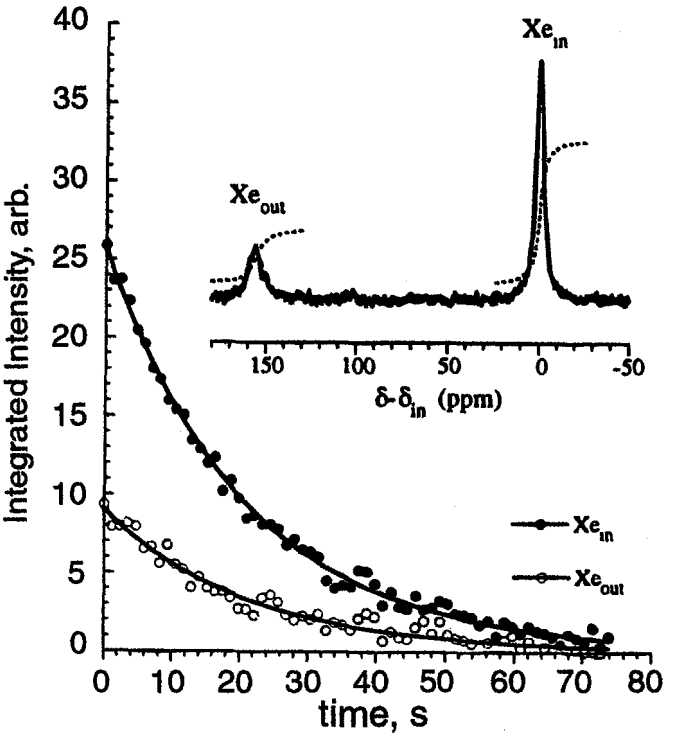

Figure 6.4

^{129}Xe NMR spectrum of laser-polarized xenon (inset) dissolved in a ~0.5 M solution of cryptophane-A in $(CDCl_2)_2$ and time evolution of the integrated intensities. The small amount of xenon used in this experiment is reflected in the fact that $[Xe]_{in} > [Xe]_{out}$

Results and Discussion

Figure 6.4 (inset) shows ^{129}Xe spectra of xenon dissolved in the cryptophane-A solution, which exhibits two lines separated by ~160 ppm and considerably broadened due to chemical exchange. The higher field signal corresponds to the xenon trapped in the cryptophane-A cavity, Xe_{in}, with a chemical shift ~60 ppm downfield with respect to the xenon gas resonance extrapolated to zero pressure. The protons' T_1 relaxation values for cryptophane-A are listed in Table 1. The longest relaxation times, ~0.8 s, are those of the methoxy and aromatic hydrogens. Relaxation of ^{129}Xe in this system is slow with respect to ^1H relaxation (T_1^{ave} of xenon was found to be 22 s), therefore equation (6.3) can be used when considering $^{129}Xe \rightarrow {}^1H$ SPINOE polarization transfer.

Table 1. Spin-Lattice Relaxation Times, SPINOE Enhancements, Relative H-Xe Cross-Relaxation Rates for Different Protons of Cryptophane-A

proton	type	T_1^H (s)	SPINOE (%)	$\sigma_{HXe}/\sigma_{H\ Xe}$	$\langle r_{HXe}^{-6}\rangle / \langle r_{H\ Xe}^{-6}\rangle$
aromatic	H_g, H_h	0.80	11.0	(1.00)	(1.00)
axial	H_a	0.27	3.0	0.47	0.3–0.4
linker	H_j, $H_{j'}$	0.36	5.2	0.67	0.3
linker	H_k, $H_{k'}$	0.41	13.0	1.55	1.5–1.8
methoxy	Me	0.83	2.6	0.23	0.1–0.3
equatorial	H_e	0.35	2.7	0.35	0.3–0.4

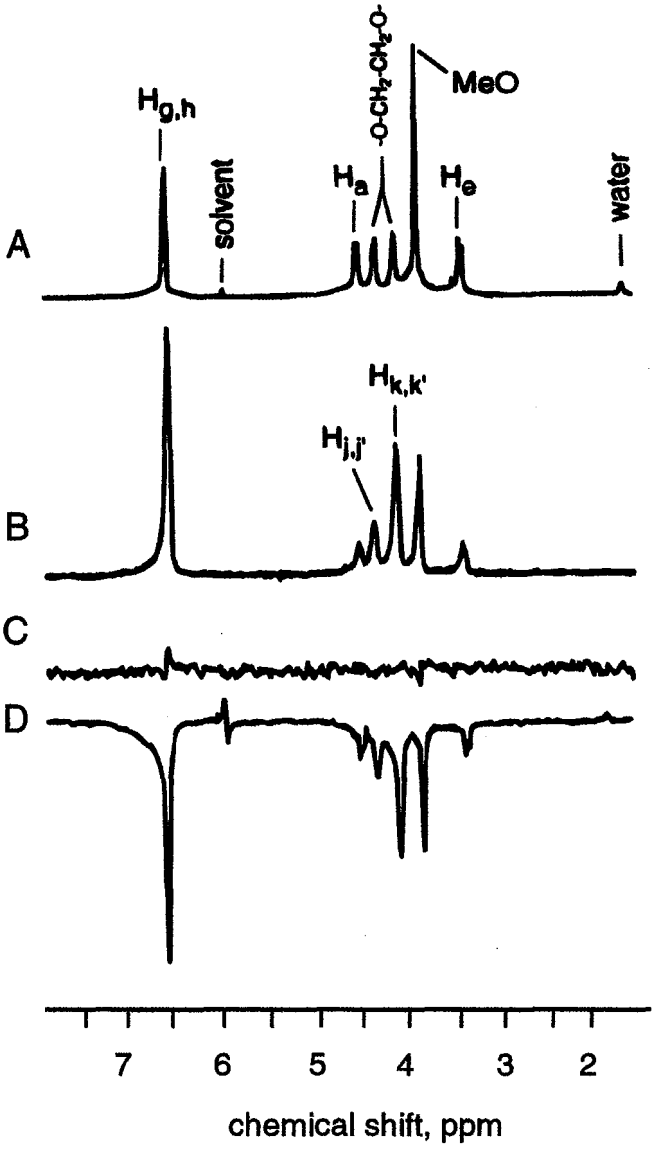

Figure 6.5 A. ^{1}H NMR equilibrium spectrum of 0.05 M cryptophane-A in $(CDCl_2)_2$ with chemical shift assignments. **B.** ^{1}H SPINOE spectrum acquired with the pulse sequence shown in Figure 5 following the introduction of positively polarized xenon to the solution. **C**. As in B, but with ^{129}Xe at thermal equilibrium, demonstrating complete suppression of all contribution to the 1H NMR signal. **D**. ^{1}H SPINOE spectrum acquired during a second experiment in which negatively polarized 129Xe (prepared by inverting the direction of the magnetic field) was used.

The relative intensities in the SPINOE spectra (Figure 6.5B and D) differ from those in the equilibrium spectrum. The equilibrium spectrum is dominated by the signal of the methoxy group, while in the SPINOE spectra the signal from the aromatic protons is the most intense. The observed ^1H enhancements in Figure 6.5B range between 3 and 13% (see Table 1). Additionally, it is clear that the selectivity of the SPINOE is not primarily a consequence of unequal ^1H relaxation times, as the T_1^H for the methoxy and aromatic protons are similar.

The determination of the H-Xe cross-relaxation rates requires the value of the ^{129}Xe polarization enhancement. Since ^1H SPINOE spectrum is the difference of two acquisitions, Eq. 6.3 can be rewritten as

$$\Delta f_H(\tau) = \frac{\gamma Xe}{\gamma H} f_{xe}^{obs}(0)\cos(\beta)e^{-\delta t/T_1^{Xe}}\sigma_{HXe}T_1^H\{(1-e^{-t/T_1^H})-(1-r)(1-e^{-\tau_2/T_1^H})\} \quad (6.5)$$

where $f_{xe}^{obs}(0)$ is estimated from the quantatative comparison of the integrated intensities of the laser-polarized and equilibrium ^{129}Xe NMR spectra. For the SPINOE experiment in Figure 6.5 B, the ^{129}Xe polarization enhancement is estimated to be ~ 13,000. However the uncertainty of this value is very high (ca 50%), resulting from experimental difficulties with inverting both ^{129}Xe resonances during acquisition, exchange broadening of the 129Xe lines (500 Hz), low signal-to-noise ratio and long ^{129}Xe T_1's in the equilibrium spectra (~50 to 90 s), and the vastly different acquisition conditions (gain, pulse length, pulse power, etc.). From the experimental data given in Table 1, and using $f_{xe}^{obs}(0)$ value, σ_{HXe} was estimated to be $\sim 1.2*10^{-4}$ s^{-1} for the aromatic protons. This number is 2 orders of magnitude larger than the value expected for H-Xe cross-relaxation

rates originating from diffusive coupling alone; the observed SPINOE enhancements can therefore be considered as originating entirely from the binding of xenon.

The largest σ_{HXe} values characterizing the binding of xenon to cryptophane-A are found to be significantly smaller (5 to 10-fold) than the largest values observed when xenon binds to α-cyclodextrin (12). Such a discrepancy is unlikely to originate from differences in dynamics of the $^{129}Xe \rightarrow {}^{1}H$ polarization transfer. This difference in the σ_{HXe} values suggests differences in the structure of these complexes. Given $\tau_c = 0.6$ ns and $\sigma_{HXe} = (1\text{-}4) \times 10^{-4}\ s^{-1}$, equation 6.4 leads to a $\langle r^{-6}_{HXe} \rangle$ value in the range $(0.5\text{-}2) \times 10^{-4}$ Å^{-6}; thus, the average distance between the aromatic protons and the xenon atom is 4.1-5.2 Å. On the basis of an X-ray structure of α-cyclodextrin (28), the r_{HXe} values between a xenon atom positioned at the center of the cavity and the nearest protons are found to be in the range of 3.2-3.8 Å. These calculated ranges of proton-to-xenon distances translate into a 4-to 8-fold factor increase in the cross-relaxation rates (neglecting dynamical effects), in agreement with the experimental observations.

Conclusion

The polarization transfer via NOE effect using laser-polarizaed xenon was investigated for xenon trapped in cryptophane-A complex within the theoretical and experimental framework. Laser-polarized xenon is a useful probe of xenon environment in solution. Selective ^{1}H ehnancements were observed, permitting the more complete assignment of ^{1}H NMR spectrum to be obtained. By using laser-polarized ^{129}Xe and SPINOE experiments, detailed microscopic information can be obtained, demonstrating

the utility of such methods to directly probe molecular structure and dynamics in solution.

References

1. J. Fraissard and T. Ito, *Zeolites* **8**, 350-361, (1988)
2. P. J. Barrie and J. Klinowski, *Prog. Nucl. Magn. Reson. Spectrosc.* **24**, 91 (1992)
3. T. Pietraβ and H. Gaede, *Adv. Mater.* **7**, 826 (1995)
4. M. S. Albert and D. Balamore, *Nucl. Instrum. Meth. Phys. Res.*, Sect. A **402**, 441, (1998)
5. J. Jokisaari, *Prog. Nucl. Magn. Reson. Spectrosc.* **26**, 1 (1994)
6. K. Bartik, M. Luhmer, S. J. Heyes, R. Ottinger, J. Reisse, *J. Magn. Reson. B*, **109**, 164 (1995)
7. Y. Xu, P. Tang, *Biochim. Biophys. Acta* **1323**, 154 (1997)
8. G. Navon, Y. –Q. Song, T. Rööm, S. Appelt, R. E. Taylor, and A. Pines, *Science* **271**, 1848 (1996)
9. R. J. Fitzgerald, K. L. Sauer, and W. Happer, *Chem. Phys. Lett.* **284**, 87 (1998)
10. T. Rööm, S. Appelt, R. Seydoux, A. Pines, and E. L. Hahn, *Phys. Rev. B* **55**, 11604 (1997)
11. E. Brunner, M. Haake, A. Pines, J. Reimer, and R. Seydoux, *Chem. Phys. Lett.* **290**, 112 (1998)
12. Y. –Q. Song, B. M. Goodson, R. E. Taylor, D. D. Laws, G. Navon, and A. Pines, *Angew. Chem. Int. Ed. Engl.* **36**, 2368 (1997)
13. R. F. Tilton, Jr. and I. D. Kuntz, *Biochemistry*, **21**, 6850 (1982)
14. S. McKim and J. F. Hinton, *Biochim. Biophys. Acta* **1193**, 186 (1994)
15. B. P. Shoenborn, *Nature* **208**, 760 (1965)

16. M. Shlitz, T. Prangé, and R. Fourme, *J. Apl. Crystallogr.* **27**, 950 (1994)

17. M. Shlitz, R. Fourme, I. Broutin, and T. Prangé, *Structure* **3**, 309 (1995)

18. J. A. Ripmeester, C. I. Ratcliffe, and J. S. Tse, *J. Chem. Soc.*, Faraday Trans. **84**, 3731 (1988)

19. D. J. Cram, M. E. Tanner, and C. B. Knobler, *J. Am. Chem. Soc.* **113**, 7717 (1991)

20. N. Branda, R. M .Grotzfeld, C. Valdes, and J. Rebek, Jr., *J. Am. Chem. Soc.* **117**, 85 (1995)

21. K. Bartik, M. Luhmer, J. –P. Dutasta, A. Collet, and J. Reisse, *J. Am. Chem. Soc.* **120**, 784 (1998)

22. T. K. Hitchens and R. G. Bryant, *J. Magn. Reson.* **124**, 227 (1997)

23. P. D. Kirchhoff, M. B. Bass, B. A. Hanks, J. M. Briggs, A. Collet, and J. A. McCammon, *J. Am. Chem. Soc.* **118**, 3237 (1996)

24. I. Solomon, *Phys. Rev.* **99**, 559, (1996)

25. J. H. Noggle and R. E. Schirmer, The Nuclear Overhauser Effect: Chemical Applications; Academic Press: New York, London (1971)

26. J. Cavahagh, W. J. Fairbrother, A. G. Palmer, and N. J. Skelton, Protein NMR Spectroscopy: Principles and Practice, Academic Press: San Diego (1996)

27. Spin-lattice relation times of hundreds of seconds are usually observed for 129Xe dissolved in most simple solvents. Binding of xenon to molecules such as cryptophane-A may shorten the relaxation time to tens of seconds, but this remains much longer than typical ^{1}H relaxation times.

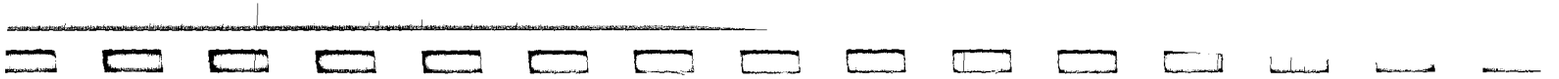

ERNEST ORLANDO LAWRENCE BERKELEY NATIONAL LABORATORY
ONE CYCLOTRON ROAD | BERKELEY, CALIFORNIA 94720

Prepared for the U.S. Department of Energy under Contract No. DE-AC03-76SF00098